

Nonlinear Mechanical Behavior of Linear Homopolymer Model Melts

Unifying Nonlinear Shear

Zur Erlangung des akademischen Grades eines
Doktors der Naturwissenschaften
(Dr. rer. nat.)

von der Fakultät für Chemie und Biowissenschaften
des Karlsruher Instituts für Technologie (KIT)

genehmigte

DISSERTATION

von

Dipl. Chem. Miriam Angela Cziep

Dekan:	Prof. Dr. Reinhard Fischer
Referent:	Prof. Dr. Manfred Wilhelm
Korreferent:	Prof. Dr. Patrick Théato
Datum der mündlichen Prüfung:	18.04.2018

Diese Arbeit wurde in der Zeit vom 15. März 2013 bis zum 9. Dezember 2017 am Institut für Technische Chemie und Polymerchemie des Karlsruher Instituts für Technologie unter Anleitung von Prof. Dr. Manfred Wilhelm durchgeführt.

Hiermit versichere ich, dass ich die von mir vorgelegte Arbeit selbstständig verfasst habe, dass ich die verwendeten Quellen und Hilfsmittel vollständig angegeben und die Stellen der Arbeit, die anderen Werken im Wortlaut oder dem Sinn nach entnommen sind, entsprechend kenntlich gemacht habe.

Karlsruhe, den 05.03.2018

Miriam Angela Cziep

Zusammenfassung

Bei der großtechnischen Verarbeitung von Kunststoffen wirken große Scherkräfte auf das Material, sodass dessen mechanisches Verhalten sich grundlegend gegenüber dem Verhalten bei niedrigen Scherraten unterscheidet. Man spricht von einem sogenannten nichtlinearen mechanischen Verhalten. Dabei ist diese Nichtlinearität stark von der molekularen Struktur der enthaltenen Polymere abhängig. Mithilfe von Rheologie ist es möglich, das mechanische Verhalten von komplexen Materialien zu untersuchen, und Zusammenhänge zwischen Struktur und mechanischem Verhalten aufzuklären. Wichtige Parameter, die die Moleküldynamik beeinflussen sind das Molekulargewicht, die Molekulargewichtsverteilung, die Topologie und die Art des Polymers selbst.

In dieser Arbeit wurde das nichtlineare mechanische Verhalten von Modellpolymersystemen mithilfe der Fourier-Transformation-Rheologie (FT-Rheologie) untersucht. Zunächst wurde mithilfe der lebenden anionischen Polymerisation verschiedene lineare Homopolymerschmelzen synthetisiert. Diese Polymere hatten eine enge Molekulargewichtsverteilung und umfassten Molekulargewichte im Bereich von nicht- oder kaum verschlauften Molekülketten, bis hin zu sehr gut verschlauften Ketten. Bei der rheologischen Untersuchung im nichtlinearen Scherbereich dieser wohldefinierten Schmelzen, erlaubte es der Ausschluss weiterer Strukturparameter, wie die Molekulargewichtsverteilung, Korrelationen

zwischen dem Molekulargewicht und dem nichtlinearen mechanischen Verhalten zu erkennen. Wie sich herausstellte, ist dieses Verhalten allein vom Molekulargewicht abhängig, nicht jedoch von der Art des Polymers.

Eine Quantifizierung des nichtlinearen mechanischen Verhaltens konnte mithilfe der intrinsischen Nichtlinearität ${}^3Q_0(\omega)$ erreicht werden. Vorhersagen aus dem Pom-Pom und dem "molecular stress function" (MSF) Konstitutivmodell, lieferten die Basis für eine semi-empirische Beschreibung der erhaltenen experimentellen Ergebnisse. Somit konnte eine Gleichung für ${}^3Q_0(\omega)$ erhalten werden, die nur das Molekulargewicht und die Scherfrequenz in Form der Deborah Nummer als Variablen beinhaltet. Diese Gleichung stellt das wesentliche Ergebnis dieser Arbeit dar.

Die Komplexität der Polymersysteme wurde anschließend durch Variation der Molekulargewichtsverteilung erhöht. Dabei stellte sich heraus, dass der zuvor gefundene Ansatz und die semi-empirische Gleichung für ${}^3Q_0(\omega)$ ihre Gültigkeit behält, jedoch das erweiterte Spektrum der Moleküldynamiken beachtet werden muss. Die scherratenabhängige Untersuchung von polydispersen Schmelzen im nichtlinearen mechanischen Bereich steht dabei erst am Anfang. Eine Erweiterung des aktuell eingeschränkten Messbereichs kann durch technische Weiterentwicklung im instrumentellen Bereich erreicht werden.

Neben der Polymerisation von linearen Polymerschmelzen, wurde die Synthese von engverteilten, verzweigten Polyisoprensystemen innerhalb dieser Arbeit realisiert. Als geeignet erwies sich dabei die sogenannte "grafting-onto" Methode, wobei ein Polyisoprenrückrat mittels Epoxidierung funktionalisiert wurde, und lebende Polyisopren-Makroanionen als Seitenketten aufgepfropft werden konnten. Messungen der intrinsischen Nichtlinearität ${}^3Q_0(\omega)$ eines Polyisopren-Kamms zeigten eine Retardierung der Rückratmobilität durch die Seitenketten, ähnlich dem Verhalten im linearen mechanischen Bereich bei kleinen Scherraten. Ein Zusammenhang zwischen dem Rückrat- bzw. Seitenkettenanteil, und der in-

trinsischen Nichtlinearität ${}^3Q_0(\omega)$ ist dabei gegeben.

Für eine weitere Aufklärung der Molekulardynamik von verzweigten Systemen, sollen Messungen der Doppelquanten-Kernspinresonanz (DQ-NMR) mit rheologischen Ergebnissen verglichen werden. Zur Realisierung dieses Vorhabens wurden erste Synthesen für deuteriertes Isopren unternommen, das als Monomer für teildeuterierte Polyisopren-Kämme dient.

Die Dissertation zeigt den Zusammenhang zwischen nichtlinearem mechanischen Verhalten von Polymerschmelzen und deren molekularer Struktur mithilfe einer quantitativen Beschreibung durch die intrinsische Nichtlinearität ${}^3Q_0(\omega)$. Basierend auf den erhaltenen Ergebnissen, eröffnen sich neue Möglichkeiten für Entwicklungen im Bereich der Konstitutivmodelle und der Molekulardynamik-Simulation.

Contents

1. Introduction	1
2. Synthesis of Model Polymer Systems	7
2.1. Principles of Living Anionic Polymerization	7
2.1.1. Monomers	8
2.1.2. Initiation	10
2.1.3. Propagation	12
2.1.4. Termination and Side Reactions	16
2.2. Synthesis of Model Comb Polymers	17
2.2.1. Grafting Through	18
2.2.2. Grafting From	19
2.2.3. Grafting Onto	20
2.3. Synthesis of Isotopically Labeled Polymer Combs	22
2.4. Polyisoprene Model Combs	23
2.4.1. Functionalization of Polyisoprene	24
2.4.2. Comb Formation	26
2.5. Synthesis of Isoprene-d8	29
2.6. Conclusion	32

3. Rheology	33
3.1. Introduction to Shear Rheology	33
3.1.1. Phenomenological Models	34
3.2. Small Amplitude Oscillatory Shear (SAOS)	41
3.2.1. Time-Temperature-Superposition Principle (TTS)	41
3.2.2. Critical Molecular Weight and Zero-Shear Viscosity	42
3.2.3. Plateau Modulus	44
3.2.4. Entanglement Molecular Weight	46
3.3. Dynamics of Entangled Polymers	46
3.3.1. Tube Model	47
3.3.2. Equilibration Time	49
3.3.3. Reptation	49
3.3.4. Primitive Path Fluctuations	51
3.3.5. Constraint Release	53
3.4. FT Rheology in the Nonlinear Mechanical Regime	54
3.4.1. Fourier Transformation - Introduction	55
3.4.2. Fourier Transformation of a Time-Dependent Stress Signal	58
3.4.3. Intrinsic Nonlinearity	61
3.4.4. Experimental Aspects of FT Rheology	61
4. Intrinsic Nonlinearity in Pom-Pom and MSF Constitutive Equations	65
4.1. Pom-Pom Model	66
4.1.1. Fundamentals	66
4.1.2. Pom-Pom Model Predictions for Nonlinearity in MAOS	68
4.2. Molecular Stress Function (MSF) Model	73
4.2.1. Fundamentals	73
4.2.2. MSF Model Predictions for Nonlinearity in MAOS	76
4.3. General Prediction for Nonlinear Behavior from Constitutive Models	80

5. Rheological Experiments	83
5.1. Methodology	83
5.2. Linear homopolymer Melts	84
5.2.1. Small Amplitude Oscillatory Shear (SAOS) Experiments	84
5.3. Medium Amplitude Oscillatory Shear (MAOS) Experiments	89
5.4. Rheological Characterization of Polymer Combs	103
5.4.1. Linear Mechanical Behavior (SAOS)	103
5.4.2. Nonlinear Mechanical Behavior (MAOS)	106
5.5. Conclusion	111
6. Conclusion and Outlook	113
Appendix	119
A. Materials and Synthesis	121
B. Model Calculations	125

1. Introduction

Motivation

In the 21st century, plastics have become one of the most dominant materials used in everyday life. The global plastic resin and plastic fiber production doubled over the last 20 years and reached the 380 million tons threshold in 2015 [1]. Europe's yearly demand alone exceeded 49 million tons of polymeric materials in 2015 [2]. Main market sectors include agriculture, electronics, automotive, building and construction and packaging, next to consumer and household goods. With more than 100 million tons, packaging is by far the largest sector [1]. Packaging is used to protect products for storage, transport, sale and use. Especially transport and warehousing of food has become a critical factor for the growing population of mankind (around 1% per year). The most used polymers in packaging are low density polyethylene (LDPE, 64 Mt/year), high density polyethylene (HDPE, 52 Mt/year), polypropylene (PP, 68 Mt/year) and polyethylene terephthalate (PET, 33 Mt/year) [1]. Processing of these polymers include injection molding, blow molding, extrusion, pressing, calendering, spinning, and foaming [3, 4]. The molecular properties of the polymer are important toward processing. Besides, temperature of the material and temperature of the related tools, as well as the pressure (up to 3000 bar), utilized for applying a deformation force, are substantial. The processing temperature influences the viscosity,

1. Introduction

crystallinity and overall mobility of the polymer, while the processing pressure induces a flow in shear and elongation. The science, describing how a material mechanically reacts to a deformation that induces a flow or a stress to the material, is called rheology. Rheological methods are used to investigate materials like polymers, liquids, emulsions, dispersions, and even solids. They are complex fluids as quantified by rheological properties. Rheology thereby classifies materials in a range of viscous and solid amounts (see chapter 3). Liquids like water can be described by Newton's law, since they are only viscous, and the viscosity is independent of the shear rate. On the other hand, a solid like iron or steel are elastic bodies and can be described by Hooke's law. Polymers are neither pure viscous nor pure elastic. They are a superposition of both properties in polymer melts and are therefore called viscoelastic. Depending on temperature and shear rate, polymeric materials can be manipulated to be more in the viscous or elastic range of the spectrum. This is crucial for polymer processing, and interesting for the final products. For example, a plastic chair should not give in under load in daily use, colloquially spoken it is solid (elastic). However, the material needs to be more 'liquid' (viscous) in production, to be able to be formed via injection molding.

The before mentioned primary forming techniques of injection molding, blow molding, extrusion, pressing, calendering, spinning, and foaming involve high shear rates (up to 1000 s^{-1}) in a greater or smaller extent. The mechanical behavior of the processed polymers under these conditions cannot be described with models of linear mathematical equations, containing only a material constant like the G modulus (Hooke) or the viscosity η (Newton) (see section 3.1.1). Instead, the mechanical stress is described more precise by nonlinear equations, which involve shear rate dependent parameters (see section 3.4.2). Correlations between nonlinear mechanical behavior and molecular structure are still being investiga-

ted with rheological experiments (rheometry), and molecular models (constitutive and numeric) are being developed that can describe and help to understand this behavior.

Nonlinear Mechanical Behavior in Literature

An established method to reach nonlinear behavior in rheometry is large amplitude oscillatory shear (LAOS). Variable, oscillating shear rates are achieved straightforward by varying oscillation frequency $\omega/2\pi$, the deformation (strain) amplitude γ_0 and measurement temperature T . Several methods have been utilized to analyze LAOS results [5]. The relaxation modulus $G(t)$ is obtained from the measured time-dependent shear stress signal $\sigma(t)$ [6]. As a function of strain amplitude, the relaxation modulus shows shear thinning or shear thickening of the material by a sudden decrease or increase of $G(\gamma_0)$ at higher deformations [7]. Converting the periodic stress signal $\sigma(t; \omega, \gamma_0)$ into so called Lissajous-Bowditch figures, $\sigma(\gamma; \dot{\gamma})$ [8], allows an identification of nonlinear behavior by deviations from the pure sinusoidal signal. The stress decomposition approach was used as a geometrical interpretation of LAOS data [9]. Following this decomposition approach, Ewoldt et al. [10, 11] expressed the nonlinear stress response by Chebyshev polynomials, where the coefficients were used to describe nonlinear behavior via Lissajous-Bowditch plots and Pipkin diagrams [12]. Rogers et al. [13, 14] used a different approach of analyzing Lissajous-Bowditch plots with a sequence of physical processes (SPP) method.

The torque signal from rheometers can also be interpreted differently. Instead of using the stress-time data $\sigma(t)$ or calculating the moduli G' and G'' , it is also possible to directly use the frequency spectrum after Fourier Transformation (FT). This approach is called FT rheology (see section 3.4). It was shown that the higher

1. Introduction

harmonic contribution, with regard to frequency and amplitude of the respective phase of the excitation frequency, can be identified with the nonlinear mechanical behavior [15]. Higher harmonic intensities have already been used to analyze complex fluids [11, 16–19] under large and medium amplitude oscillatory shear (LAOS and MAOS). The third harmonic intensity I_3 , as the dominant contribution, was chosen as a measure for nonlinearity in several publications, for example by Neidhöfer et al. [20], Fleury et al. [18], Schlatter et al. [21], Vittorias et al. [22] and Hyun et al. [23], who investigated the relative ratio $I_{3/1}(\gamma_0, \omega) := I_3/I_1$ within a magnitude spectra of the stress versus frequency $\omega/2\pi$ with regard to branched structures and long chain branching (LCB). The intrinsic nonlinearity ${}^3Q_0(\omega)$, as defined by Hyun et al. [5, 23] (see section 3.5), is only a function of the excitation frequency ($\omega_1/2\pi$). It allows to quantify the influence of relaxation processes, as for instance reptation, stretching, contour length fluctuation (CLF) and constraint release (CR) mechanisms [24]. Molecular relaxations in polymer melts are related to stretch and orientation [25, 26], and are strongly affected by molecular weight distribution (PDI) and topology of the polymer. Linear homopolymers are reasonable simple molecular models to investigate the dynamics in the nonlinear mechanical regime. The intrinsic nonlinearity ${}^3Q_0(\omega)$ was chosen in this work to quantify the mechanical nonlinear behavior under oscillatory shear as a function of molecular weight and PDI of a large variety of linear homopolymer melts.

With the time-temperature superposition (TTS) principle [27], it was possible to generate ‘nonlinear master curves’ for ${}^3Q_0(\omega)$, using the shift parameters from respective linear master curves. In previous publications, it was shown that these nonlinear master curves are sensitive to molecular topology, e.g. long chain branching (LCB) of polystyrene combs [23, 28]. Interpretation of the results however stayed on a qualitative level.

Several research groups conducted simulations of $I_{3/1}(\gamma_0)$, ${}^3Q(\omega, \gamma_0)$ and especially ${}^3Q_0(\omega)$, using different constitutive models [24–26, 29]. The Pom-Pom model was used to predict the nonlinear behavior of branched polymer systems [24, 30, 31] and comparisons between experiments and model prediction already were used to re-evaluate the existing model [29]. Wagner et al. [26, 32] developed a molecular stress function (MSF) model. They could show, that a linear dependence of ${}^3Q_0(\omega)$ toward the difference between the orientational effect (parameter α) calculated from the Doi-Edwards model and the stretching effect (parameter β), obtained from the MSF model, exists ($Q \propto \alpha - \beta$). Using the MSF model, Abbasi et al. [25] were able to predict the LAOS behavior, as well as start-up shear and extensional deformations of different LDPE samples, with a single set of nonlinear parameters. Constitutive models, like the Pom-Pom and MSF model, are based on fundamental physical characteristics of macromolecules. They were chosen in this thesis as templates for a quantitative, analytical description of the obtained results, and can help to understand fundamental dynamics of polymers.

Objective and Outline of this Thesis

The quantification of mechanical nonlinear behavior and its correlation to the molecular structure of molten polymers are the main objective of this thesis. Mechanical nonlinearity of simple model systems, i.e. linear homopolymer melts as a function of monomer, molecular weight and polydispersity, have not been studied systematically before. Rheology, and especially FT rheology, is a sensitive method to give insights into the microscopical, molecular level of a viscoelastic material, yet it is itself a macroscopic technique, experimenting on the bulk material. Physical interpretation of observed effects is still not clear in the nonlinear regime. Correlations between underlying relaxation processes and experimental

1. Introduction

results of the intrinsic nonlinearity $Q(\omega)$ can be made with the help of constitutive modeling, and can also help to expand and refine existing model theories. In a next step, obtained results can be very useful and can be carried over to molecular dynamic simulation.

The thesis starts with a presentation of fundamentals in anionic polymerization (chapter 2), which was the main synthesis method for the preparation of linear homopolymer melts. Chapter 2 also includes a detailed synthesis route for preparation of polyisoprene combs, as an outlook to branched model systems.

An introduction to shear rheology is given in chapter 3. Basics of linear and nonlinear rheology (FT rheology) are presented, as well as basics of the polymer tube model, which describes polymer dynamics in a phenomenological way. The constitutive models (Pom-Pom and MSF) are lined out in chapter 4. These models served as a basis for the following interpretation of rheological experiments on polymer melts, that are presented in the following chapter. In chapter 5 a detailed experimental approach to obtain and quantify mechanical nonlinear behavior of linear molten polymers is given (section 5.2). First results on the rheology of branched polyisoprene are shown in section 5.4.

2. Synthesis of Model Polymer Systems

2.1. Principles of Living Anionic Polymerization

The principle of a "living" polymerization was established in 1956 by Szwarc et al. based on the work of anionic polymerization of styrene, initiated by a sodium-naphthalene complex [33]. Szwarc later defined a living polymerization as "[...] a chain growth reaction, which takes place in the absence of termination or chain transfer reactions" [34]. Within this sentence, the advantages and disadvantages of an anionic polymerization are already mentioned. The disadvantage is at the same time the advantage, namely that this method is only valid in "absence of termination or chain transfer reactions", meaning no impurities are allowed within the reaction vessel. This demands meticulous working and thorough preparation of reagents. The absence of termination and chain transfer reactions also means, that desired molecular weights can be calculated easily, even very high molecular weights are possible, and that at the same time low polydispersities can be reached. Anionic polymerization is also a versatile method to produce polymers with rather complicated but defined molecular structures, e.g. blockcopolymers, combs and stars, with specific features as for example a given number

2. Synthesis of Model Polymer Systems

of sidearms. There are also lots of monomers available that can be polymerized with anionic synthesis (for monomer requirements see section 2.1.1), and common initiators, e.g. metal organyls, are commercially available. However, the economical impact of anionic polymerization remained low (ca. 500 000 t/year production) compared to free radical polymerization and other controlled polymerizations with catalysts (especially Ziegler-Natta), since the two most used monomers, ethene and propylene, cannot be polymerized via anionic polymerization. Nevertheless, the method is used by industry to produce polymers with special material properties that are based on characteristic molecular structures, such as the aforementioned topologies. An examples where anionic polymerization is used are rubbers for tires (*cis*-1,4-polybutadiene and -isoprene), additives (star topologies) or adhesives (e.g. poly cyanoacrylate) [35].

2.1.1. Monomers

The capability of a vinyl monomer to undergo living anionic polymerization is dominated by its carbanion formation and stabilization, after activation of the monomer double bond through a potent initiator (see section 2.1.2). Substituents that can stabilize the propagating negative charge, inductively or through resonance, are indispensable to enable the nucleophilic addition onto a next monomer (fig. 2.1) [36]. The carbanionic species of a monomer can be seen as the conjugate base of a protonic acid whose pK_a can be evaluated [37]. Carbanion stability information deduced from pK_a values for corresponding hydrocarbon conjugated acids can be used to make predictions regarding the relative reactivity of monomers [38]. This can help to choose appropriate initiators and to gauge relative polymerization speeds for various monomers. It is also important to predict and understand the required order of addition of monomers for block copolymer for-

mation and to understand the copolymerization behavior of various monomers [38].

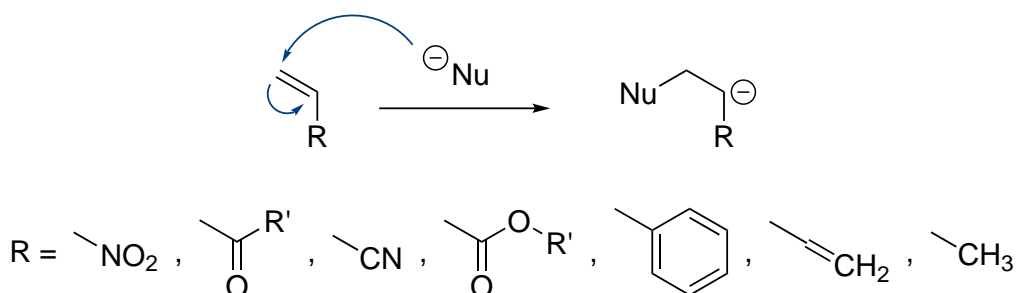


Figure 2.1.: Vinyl monomer activation by a nucleophile (Nu) in living anionic polymerization, and selected substituents (R) with relative carbanion stabilization in descending order.

Corresponding conjugated bases of monomers with relatively high pK_a , e.g. styrene anions, are very reactive towards electrophilic species. Electron-donating groups or acidic proton-donating groups, such as amino-, carboxyl-, hydroxyl-, halogen- or acetylene functional groups will lead to side reactions or termination of the active species [36]. It is therefore essential to excluded these kind of chemical functionalities within the reaction environment of anionic polymerization by choosing a compatible monomer and solvent (for influence of the solvent on the structure also see 2.1.3).

Aromatic rings, double bonds, carbonyl, ester and cyano groups stabilize the negative charge of a carbanion [36]. Vinyl and related monomers require an activation of the monomer double bond, for example by electron withdrawing substituents, or by those inducing a strongly positive polarization of the β -carbon atom of the double bond [37]. Heterocyclic monomers can undergo living anionic polymerization through ring opening either by nucleophilic substitution or by nucleophilic addition onto a carbonyl group, followed by an elimination [37].

2.1.2. Initiation

The original initiation of an anionic polymerization reaction with sodium naphthalene, as utilized by Szwarc et al. [33], is started by an electron transfer from the alkali metal to the naphthalene. An aromatic anion-radical is formed, which then initiates the polymerization (fig. 2.2).

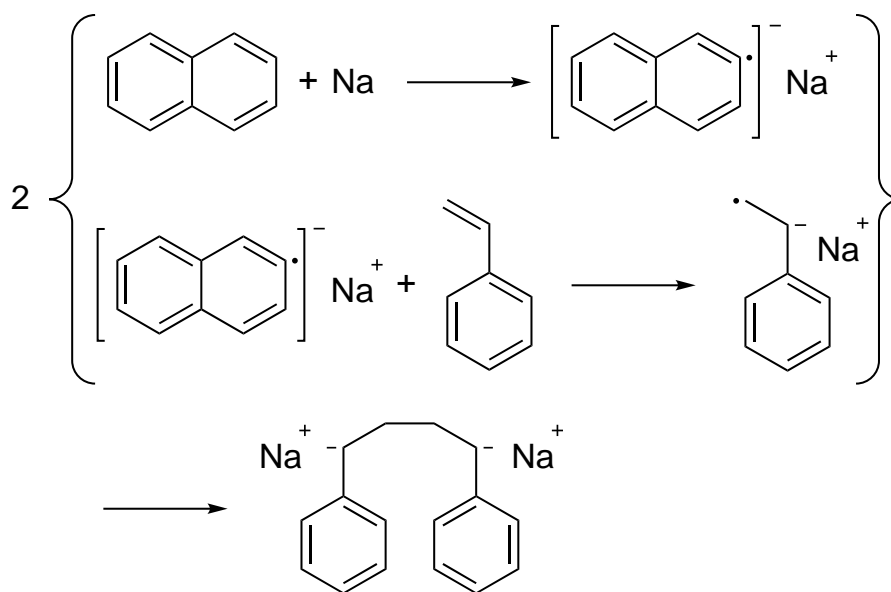


Figure 2.2.: A bifunctional initiator for living anionic polymerization is formed via electron transfer from sodium to naphthalene.

It is important to choose an initiator reagent that ensures a fast initiation step compared to the propagation and the absence of side reactions [37]. Only then the characteristic low polydispersities of living anionic polymerizations can be achieved. This is a reason why one of the most popular initiation methods is the application of strong nucleophilic Lewis bases. Usually monofunctional organometallic species such as the isomers of butyl lithium (*n*-, *sec*-, *tert*-) are used. Lithium organyls are capable to initiate economically important monomers with relatively weak electron-withdrawing groups, such as styrene, 1,3-butadiene and isoprene. The initiation step starts with the addition of the lithium alkyl to the monomer, followed by propagation (fig. 2.3).

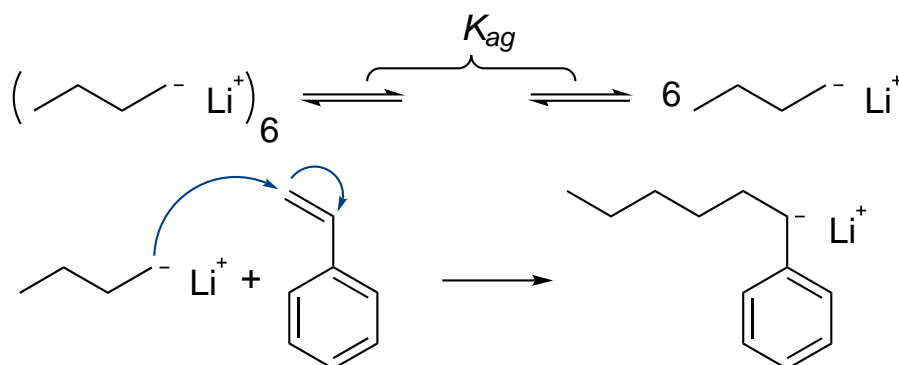


Figure 2.3.: Initiation of styrene with *n*-butyllithium. Lithium organyls build aggregates (here hexameres) with reduced reactivity in a multi step pre-equilibrium (rate constant K_{ag}).

It is important to note, that lithium alkyls build aggregates that are substantially less reactive than the "monomeric" version. In hydrocarbon solutions, the aggregate and the monomeric molecules are in equilibrium with favor towards the aggregates. Therefore, reactions in polar solvents (tetrahydrofurane, THF) or addition of certain reagents (tetramethylethylenediamine, TMEDA) that can break up the aggregates are used. Formation of solvated ion pairs and free ions increase initiation speed substantially. However, this also facilitates side reactions, for example with the solvent.

Independent of the initiator applied, the general reaction scheme for initializing an anionic polymerization occurs with a nucleophilic attack of the base I^- (with the metal counter ion Me^+) at the vinyl double bond of the monomer $CH_2=CHX$ (eq. 2.1, X represents the substituent). In this reaction, a first monomer carbanion is formed, which acts as active center in the followed propagation.



2.1.3. Propagation

The chain growth proceeds by addition of further monomers (M) to the living anion, which is built by the initiation, or to already existing polyanions (P_n^-). This results in a repeating reproduction of anionic species at the end of the molecular chain (eq. 2.2).

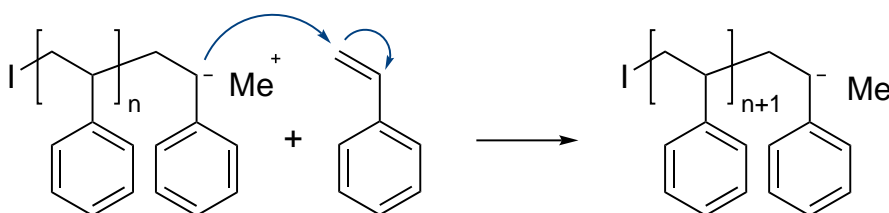


Figure 2.4.: Propagation on the example of polystyrene. The active center at the chain end adds to further free monomers, resulting in a continuous chain growth.

The number of reactive ends is defined by the initiator, where for example initiation with sodium-naphthalene leads to two opposing growing ends (fig. 2.2) and lithium alkyls like n-butyllithium initiate only one active end (fig. 2.3).

Structure of the Propagating Species

The microstructure of the resulting macromolecular chains in living anionic polymerization strongly depends on the electron density on the carbanionic active center. Therefore three parameters control the structure for vinyl monomers: the substituents at the double bond, the counterion and the solvent [37].

The substituent has a major influence on the reactivity of the monomer, as well as the structure and physical behavior of the polymer (also see chapter 3). In general, electron-withdrawing groups decrease reactivity, electron-donating groups increase intrinsic reactivity of the carbanionic active centers [37]. Reactivity is

2.1. Principles of Living Anionic Polymerization

also decreased, if the substituent promotes delocalization of the negative charge. As mentioned before, this is important for the choice of initiator and the overall synthesis strategy (monomer sequence order for block copolymers, reaction temperature and time, etc.).

The counterion has less of an effect on the microstructure than the substituent or the solvent. Usually, alkali or earth alkali metal ions are used as counterions, especially lithium, because of the popular use of butyllithium as initiator. The main influence of the counter ion is due to its size. Small ionic radii favor a partial covalent character of the bond between the counterion and the anionic active center [37]. Bigger cations lead to a separation of charges, and therefore to a different coordinative environment of the growing chain end. Figure 2.5 shows the range of possible ion pairs. Contact ion pairs (b) and solvent-separated ion pairs (c) most likely occur in living anionic polymerization, because of the cation size and solvent choice (see below).

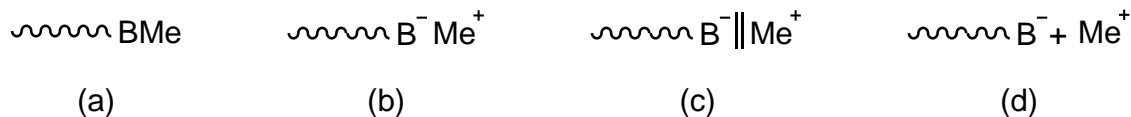


Figure 2.5.: Range of ion pair behaviors from covalent (a), tight/contact ion pair (b), solvent-separated/loose ion pair (c) to highly solvated/free ion pair (d).

The solvent choice is of utmost importance in living anionic polymerization. As already mentioned, because of the very high reactivity of the anionic species, protic solvents cannot be used. The solvent fulfills up to three roles in anionic polymerization [37]. First it serves as a diluent, so that the reaction heat can be removed and controlled. Sometimes aggregates of the reactive centers vary also with the range of concentration (e.g. polystyryllithium dimers). The second role of the solvent is that of a solvating agent for the reactants. This is especially interesting in combination with the nature of the counterion and therefore the

2. Synthesis of Model Polymer Systems

formation of ion pairs or free ions (see fig. 2.5). The role of the solvating agent can also be fulfilled by additives that coordinate the cation and stretch the ion pair distance (e.g. TMEDA, crown-ether, fig. 2.6).

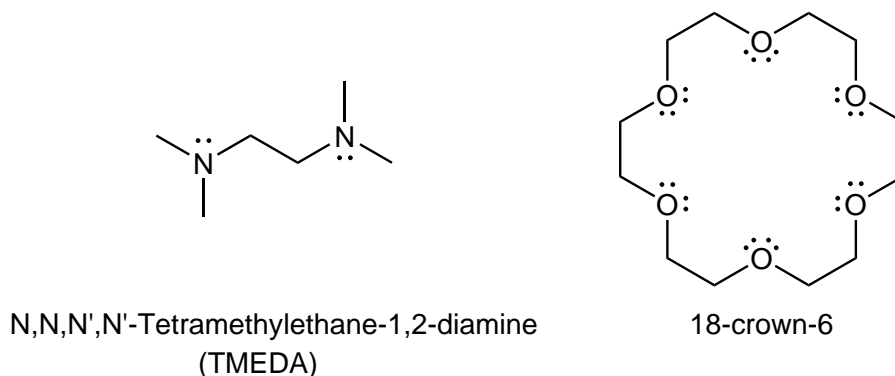


Figure 2.6.: Examples of solvating agents for counter ions, used in anionic synthesis to enhance reactivity of the living species.

Third, the solvent can serve as dissociating agent, when its permittivity is sufficiently high (e.g. THF 7.8 at 20 °C) [37]. In this case, it is even possible to separate the anion and counterion and form free ions. The reactivity of free ions is extremely high and even in small concentration have a remarkable impact on the reaction kinetics [37].

Anionic Polymerization of 1,3-Dienes

The influence of the mentioned three parameters, substituent, counterion and solvent, on the stereochemistry of polymers is especially important for the anionic polymerization of 1,3-dienes. Four possible stereochemistries of the monomer are possible with 1,3-dienes (example for polyisoprene in fig. 2.7).

Table 2.1 lists possible microstructure ratios for polybutadiene and polyisoprene with varying counterions and solvents.

2.1. Principles of Living Anionic Polymerization

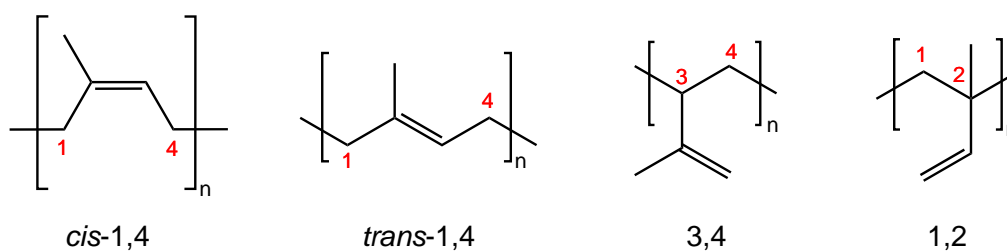


Figure 2.7.: Polyisoprene can take on four different microstructures, depending on solvent and counterion during synthesis. Every microstructure inherits different glass transition temperatures, e.g *cis*-1,4 has a T_g of -70°C , and *trans*-1,4 has a T_g of -58°C [39].

counterion	solvent	structure of polymer (%)			
		<i>cis</i> -1,4	<i>trans</i> -1,4	3,4	1,2
<i>Isoprene</i> (at 25°C)					
Li	n-hexane	93	0	7	0
Na	n-hexane	0	47	45	8
Li	THF	0	30	54	16
Na	THF	0	38	49	13
<i>1,3-Butadiene</i> (at 0°C)					
Li	n-pentane	35	52		13
Na	n-pentane	10	25		65
Li	THF	0	4		96
Na	THF	0	9		91

Table 2.1.: Solvent and counterion effect on stereochemistry of polyisoprene and polybutadiene [40]. By choosing a certain combination of solvent and counterion, the microstructure amount can be manipulated.

The *cis*-1,4 microstructure demands a highly coordinated system of the reactive anion, the counterion and a monomer [41, 42]. As a consequence, *cis*-1,4 content is higher in unpolar solvents with small counterions, where the ion pair is tight. With increasing size of the counter ion, this coordinative system is loosened up and the *cis*-1,4 ratio is generally decreasing to even diminishing low contents. In THF, a slightly polar solvent, the propagating center is free and 3,4-polymerization for isoprene is highly favored over any 1,4 stereochemistry [40]. Butadiene in polar solvents favors 1,2 polymerization instead, which shows the influence of the substituent. Table 2.1 shows empirical data for the stereochemi-

2. Synthesis of Model Polymer Systems

stry of 1,3-dienes, which can typically be obtained by adjusting counterion and solvent. However, there is no mechanism that adequately explains all features of the anionic polymerization of 1,3-dienes [40].

The stereochemistry of the penultimate monomer is given by its structure during addition of the last monomer. For poly-1,3-diene anions, the allylic end is in equilibrium between the *cis*- and the *trans*- form (provided 1,4 addition). The stereo equilibrium is shifted to *cis*-1,4 in polar solvents, and to *trans*-1,4 in unpolar solvents [43]. This is contrary to the dominant microstructure for anionic polymerization of 1,3-dienes in respective solvents (see tab. 2.1). Polyanions in hydrocarbon solvents exist as aggregates in equilibrium with the monomeric form. The isomerization of the end-group mainly takes place while the polyanion is in its aggregated form, while monomer addition occurs only in the monomeric form. Therefore, it can be concluded, that monomer addition in unpolar solvents prefers *cis*, and that the transition between aggregate and monomeric form is faster than the end group isomerization. In polar solvents the situation is reversed. Mechanisms that try to explain this outcome for polyisoprene in presence of lithium as counterion have been proposed [41, 42, 44] and discussed [38, 43], however no satisfying explanation has been found, as influences are complex and manifold.

2.1.4. Termination and Side Reactions

The living character of the anionic polymerization implies that no termination reactions occur. A deliberately end of the propagation can be induced with proton donating reagents like water or alcohols that react with the carbanions, after all monomers have reacted. However, all impurities, especially water, should be removed from the reaction vessel prior to initiation. Additionally to its termination character, water is an active chain-transfer agent and even small concentrations,

present during polymerization, have a negative effect on molecular weight and limit the polymerization rate [40]. The reactivity of the carbanions towards acidic reagents is so high, that atmospheric humidity and residual absorbed water on glassware leads to unwanted termination and side reactions.

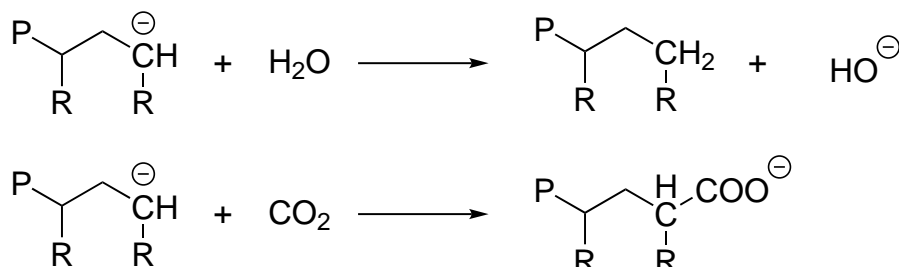


Figure 2.8.: Termination of living carbanions with water and carbon dioxide.

Anionic polymer chain ends also react with oxygen (20%) and carbon dioxide (0.04%) within air (fig. 2.8). Especially the reaction with oxygen has a noticeable impact, since it leads to a chain coupling, and can be noticed as an increase in double molecular weight, for example in a GPC measurement (fig. 2.9). It is also possible to exploit a termination reaction to functionalize or couple chain ends [38].

2.2. Synthesis of Model Comb Polymers

Comb polymers are grafted macromolecules with one backbone and at least two branches. The difference to random branched polymers like LDPE is, that defined branches are constructed on purpose by special synthesis strategies. These reaction routes allow the chemist to control certain parameters of the polymer comb, for example the number and length of the branches. It is therefore possible to synthesis model systems that can be investigated for their chemical and physical behavior.

2. Synthesis of Model Polymer Systems

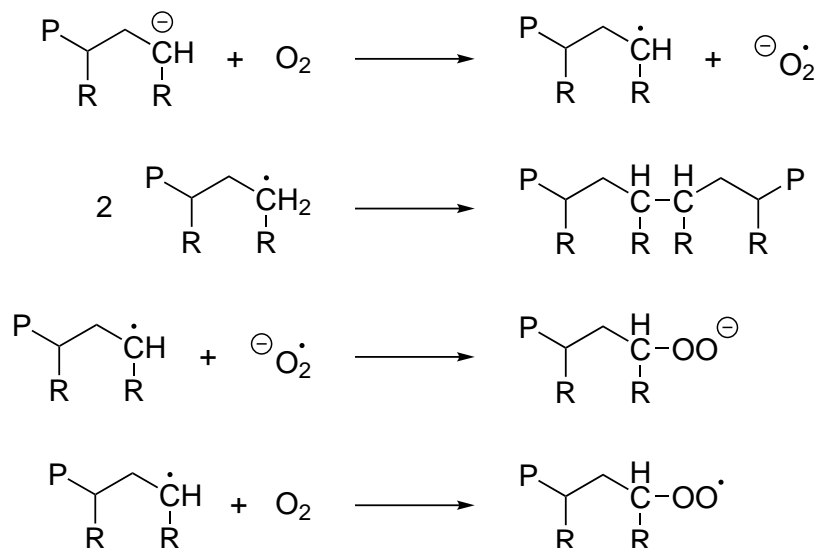


Figure 2.9.: Oxygen from air leads to several termination and side reactions with living anions.

In general, there exist three main strategies for graft polymer synthesis: grafting through (also called macromonomer method), grafting from and grafting onto [36, 45, 46].

2.2.1. Grafting Through

End functionalized polymers can be copolymerized with other monomers and lead to a comb like molecular structure (fig. 2.10). The macromonomers form side chains in the final polymer, giving this method also the name macromonomer method.

It is important to at least have an idea about the copolymerization parameters of the involved conventional monomers and the macromonomers, to exploit this method to its full potential. Usually, an even or random distribution of the branches is desired, where the ratio of comonomer concentration controls the number of branches. The difference in reactivity ratios of the involved comonomers are

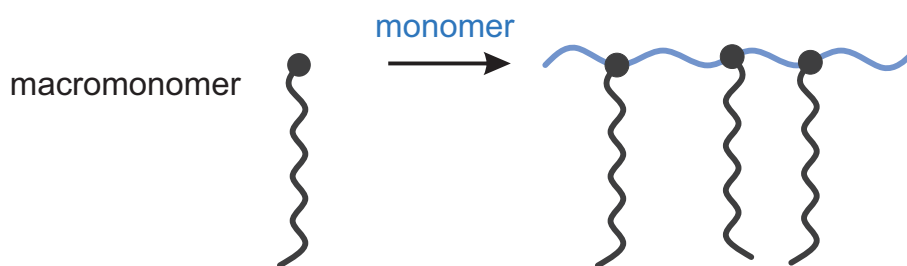


Figure 2.10.: Grafting Through approach. Copolymerization of macromonomers with monomers leads to a comb-like polymer structure.

generally greater in anionic polymerization than in free radical polymerization [46]. This may lead to a more brush-like AB block copolymer structure, where one comonomer reacts completely through before the next one starts. A popular strategy to enhance control over branch location within a polymer comb via the grafting through method is the utilization of diphenylethylene (DPE) endcapped macromonomers [47]. DPE endfunctionalized macromonomers do not homopolymerize and can be added sequentially with the other monomer [46].

An advantage of the macromonomer method is that no fractionation is needed after completed synthesis to isolate the comb polymer. With appropriate conditions, it is also possible to obtain a wide variety of well-defined structures [45].

Characterization of polymer systems synthesized with grafting through is challenging, since only the molecular weight and polydispersity of the macromonomer and of the complete comb can be determined directly. The exact composition of the backbone is not easily ascertainable.

2.2.2. Grafting From

The grafting from method utilizes active sites that are introduced along the polymer chain of a backbone. These active centers are able to initiate the polymerization of another monomer, leading to branch formation (fig. 2.11).

2. Synthesis of Model Polymer Systems

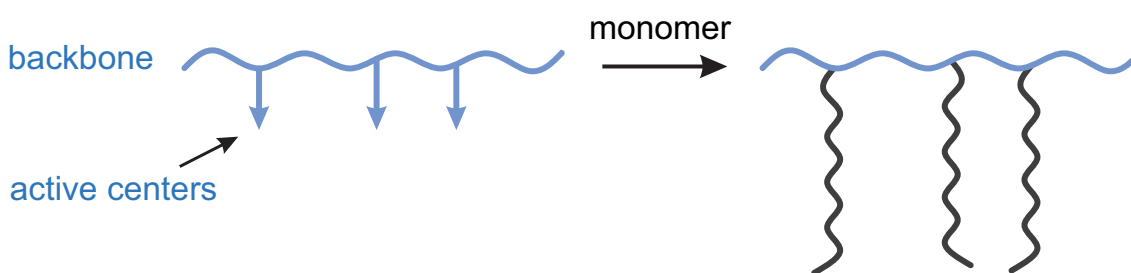


Figure 2.11.: Scheme of the grafting from approach. Branches grow from active centers at the backbone by addition of monomer.

Classically, grafting-from employs some form of acid/base chemistry [48]. Acidic hydrogens within the backbone, for example phenols, amides or alcohols, can be removed by a base (e.g. *tert*-BuOK or lithium diisopropylamide) [49, 50]. The created active sites then initiate anionic polymerization of added monomers. Another possibility utilizes metallation of allylic, aromatic or benzylic protons on the backbone with organolithium compounds (e.g. *sec*-BuLi) [51, 52].

The grafting-from method has several disadvantages, such as that the sidechains cannot be characterized independently from the backbone. This impedes identification of exact branch length and density. Initiation of sidechain polymerization is often slow, so that molecular weight distribution of the branches are higher compared to other grafting techniques, which makes it also more difficult to plan molecular weights in advance.

2.2.3. Grafting Onto

The grafting onto method utilizes a reaction between nucleophilic chain ends (i.e. the branches) and electrophilic functional groups along a backbone (fig. 2.12). The functional groups can be introduced into the backbone post-polymerization. A randomly branched molecular comb is then formed by a coupling reaction (grafting).

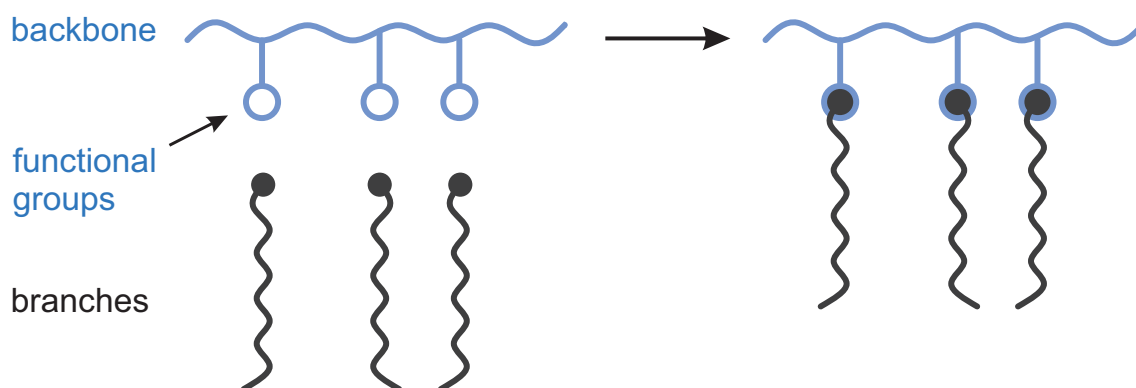


Figure 2.12.: Schematic representation of the grafting onto approach. Branches grafted onto functional groups lead to formation of a polymeric comb-like structure.

Several post-polymerization modifications, that are suitable for coupling with living anionic sidechains have been reported. The most common approach is functionalization of polystyrene (PS) with chloromethylation [53–55]. Hydrosilylation is a versatile route to grafted polymers from materials that contain double bonds, especially polybutadiene (PB) and polyisoprene (PI). Silane groups are introduced, involving platinum (e.g. H_2PtCl_6) [56, 57] or rhodium catalysts (e.g. $\text{Rh}(\text{PPh}_3)_3\text{Cl}$) [58].

The main advantage of the grafting onto method is the possibility to synthesize and characterize backbone and sidechains independently. Branched structures from this route are therefore very well defined in terms of molecular weight of the backbone and sidechains, the number of branches and PDI. It is even possible, to graft arborescent polymers by repeated functionalization of already obtained branched structures [59, 60]. The obtained comb-like structures are also nearly monodisperse, since the backbone and the sidechains can be prepared by anionic polymerization. Main challenges are side reactions (e.g. crosslinking) due to the high reactivity of the living anions or low grafting yields, because of steric barriers or non-compatibility of functional group and nucleophilic chain end.

2.3. Synthesis of Isotopically Labeled Polymer

Combs

The investigation of linear homopolymer systems offer the possibility to correlate observed viscoelastic behavior with few variable properties, such as the molecular weight, polydispersity or the effect of the monomer (see chapter 3). Therefore, the focus of this work lies on these most simple polymer systems.

In a further project cooperation with Prof. Kay Saalwächter, University of Halle-Wittenberg, the molecular dynamics of branched polymers are investigated with FT rheology (Prof. Wilhelm's group) and double quantum NMR (Prof. Saalwächter's group). Results, obtained from the investigation of the simple linear polymer melts from the here presented work, are the foundation for enlightening the hierarchical relaxation processes of polymer combs. The synthesis of first model comb polymers for this project were also conducted as part of this work.

The synthesis of model comb polymers from styrene monomers is well established and examination of their nonlinear mechanical behavior was already presented in various publications. First FT rheology experiments on polystyrene (PS) model combs were already presented by Hyun and Wilhelm [23] with introduction of the intrinsic nonlinearity ${}^3Q_0(\omega)$ (see section 3.4.3). Later, Kempf et al. [28, 61] continued the rheological research on self-synthesized branched polystyrene and polystyrene derivatives. Polystyrene combs are however not suitable for the usage with a low field NMR spectrometer as demanded by the named cooperation with Prof. Saalwächter, and explained in the following. The investigation of molecular relaxation times with NMR techniques require the sample to be very mobile, meaning the polymer must be heated to typically 100 °C to 150 °C above the glass transition temperature T_g . The T_g of polystyrene is around

100 °C, which demands a measurement temperature of at least 200 °C and above. This temperature is not only too high for some parts of the instrument, but may lead to oxidation and thermal degradation of the polystyrene sample, and also to possible depolymerization (the ceiling temperature for styrene is 310 °C [40]). Alternatively, pure *cis*-1,4-polyisoprene (PI) has a T_g of around -70 °C (also see fig. 2.7) It can be synthesized via anionic polymerization with more than 90% *cis* microstructure content (see table 2.1), which makes it a suitable substitute for polystyrene.

The synthesis strategy chosen in this work to build up branched polyisoprene structures, was a functionalization of a PI backbone and then use the grafting onto method (see section 2.2.3) to form the desired comb.

2.4. Polyisoprene Model Combs

A polymer comb molecule consists of the backbone (bb) and a certain number of sidechains (sc). The polyisoprene backbone precursor and the sidechains were prepared with anionic polymerization, utilizing *sec*-butyllithium (*s*-BuLi) as initiator and cyclohexane as solvent (fig. 2.13). The synthesis was conducted in Schlenk reactors on a high-vacuum line, that allowed exclusion of air and moisture, which lead to unwanted side reactions (also see section 2.1.4).

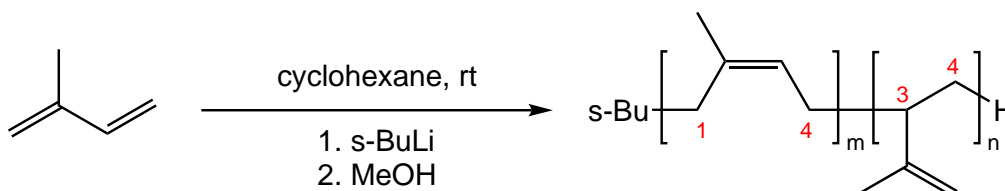


Figure 2.13.: Anionic polymerization of polyisoprene, initiated with *s*-BuLi. The dominant microstructure is *cis*-1,4 with more than 90 mol% expectedly ($m \gg n$).

2. Synthesis of Model Polymer Systems

In case of backbone synthesis, the living polymers were terminated with degassed methanol, then precipitated in methanol, dried and characterized afterwards. Living sidechains were freshly synthesized for comb formation, and kept within the reaction vessel until needed. For sidechain characterization, only a small sample was taken in an Argon counterstream with a syringe, and terminated with methanol.

The choice of solvent and counterion influences the microstructure of the resulting polyisoprene (see section 2.1.3). Typically, the use of cyclohexane and *s*-BuLi resulted in a 95 mol% 1,4- and 5 mol% 3,4- microstructure for the monomers (fig. 2.14, literature values are given in tabel 2.1 in section 2.1.3).

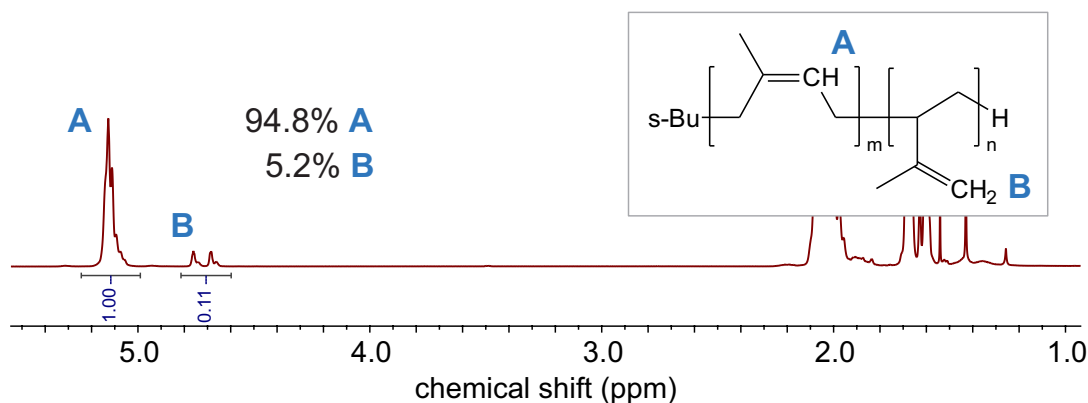


Figure 2.14.: 400 MHz ¹H-NMR of anionic synthesized polyisoprene with cyclohexane as solvent and *s*-BuLi as initiator. Peak signals at 5.13 ppm are assigned to the *cis*-1,4 microstructure (A, one proton), 3,4 protons result signals between 4.66-4.76 ppm (B, two protons) [60].

2.4.1. Functionalization of Polyisoprene

The grafting-onto method demands the introduction of functional groups into the backbone, which are reactive to the living, anionic endgroups of the sidechains. Functionalization of the C-C double bonds of the backbone was achieved by epoxidation.

The advantage of epoxidation compared to other possible reactions like hydrosilylation is, that it is a highly selective and experimentally simple method. Hydrosilylation was proven to be a potent strategy for the formation of various branched molecules [62]. However, reagents include silicon tetrachloride, which is classified as toxic, and consequently should be avoided. The preparation of the educts also require an increased workload due to additional distillation, and longer reaction times (around 8 hours).

Epoxidation of the inner double bonds of PI can be accomplished by adding a reaction mixture of formic acid and hydrogen peroxide (H_2O_2) to the polymer at room temperature (fig. 2.15). For this, the assigned backbone was dissolved in toluene. Formic acid was then given to the polymer, and H_2O_2 was added dropwise. The separation between organic phase (polymer solution) and aqueous reagents (peracid) demanded a constant stirring control. The heterogeneous reaction was stopped after one hour by washing the reaction mixture with distilled water until pH 6 was reached. The organic phase, containing the functionalized backbone, was then separated, dried with magnesiumdichloride (MgCl_2) and precipitated in methanol. The reaction yield was determined to be 20 % to 30 % via $^1\text{H-NMR}$.

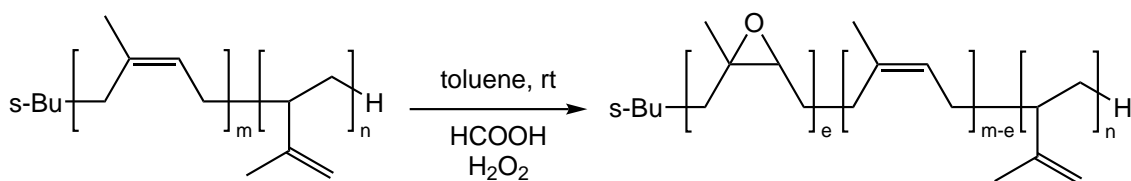


Figure 2.15.: Epoxidation of anionically synthesized polyisoprene. Only double bonds of the *cis*-1,4 microstructure ($m \gg n$) get functionalized, due to kinetic control of the reaction.

The epoxidation of dienes is an electrophilic reaction. A higher electron density and additional alkyl substituents increase reactivity. A tri-substituted alkene, like the intrachain double bond of PI, reacts 6500 times faster, and a di-substituted

2. Synthesis of Model Polymer Systems

double bond, similar to the terminal double bonds of 3,4-PI, reacts 500 times faster than ethene [63]. A selective functionalization of the 1,4-PI double bonds is consequently kinetically controlled. The high amount of intrachain double bonds in anionic PI (95 %) offers the possibility for synthesis of dense branched-like structures via the epoxidation route.

Side reactions, such as ring opening of the epoxide, take place at high reaction temperatures and high acid concentrations [64]. The chosen reaction conditions therefore minimize unwanted byproducts (alcohols). Figure 2.16 shows the ^1H -NMR spectrum of an epoxidized PI (ePI). The peak signal at 2.7 ppm is assigned to the proton, bound at the epoxi ring [65, 66].

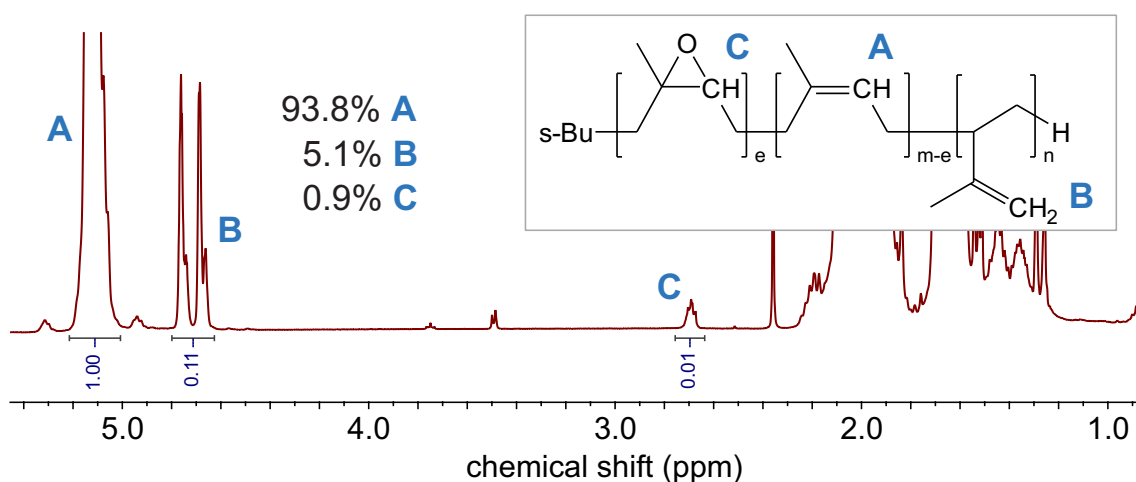


Figure 2.16.: 400 MHz ^1H -NMR of partly epoxidized polyisoprene. The single proton at the epoxide ring (C) gives a peak signal at 2.7 ppm (A, one proton for *cis*-1,4, B, two protons for 3,4). Integration of the peak areas results the microstructure content of the functionalized PI backbone, with approximately 0.9 % epoxidized double bonds ($m \gg n \gg e$, compare to fig. 2.14).

2.4.2. Comb Formation

The grafting reaction of the PI anions onto the epoxidized backbone is a nucleophilic ring opening reaction (fig. 2.17).

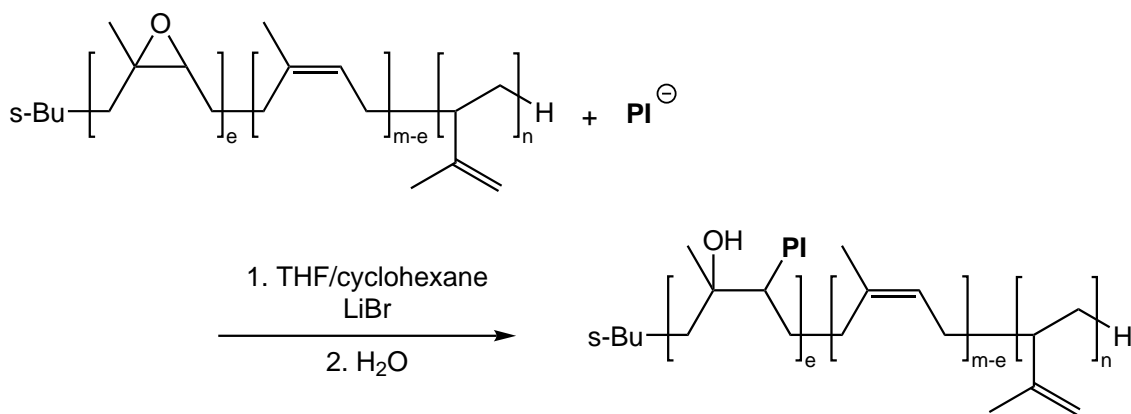


Figure 2.17.: Comb formation reaction via nucleophilic attack of living polyisoprene (sidechains) onto an epoxidized polyisoprene backbone.

The reactivity of the anionic sidechains can be enhanced by separating the counterion from the reactive chain end (see section 2.1.3). The synthesis of the sidechains was conducted in cyclohexane, an unpolar solvent, which means, that addition of solvating agents (see fig. 2.6) or a polar solvent is needed to improve reaction speed. The backbone was therefore dissolved in dry THF, so that a solvent ratio of cyclohexane:THF of 2:1 was achieved. Further improvement of reactivity was attained by adding a Lewis acid to the reaction mixture. Lithium salts are weak Lewis acids, that can increase the reactivity of the epoxide rings by coordination. Simultaneously, they decrease the reactivity of the living anions by a common ion effect. Yuan et al. [60] obtained the highest reaction yields with lithium bromide as promoter for coupling of PI anions onto epoxide rings.

The final comb formation setup in this work consisted of the the main reactor with the backbone dissolved in THF, and lithium bromide (LiBr) as promoter. Attached to the main reactor, connected via a glass joint, was an excess of living sidechains, dissolved in cyclohexane. The sidechains were added slowly to the backbone/LiBr mixture at room temperature, upon which the solvent color immediately turned into a bright yellow. The distinct color of the surplus PI anions served as indicator for the reaction stability. Without termination due

2. Synthesis of Model Polymer Systems

to unwanted side reactions (impurities or ring opening of THF), the bright color got preserved over more than two days at room temperature. The reaction was then terminated by addition of degassed methanol. The polymer mixture, consisting of PI combs and linear PI, was separated by precipitation fractionation from THF/methanol.

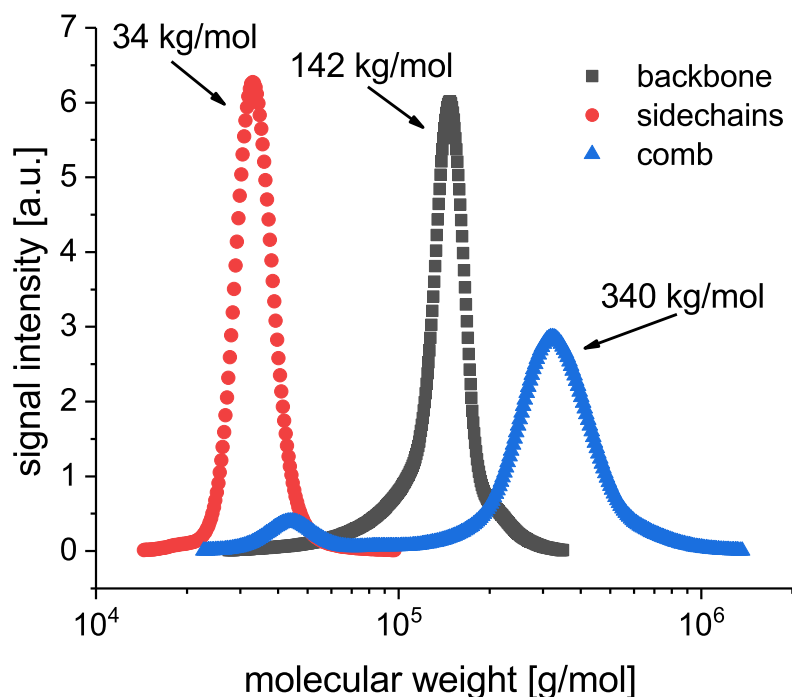


Figure 2.18.: SEC-MALLS of a synthesized polyisoprene comb and linear polyisoprenes, which were used as backbone and sidechains. The calculated number of sidearms from this measurement results 5.8 in average.

Figure 2.18 shows the SEC-MALLS (size exclusion chromatography combined with multi angle laser light scattering) result for the different components of an example PI comb formation. At 34 kg/mol the sidechains can be identified in the sample, taken directly from the sidechain reactor. They also remain in the unfractionated polymer mixture after the grafting reaction, since they have been added in excess. The functionalized backbone has a molecular weight of 142 kg/mol ($M_w/M_e = 30$). The disappearance of the backbone signal after comb formation

indicates the successful reaction between functional groups (epoxides) and living anions. At 340 kg/mol the newly formed PI comb is detected with a PDI of 1.07.

Determination of Number of Sidearms

In general, SEC calibrations are not available for comb polymers, which demands SEC-MALLS as preferred method for molecular weight and sidearm number determination. The PI comb depicted in figure 2.18 has an average number of 5.8 sidearms per molecule, as calculated from SEC-MALLS. The number of sidearms and the total molecular weight of the comb can also be calculated from the stoichiometry of the reaction, when no light scattering is available for SEC [60, 67]. The area ratio of the comb and sidearm signals from the unfractionated reaction mixture from SEC, using linear PI standards as calibration, was calculated and compared to the mass ratios of the grafting educts. In the presented example, the number of sidearms was determined as 5.8 in average, and therefore a total molecular weight of around 332 kg/mol for the final comb. The calculation of sidearms and comb molecular weight via area ratio yielded a similar result to SEC-MALLS in this example.

2.5. Synthesis of Isoprene-d8

A macromolecule has a wide spectrum of relaxation times, that can be assigned to dynamics of different segments of the molecule (also see section 3.3). The inner part will behave and relax differently than the chain ends. The investigation of these different molecule segment dynamics via ¹H-NMR can be achieved by "hiding" other respective parts with deuterons. Therefore, only the protonated chain segments will be detected. It was shown in the previous section, that the

2. Synthesis of Model Polymer Systems

synthesis of branched polyisoprene structures is possible with anionic polymerization methods. It can be assumed, that the synthesis of partly deuterated PI combs with this method is also viable. The needed monomer isoprene-d8, where all protons are exchanged with deuterons, is consequently a very valuable molecule. This is indicated by the rare commercial availability and a price of around 1000 USD per gram. The successful synthesis of isoprene-d8 can therefore be an advantage for current and future research projects.

In literature [68] a synthesis for isoprene-d8 is documented, starting from carbide and deuterated water (see reaction scheme in fig. 2.19).

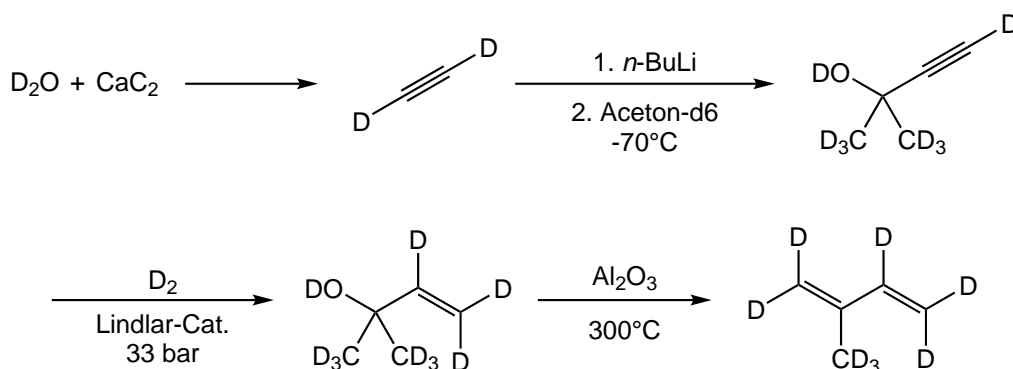


Figure 2.19.: The reaction scheme shows a five step synthesis of isoprene-d8, starting from carbide and water.

First steps for a full synthesis of isoprene-d8, following the reaction scheme from figure 2.19 were conducted in the frame of this work. The reaction was conducted with protonated substrates, to be able to evaluate formation and reaction yield with 1H -NMR, but can be performed with deuterated substrates analogously. A more detailed reaction scheme of the executed synthesis is shown in figure 2.20.

Acetylene was generated by adding H_2O to slivers of calcium carbide (CaC_2). The gas was transferred to a round flask with cold THF ($-70^\circ C$), where it dissolved almost completely (no increase in gas volume within the reaction setup was

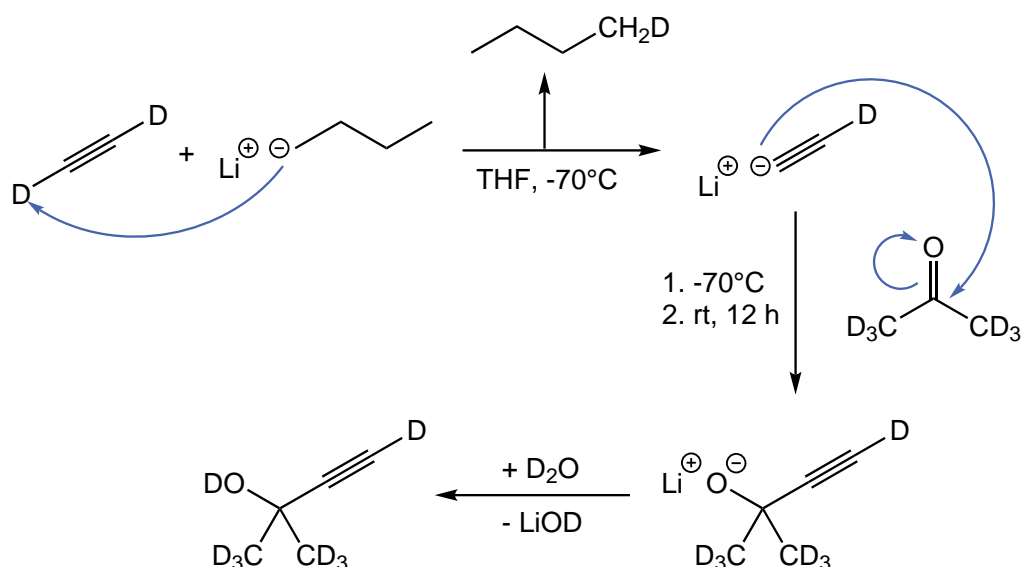


Figure 2.20.: Detailed reaction scheme for synthesis of the isoprene precursor, starting from acetylene.

detected by the connected bubble counter). After the reaction was completed and all acetylene was collected in the THF, *n*-butyl lithium (*n*-BuLi) was carefully added dropwise. The reaction mixture was kept below $-70\text{ }^{\circ}\text{C}$ to avoid formation of di-lithio acetylide. Afterwards, acetone was added dropwise, keeping the temperature below $-70\text{ }^{\circ}\text{C}$. The solution was stirred for another 15 min before the cooling bath was removed and the mixture was stirred overnight at room temperature. H_2O was added slowly to form the final alcohol, 2-methyl-but-3-yn-ol. Upon addition of water, the reaction mixture became thick due to precipitating lithium hydroxide. The mixture was filtered, washed with pentane and distilled afterwards. Analysis of the distillate with $^1\text{H-NMR}$ showed the successful formation of the isoprene precursor (fig. 2.21).

Signal peaks at 1.50 ppm ($-\text{CH}_3$), 2.39 ppm ($-\text{H}$) and 2.54 ppm ($-\text{OH}$) are assigned to the precursor molecule. Strong signals for the reaction solvent THF (1.83 ppm and 3.72 ppm) and the acetone educt (2.14 ppm) remain even after distillation. Therefore, the reaction yield could not be determined, since it was not possible to separate the alcohol from the solvent completely within the framework of this

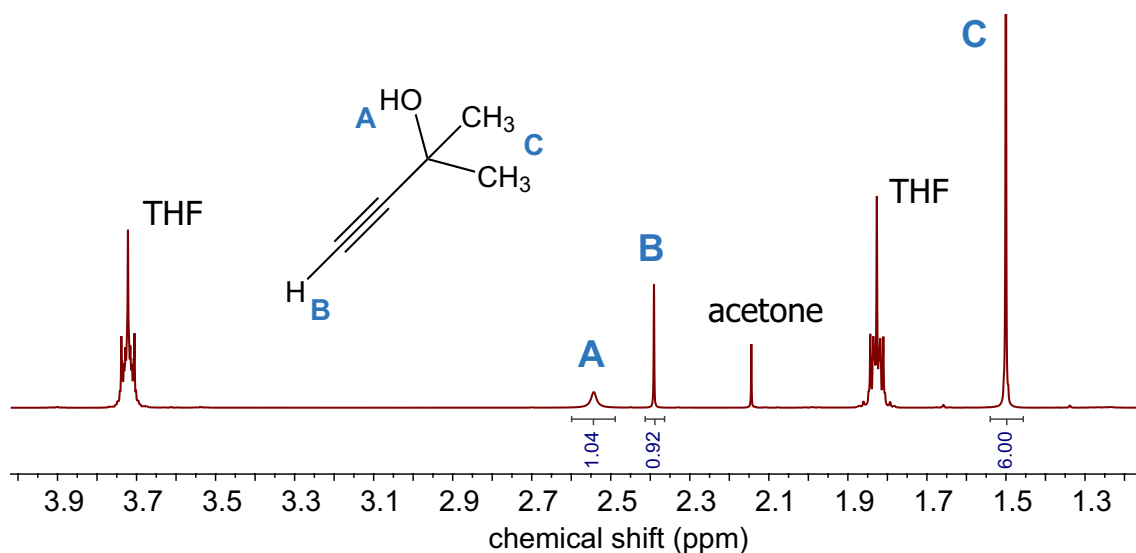


Figure 2.21.: 400 Mhz ¹H-NMR of the isoprene precursor. The reaction scheme is shown in figure 2.20.

thesis (see THF signals in fig. 2.21).

2.6. Conclusion

The synthesis of polyisoprene (PI) model combs with a low branching degree is possible with the grafting-onto method. Introduction of epoxide ring functional groups into the 1,4- microstructure of the backbone was achieved with reproducible reaction yields of 20-30 %. Comb formation was then conducted by ring opening of the epoxide rings. These first experiments show, that the synthesis of partly deuterated polyisoprene combs for investigation on molecular dynamics via double quantum NMR an FT rheology (see section 3.4) is in principle possible. The synthesis and availability of isoprene-d8 monomer is a challenging issue, which is already tackled and partly solved within this thesis.

3. Rheology

Rheology is the science of flow and matter [6, 97, 101]. Through deformation of a body, material specific forces are initiated, that can be detected and investigated. Matter is categorized in a range between ideal viscous (e.g. water) and ideal elastic (e.g. iron). Most materials are partial viscous and partial elastic, so called viscoelastic. This is especially true for polymeric materials. Through rheological experiments, correlations between material response and the molecular structure are revealed. Informations such as molecular weight, molecular weight distribution, various relaxation times, glass transition temperature, and topology are accessible.

Underlying fundamental physics of the polymeric material and the effects on the mechanical behavior, especially at deformations that lead to high shear rates (i.e. the nonlinear regime) are still not fully understood. This chapter focuses on the basics of shear rheology of polymer melts.

3.1. Introduction to Shear Rheology

The basics of rheology can be explained by a two-plate model. A material is placed between two parallel plates of a distance h . The upper plate, having an

3. Rheology

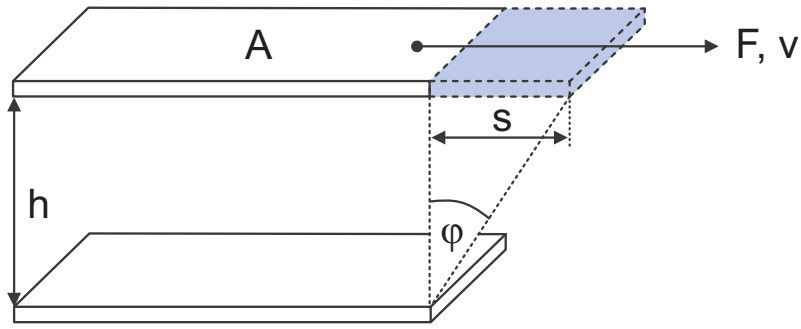


Figure 3.1.: Two-plate shear experiment. A material is placed between two plates, from which the upper plate is moved constantly with a force F [87].

area A , is moved with a constant force F over a distance s . The resulting stress σ , or shear stress, is given by the following equation.

$$\sigma = \frac{F}{A} \quad (3.1)$$

The strain γ is calculated by the deformation s and the distance h of the plates.

$$\gamma = \frac{s}{h} \quad (3.2)$$

The velocity v of the shear movement in this example is decreasing from the upper, moving plate to the bottom plate. Therefore, a time-independent shear rate $\dot{\gamma}$ is defined, which is normalized to the distance h [101].

$$\dot{\gamma} = \frac{d\gamma}{dt} = \frac{v}{h} \quad (3.3)$$

3.1.1. Phenomenological Models

Elasticity - Hooke's Law

The one-dimensional spring model of Hooke can be used for the description of ideal elastic materials (fig. 3.2).



Figure 3.2.: Hooke's spring model for ideal elastic matter. A rotational movement with a constant angular frequency ω is transferred as sinusoidal deformation to an elastic spring.

In this most simplified case, the material stress σ is directly proportional to the deformation γ . The material characteristic proportionality constant G is called the relaxation modulus.

$$\sigma = G \cdot \gamma \quad (3.4)$$

In oscillatory shear, a sinusoidal deformation γ is performed over a time t , with the maximum deformation amplitude γ_0 , and the excitation frequency ω_1 .

$$\gamma(t) = \gamma_0 \cdot \sin(\omega_1 t) \quad (3.5)$$

The time-dependent stress $\sigma(t)$ in phase with the deformation is obtained by combination of eq. (3.5) and eq. (3.4) (see fig.3.3).

$$\sigma(t) = G \cdot \gamma_0 \cdot \sin(\omega_1 t) \quad (3.6)$$

3. Rheology

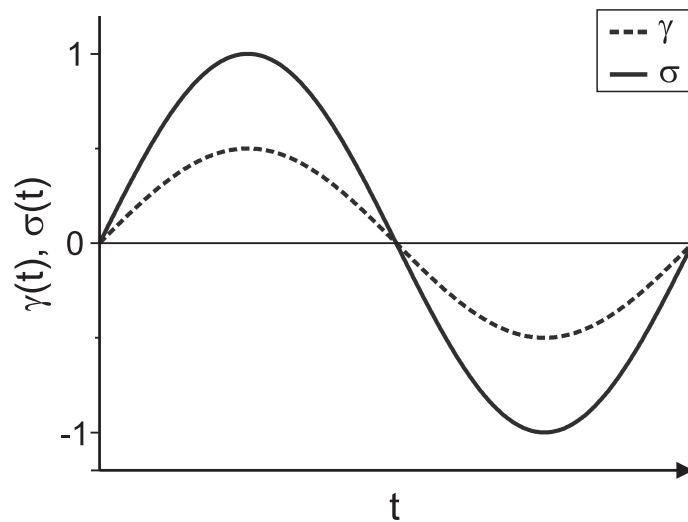


Figure 3.3.: Ideal elastic deformation $\gamma(t)$ and the stress response $\sigma(t)$ in oscillatory shear.

Viscosity - Newton's Law

Ideal viscous matter can be described by a linear dash-pot model, where the force is proportional to the displacement, and energy gets dissipated completely (Newtonian fluid).

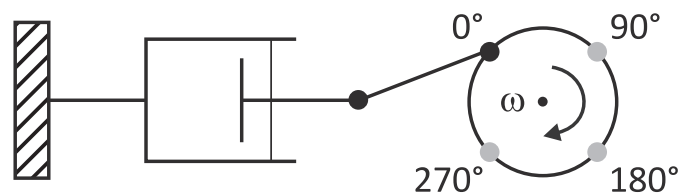


Figure 3.4.: Dash-pot model for ideal viscous materials [101]. A piston is moved back and forth by an initial sinusoidal rotation. The dash-pot damps the movement, which results in a phase shift of the piston towards the movement initiation (see fig. 3.5).

The proportionality between σ and the shear rate $\dot{\gamma}$ is only given, if the temperature is constant. The shear viscosity η is then a material specific property.

$$\sigma = \eta \cdot \dot{\gamma} \quad (3.7)$$

The shear rate $\dot{\gamma}$ in oscillatory shear is the derivative of the time-dependent deformation γ from eq. (3.5).

$$\dot{\gamma}(t) = \frac{d\gamma}{dt} = \gamma_0 \cdot \omega_1 \cdot \cos(\omega_1 t) \quad (3.8)$$

The time-dependent shear stress $\sigma(t)$ is obtained accordingly.

$$\sigma(t) = \eta \cdot \gamma_0 \cdot \omega_1 \cdot \cos(\omega_1 t) \quad (3.9)$$

$$\sigma(t) = \eta \cdot \gamma_0 \cdot \omega_1 \cdot \sin(\omega_1 t + 90^\circ) \quad (3.10)$$

From eq. (3.10) it can be seen, that ideal viscous materials respond with a shear stress $\sigma(t)$ that has a phase shift of 90° to ideal elastic materials (fig. 3.5).

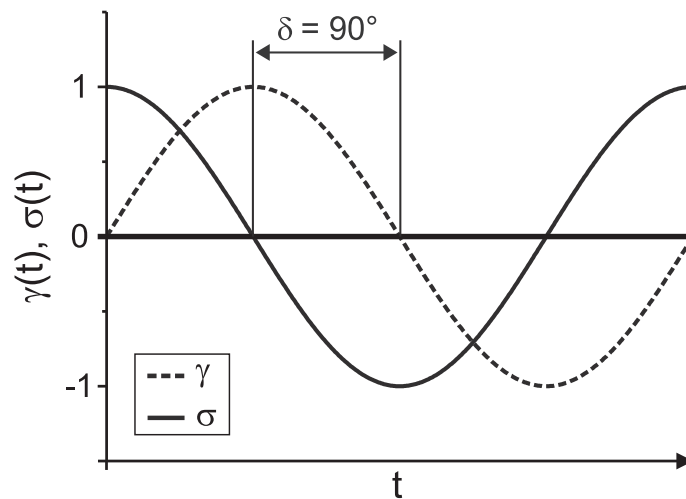


Figure 3.5.: Ideal viscous deformation in oscillatory shear. Stress $\sigma(t)$ and strain $\gamma(t)$ are phase shifted by 90° [101].

Viscoelasticity

Ideal elastic and ideal viscous are marginal cases of reality. Almost every substance contains an elastic and a viscous part. This is called viscoelasticity and can be described by a combination of the linear spring model (Hooke) and the linear

3. Rheology

dash-pot (Newton). The linear, one-dimensional combination is the Maxwell model, the parallel combination is the Kelvin-Voigt model (fig. 3.6).

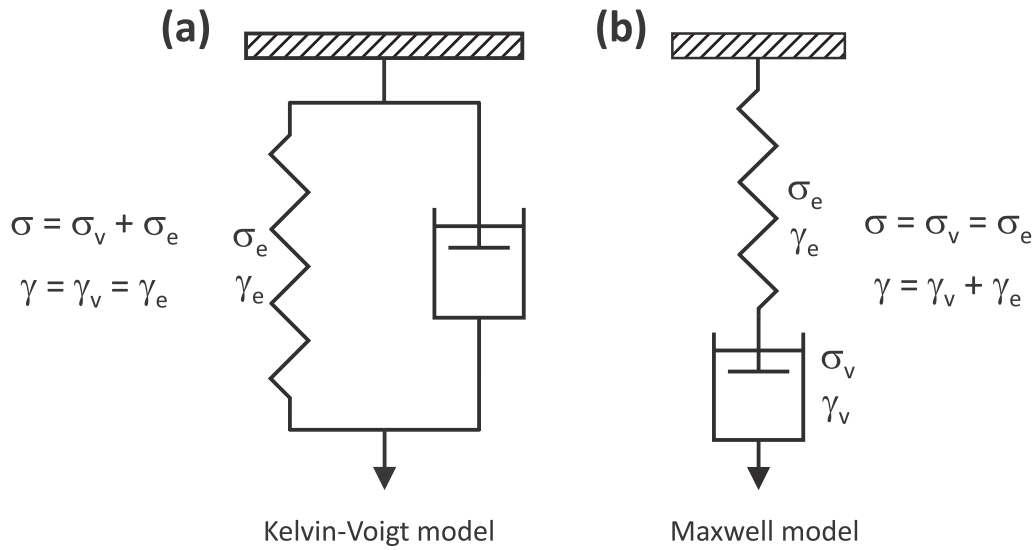


Figure 3.6.: (a) Kelvin-Voigt model for elastic solids with viscous part. (b) Maxwell model for viscous liquids with elastic part [6][87].

Kelvin-Voigt Model

The Kelvin-Voigt model describes an elastic body with low viscous rate (fig. 3.6 a). These bodies are called Kelvin-Voigt solids. The model puts an elastic spring and a dash-pot into parallel position. Relaxation after a strain is complete but time-delayed. The total stress σ consists of the stress σ_e from the spring, and the stress σ_v from the dash-pot (dampener).

$$\sigma = \sigma_e + \sigma_v \quad (3.11)$$

The deformation γ and shear rate $\dot{\gamma}$ are equal in both components over a wide range of cases.

$$\gamma = \gamma_e = \gamma_v; \quad \dot{\gamma} = \dot{\gamma}_e = \dot{\gamma}_v \quad (3.12)$$

Hooke's law (3.4) is valid for the elastic part, and Newton's law (3.7) for the viscous part. Through the combination of both laws, equation (3.11) results a differential equation for the total stress of the system.

$$\sigma = \sigma_e + \sigma_v = \eta \cdot \dot{\gamma}_v + G \cdot \gamma_e = \eta \cdot \dot{\gamma} + G \cdot \gamma \quad (3.13)$$

Maxwell Model

Viscous liquids that own an elastic amount stay partly deformed after an applied strain. This behavior can be described by a dash-pot and a spring in series (fig. 3.6). Substances that follow this model behavior are called Maxwell liquids. The stress τ is equally distributed over all parts of the model.

$$\sigma = \sigma_e = \sigma_v \quad (3.14)$$

The total strain γ and the total shear rate $\dot{\gamma}$ are the summation of spring and dash-pot.

$$\gamma = \gamma_e + \gamma_v \quad (3.15)$$

$$\dot{\gamma} = \dot{\gamma}_e + \dot{\gamma}_v \quad (3.16)$$

Through insertion of Hooke's law (3.4) and Newton's law (3.47) into equation (3.16), Maxwell's differential equation is obtained.

$$\dot{\gamma} = \dot{\gamma}_v + \dot{\gamma}_e = \frac{\sigma_v}{\eta} + \frac{\dot{\sigma}_e}{G} = \frac{\sigma}{\eta} + \frac{\dot{\sigma}}{G} \quad (3.17)$$

3. Rheology

Upon consideration of equation 3.8, the following expression results for the time-dependent shear rate $\dot{\gamma}(t)$ in oscillatory shear.

$$\dot{\gamma}(t) = \frac{\sigma}{\eta} + \frac{\dot{\sigma}}{G} = \gamma_0 \omega_1 \cos(\omega_1 t) \quad (3.18)$$

Following the mathematical solution of this equation, the oscillatory shear stress is calculated, with $\tau = \eta/G$ being the relaxation time.

$$\sigma(t) = \gamma_0 \left(G \frac{(\omega\tau)^2}{1 + (\omega\tau)^2} \sin(\omega t) + G \frac{\omega\tau}{1 + (\omega\tau)^2} \cos(\omega t) \right) \quad (3.19)$$

$$= \gamma_0 (G' \sin(\omega t) + G'' \cos(\omega t)) \quad (3.20)$$

The storage modulus G' describes the reversible deformation energy (elastic amount). The so called loss modulus G'' measures the dissipating deformation energy (viscous amount). G_n^0 is called the plateau modulus (see section 3.2.3). The quotient of the two moduli is the dissipation factor $\tan \delta$.

$$\tan \delta = \frac{G''}{G'} \quad (3.21)$$

$\tan \delta$ has values between zero and ∞ . For $\tan \delta = 0$ an ideal elastic behavior is described. Ideal viscous behavior is reached at $\tan \delta = \infty$. Long relaxation times τ , or short frequencies ω respectively, show a proportionality for the storage and loss modulus from equation (3.19), $G' \propto \omega^2$ and $G'' \propto \omega^1$.

The Maxwell model is valid for monodisperse polymer melts at high measurement temperatures or small excitation frequencies. Polymer melts behave approximately like viscoelastic liquids at small shear rates [101].

3.2. Small Amplitude Oscillatory Shear (SAOS)

Rheometry utilizes small amplitude oscillatory shear (SAOS) to investigate polymer melts in the linear mechanical regime, i.e. at small deformations and shear rates. These experiments yield the storage and loss modulus depending on frequency. From linear master curves of $G'(\omega)$ and $G''(\omega)$, relaxation times of different segment lengths of the molecular chain are accessible. The frequency range of the measurements can be extended with the time-temperature-superposition (TTS) principle.

The following sections describe important material specific features like the entanglement molecular weight M_e , which are obtainable through SAOS experiments of linear polymer melts.

3.2.1. Time-Temperature-Superposition Principle (TTS)

The time-temperature-superposition (TTS) principle enables rheological examination of viscoelastic materials over a wide range of frequencies. Measurements are conducted at different temperatures. The obtained data can then be shifted with respect to a reference temperature T_{ref} , which results a single master curve (fig. 3.7). This is possible because relaxation phenomena depend equally on temperature for viscoelastic materials. The horizontal shift factor a_T along the frequency axis is correlated to the measurement temperature T and to T_{ref} via the William-Landel-Ferry (WLF) equation [128].

$$\log a_T = \frac{-C_1 (T - T_{ref})}{C_2 + T - T_{ref}} \quad (3.22)$$

3. Rheology

C_1 and C_2 are empirical parameters, that become very similar for polymers that are also dynamically similar. For $T_{ref} = T_g$ they become constants for a wide range of materials, $C_1 = 17.44$ and $C_2 = 51.6K$.

Next to the horizontal shift factor a_T , there is a vertical shift factor b_T . Through b_T small vertical differences can be compensated, utilizing the temperature dependent polymer density ρ .

$$b_T = \frac{T_0 \cdot \rho_0}{T \cdot \rho} \quad (3.23)$$

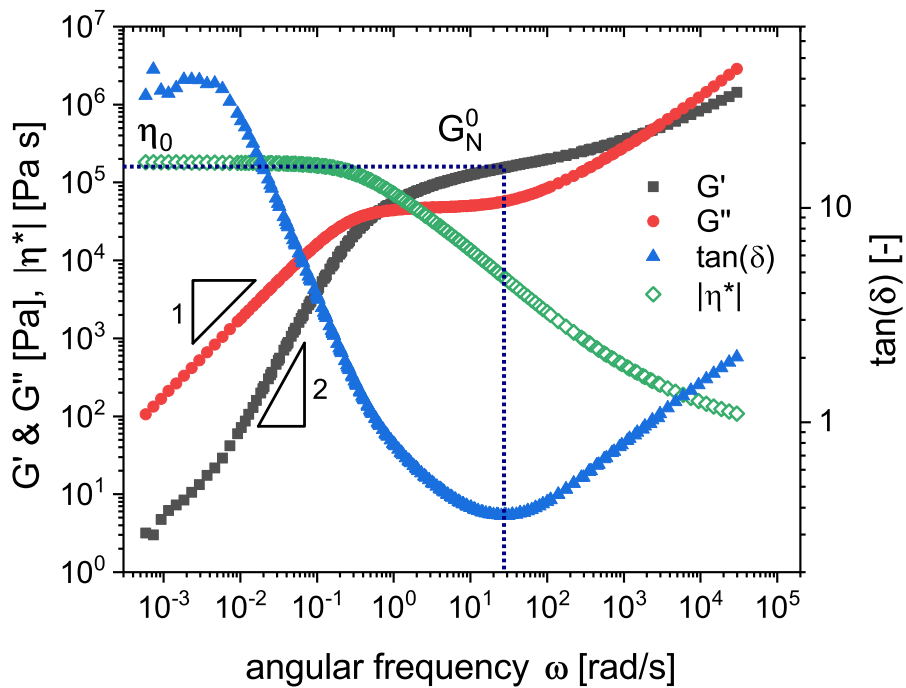


Figure 3.7.: Master curve of the storage (G') and loss modulus (G'') obtained via TTS (linear polystyrene $M_w = 154$ kg/mol, $T_{ref} = 160$ °C). In the terminal regime, at small frequencies, the moduli show scalings of $G' \propto \omega^2$ and $G'' \propto \omega^1$, following the Maxwell model (see eq. 3.19). The plateau modulus G_N^0 is obtained via the minimum of $\tan \delta$.

3.2.2. Critical Molecular Weight and Zero-Shear Viscosity

The dynamics of short polymer chains are governed by Rouse behavior [109]. This means relaxation occurs along the chain, without interference of an outer

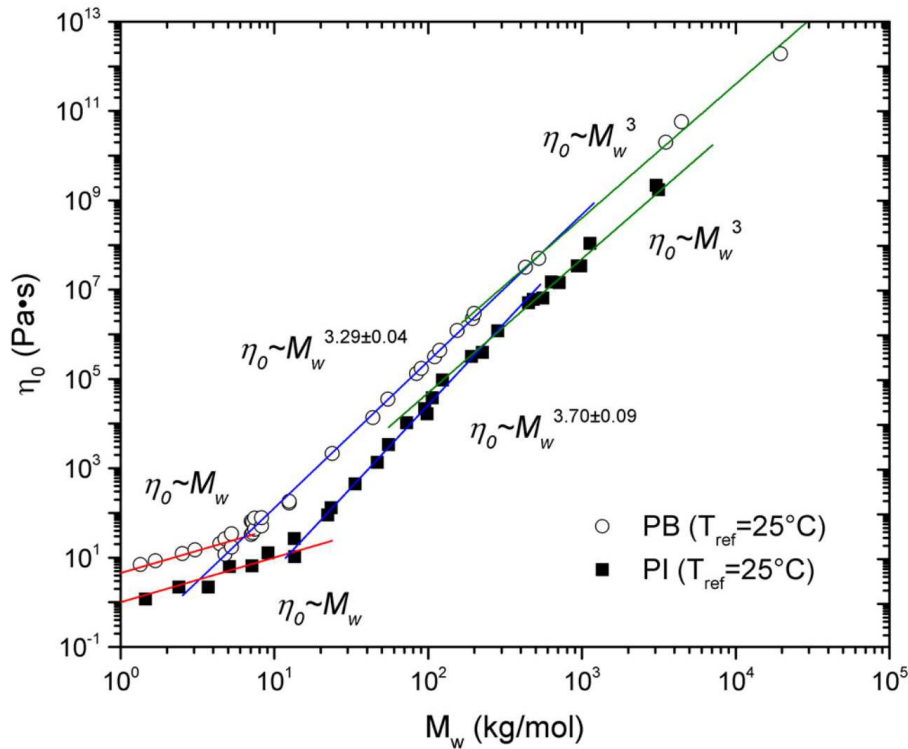


Figure 3.8.: The zero-shear viscosity $\eta_0(M_w)$ for polybutadiene (PB) and polyisoprene (PI). Three different scaling laws are observed, which correspond to three different relaxation mechanisms for polymer melts. The scaling crossovers mark the critical molecular weight M_c and the reptation molecular weight M_r ($M_c < M_r$). Adapted from Unidad and Fetters et al. [118].

matrix. Above a certain molecular weight however, the presence of entanglements dominates mechanical behavior. This becomes very apparent in the zero-shear viscosity η_0 (fig. 3.8). Following Rouse theory, at low molecular weight the zero-shear viscosity is predicted to be proportional to M_w .

$$\eta_0 \propto M_w \quad \text{for} \quad M_w < M_c \quad (3.24)$$

Above a certain threshold, called the critical molecular weight M_c , the scaling changes to 3.4 for typical linear homopolymer melts. In this region, reptation, contour length fluctuation (CLF, section 3.3.4) and constraint release (CR, section 3.3.5) are used as explanation [77, 86, 89]. As the molecular weight increases above M_c , entanglements restrict dynamic movements of the molecular chains

3. Rheology

and thus the zero-shear viscosity increases.

$$\eta_0 \propto M_w^{3.4} \quad \text{for} \quad M_c < M_w < M_r \quad (3.25)$$

The critical molecular weight M_c varies between values of 2 - 4 M_e [27], where M_e is the entanglement molecular weight.

For sufficiently long chains, again a different scaling exponent of 3 is observed. The usual explanation is, that the influence of CLF and CR is diminishing, and the mechanical behavior is based purely on reptation. This second transition is marked by the reptation molecular weight M_r .

$$\eta_0 \propto M_w^3 \quad \text{for} \quad M_r < M_w \quad (3.26)$$

For *cis*-1,4-PI the reptation molecular weight M_r is above 220 kg/mol [70]. Equations (3.24), (3.25) and (3.26) allow to infer the molecular weight for a monodisperse polymer from the zero-shear viscosity η_0 .

3.2.3. Plateau Modulus

The storage modulus $G'(\omega)$ of well entangled polymer melts shows a constant value (a plateau) over a wider frequency range. This plateau is called the plateau modulus G_N^0 , and extends with increasing molecular weight of the polymer. G_N^0 is proportional to the density of entanglements of the polymer melt, and is polymer specific as well [6]. This can be seen in $G'(\omega)$ plots of varying molecular weight (fig. 3.9).

For low molecular weight polymers, a plateau cannot be observed, because they are not entangled. With increasing molecular weight, the entanglements delay

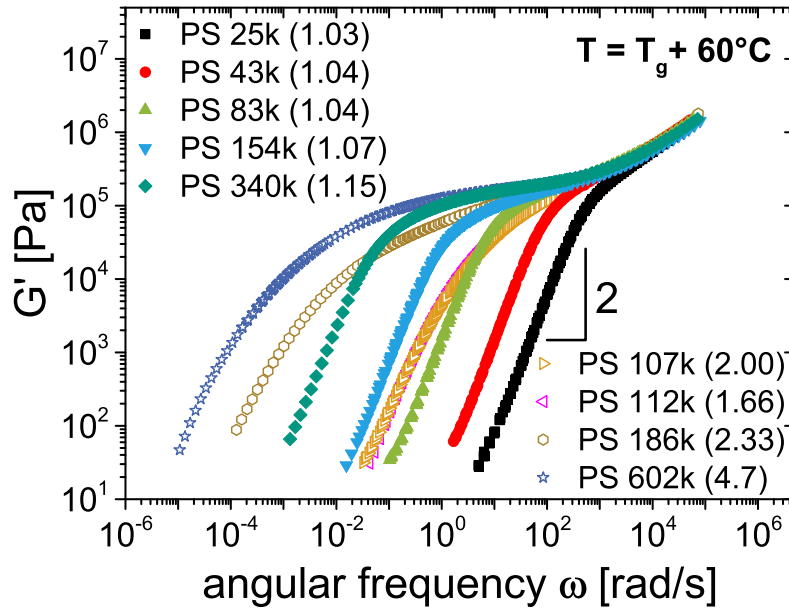


Figure 3.9.: Storage shear modulus G' of linear polystyrene melts with different molecular weight and PDI (given in brackets) as a function of angular frequency ω , nominated to a reference temperature of $T_g + 60^\circ\text{C}$ (adapted from [76]).

the final relaxation of the polymer chains, which results in a wider plateau of $G'(\omega)$. Compared to the viscosity $\eta(\omega)$ and the relaxation time $\tau(\omega)$, G_N^0 is relatively independent of temperature (see also section 3.2.1) and the absolute molecular weight, if $M_w \gg M_c$. However, since the terminal relaxation time τ_0 is roughly proportional to the zero-shear viscosity η_0 , i.e. $\eta_0 \propto G_N^0 \tau_0$ (see section 3.3.3), τ_0 is also proportional to the molecular weight M_w above the critical molecular weight M_c [6].

$$\tau_0 \propto \eta_0 \propto M_w^{3.4} \quad \text{for } M_w > M_c \quad (3.27)$$

Differently long molecular chains can escape their entanglements at different times, meaning they have varying relaxation times τ_0 . Hence, polydisperse melts show a gradual slope of $G'(\omega)$ instead of a flat plateau. The shape of $G'(\omega)$ especially, contains therefore information about the molecular weight distribution.

3.2.4. Entanglement Molecular Weight

Following the remarks of section 3.2.3, the plateau modulus G_N^0 is related to the entanglements of a polymer melt (also see fig. 3.10 in section 3.3). It can be used to calculate the entanglement molecular weight M_e .

$$M_e^F = \frac{\rho RT}{G_N^0} \quad (3.28)$$

$$M_e = \frac{4 \rho RT}{5 G_N^0} \quad (3.29)$$

Equation (3.28) was defined by Ferry [27], whereas equation (3.29) considers fast Rouse modes which allow re-equilibration of tension along the chain before entanglements come into effect [85, 88]. This reduces the value of G_N^0 by one fifth [6, 110, 115].

In this work, definition (3.29) is used for the calculation of the entanglement molecular weight M_e from linear rheology.

3.3. Dynamics of Entangled Polymers

The majority of investigated samples in this work are well-entangled polymer melts with $M_w > M_e$. The following sections about polymer dynamics therefore focus on entangled polymers.

The motion of a single polymer chain in highly concentrated polymer solutions or polymer melts is impeded by topological constraints (fig. 3.10) [6]. A polymer chain is unable to cross through its neighboring chains and thus has to perform certain movements to be able to relax after a deformation. The most important

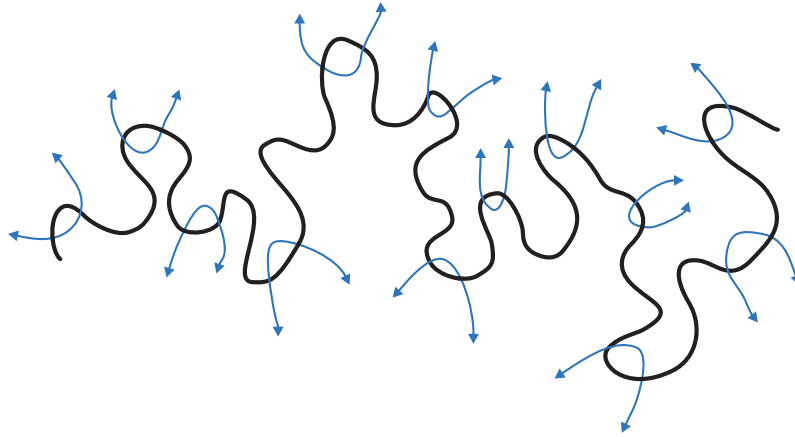


Figure 3.10.: An entangled polymer chain (black line), surrounded by a matrix of other polymer chains (blue lines).

relaxation processes are reptation, primitive path fluctuations and constrain release, and are described in the following sections.

3.3.1. Tube Model

Edwards introduced the idea of a fixed polymer chain, which is “hedged in by the other chains” [84]. This theory was later extended by deGennes [86], and by Doi and Edwards [78–81], and is known as the tube model. This model imagines the dynamics of a polymer chain as a motion confined in a tube. The tube is build by surrounding molecules that put a topological constrain on the movement of a given polymer strand because they cannot cross (entanglement). This forces the chain to move along the axis of the tube, called the primitive path or contour length (fig. 3.11). This simple tube model already allows to describe the properties, such as the viscosity, of entangled polymers , e.g. polymer melts, quantitatively to a large degree [115].

The width of the confining tube is the tube diameter a . If the molecular chain has time to relax (i.g. no shear flow), it will have the configuration of a random walk, and so will the tube. Within the tube, the polymer chain meanders and thus

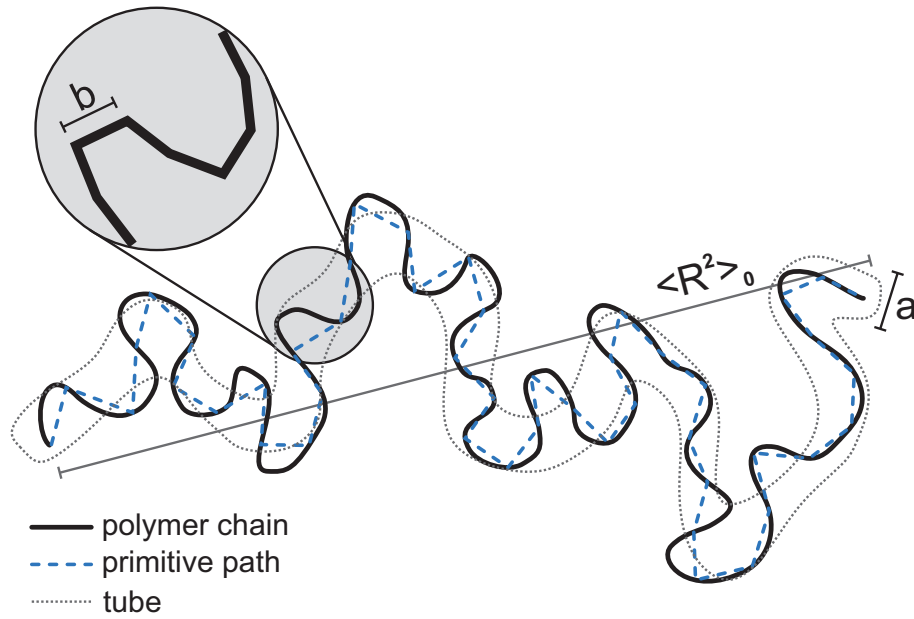


Figure 3.11.: Surrounding constrains form a tube-like region, in which the entangled polymer chain meanders. The primitive path of the tube is a random walk with step size a , equal to the diameter of the tube. The contour length of the tube is much smaller than the contour length of the molecular chain, which has a statistical segment length b . Adapted from Graessley [89].

the contour length L_{tube} of the tube is shorter than the contour length L of the molecule [6]. On the other hand, the tube diameter a is wider than the statistical segment length b of the chain. It can be interpreted as the end-to-end distance of an entanglement strand of N_e monomers [110]:

$$a = b\sqrt{N_e} \quad (3.30)$$

Where $b \equiv \sqrt{\langle R^2 \rangle_0 / N}$ is the statistical segment length, which is defined by the mean-square end-to-end distance $\langle R^2 \rangle_0$ and the degree of polymerization N of the molecule. An entanglement strand is the molecular distance between two constraints of the surrounding matrix and thus directly proportional to the entanglement molecular weight M_e (see section 3.2.4). Therefore, the tube diameter a is directly related to M_e and the molecular weight of the monomer M_0 , and

equation 3.30 can be rewritten as follows.

$$a^2 = b^2 \frac{M_e}{M_0} = b^2 \frac{4}{5} \frac{\rho RT}{G_N^0} \frac{1}{M_0} \quad (3.31)$$

According to eq. 3.31 the smaller M_e , the smaller the tube diameter a . This agrees with the general rule of thumb, that bigger substituents on a monomer lead to larger entanglement molecular weights and wider tube diameters; for example for 1,4 - polybutadiene $a = 36.8 \text{ \AA}$ and for polystyrene $a = 76 \text{ \AA}$ [6]. Typically, this results in 100 to 200 monomers between two entanglements (M_e).

3.3.2. Equilibration Time

In tube theory it is assumed, that all relaxation processes in the melt are controlled by the monomeric friction coefficient ζ . The monomeric friction coefficient ζ is independent of molecular weight, polymer specific and mainly depends on temperature. It is used to define the equilibration time τ_e , which is the Rouse reorientation time required to relax a chain part, that occupies a single tube segment a [6].

$$\tau_e = \frac{\zeta a^2 M_e}{3\pi^2 k T M_0} \quad (3.32)$$

3.3.3. Reptation

A polymer chain can dynamically move out of its tube by reptation [86]. In this process the chain meanders, which leads to a partial abandonment of the old tube by escaping its entanglements (fig. 3.12).

At the same time, new entanglements are formed, thus a new tube is created. If reptation is the only considered relaxation of an entangled polymer chain, the

3. Rheology

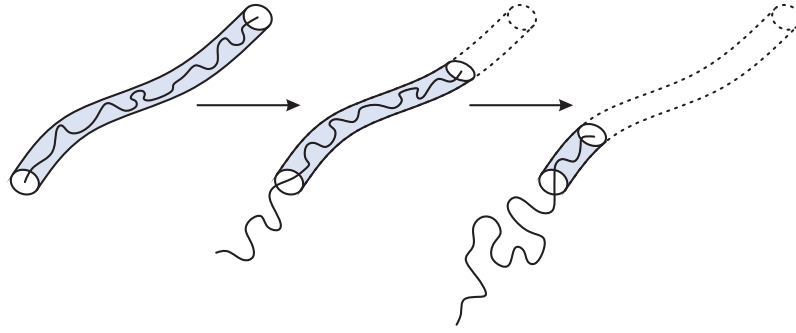


Figure 3.12.: Reptation of a polymer chain out of its tube. During the process, the chain escapes its old tube (dotted line) and forms new entanglements with surrounding polymer chains.

relaxation modulus $G(t)$ is given by the following equation.

$$G(t) = \sum_{i_{odd}} G_i e^{-t/\tau_i} \quad (3.33)$$

The distributions of relaxation modes G_i results the plateau modulus G_N^0 , and the relaxation times τ_i are defined by the reptation time or disengagement time τ_d , which is also the longest relaxation time τ_0 .

$$G_i = \frac{8}{\pi^2} \frac{G_N^0}{i^2} \quad i_{odd} \quad (3.34)$$

$$\tau_i = \frac{\tau_d}{i^2} \quad i_{odd} \quad (3.35)$$

The disengagement time τ_0 is the time, the molecule needs to fully escape its former tube. It can be calculated, using the monomeric friction coefficient ζ , the statistical segment length b , the degree of polymerization N , and the tube diameter a .

$$\tau_0 = \frac{\zeta N^3 b^4}{\pi^2 k T a^2} = 3Z^3 \tau_e \quad (3.36)$$

The zero-shear viscosity η_0 can be calculated from the discrete relaxation times spectrum.

$$\eta_0 = \sum_{i_{odd}} G_i \tau_i \quad (3.37)$$

Taking into account, that the sum in equation (3.37) converges rapidly, it is stated that the zero-shear viscosity η_0 is dominated by the first term, which implies the longest relaxation time τ_0 . From equation (3.36) it can be seen, that the longest relaxation time τ_0 is very sensitive to the number of entanglements Z^3 , what carries over to the zero-shear viscosity η_0 due to equation (3.37). This perfectly agrees with experimental results of $\eta_0(M_w)$ for very high molecular weights above the reptation molecular weight M_r (see section 3.2.2).

The storage modulus $G'(\omega)$ and the loss modulus $G''(\omega)$ for pure reptation can also be predicted from the discrete relaxation times spectrum $\{G_i, \tau_i\}$ by the following equations (also compare to Maxwell model, eq. 3.19).

$$G'(\omega) = \sum_i G_i \frac{(\omega\tau_i)^2}{1 + (\omega\tau_i)^2} \quad (3.38)$$

$$G''(\omega) = \sum_i G_i \frac{(\omega\tau_i)}{1 + (\omega\tau_i)^2} \quad (3.39)$$

Predictions of $G'(\omega)$ and $G''(\omega)$, considering only pure reptation from equations (3.38) and (3.39) are plotted in figure 3.13. It can be seen that for higher frequencies, or more precisely for relaxation times smaller than the longest relaxation time τ_0 , $G''(\omega)$ falls off too rapidly compared to experimental data. Therefore, other relaxation processes besides pure reptation need to be considered [6, 110, 115].

3.3.4. Primitive Path Fluctuations

Another possible relaxation process for polymer chains is primitive path fluctuation (PPF) or contour length fluctuation (CLF). In section 3.3.1 the primitive path or contour length was defined as the length of the occupied tube of the chain. The diameter a of the tube is much smaller than the length L_{tube} . Because the chain

3. Rheology

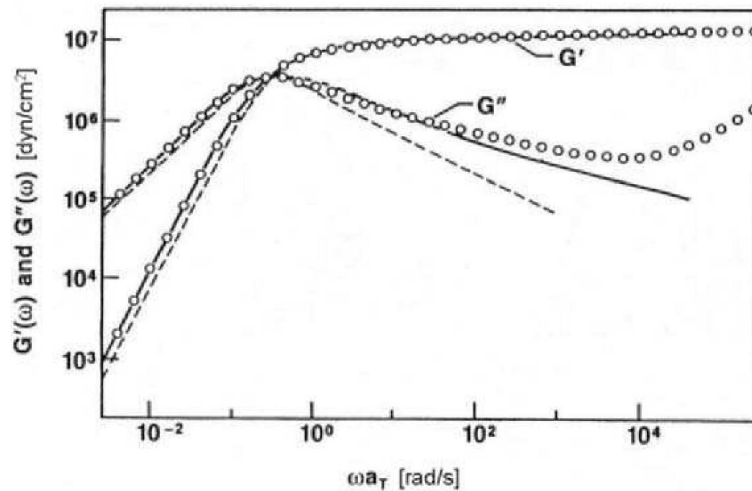


Figure 3.13.: Storage and loss modulus of a monodisperse polybutadiene melt ($M_w \approx 360$ kg/mol). The dashed lines show prediction of G' and G'' with only reptation as relaxation process. Solid lines include reptation and primitive path fluctuations (see section 3.3.4). Adapted from Pearson [106].

meanders within the tube, it gets folded, starting from each end (fig. 3.14). Due to Brownian motion the degree of folding changes randomly. By chance, the end of the chain therefore can fold more than usual and vacates the outer part of the tube. In this moment, the stress associated with the now vacated part is released. When the chain end pushes outwards again, new random tube segments are created. Primitive path fluctuations relax the ends of a molecular chain very rapidly, but the inner parts not so fast, because it is very unlikely for the chain to fold up this much, as this is entropically unfavored.

For linear polymers, reptation and PPF occur simultaneously. Because PPF are slow for the middle part of a chain, its relaxation is dominated by reptation. The outer ends of the molecule however relax at shorter times (higher frequencies) due to PPF. The PPF mechanism shortens the effective tube for the molecule, which leads to a faster relaxation time for the inner segment, too. As a result, the longest relaxation time and the zero-shear viscosity are lower than without the consideration of PPF. Predicted values of the zero-shear viscosity η_0 with and without PPF merge at high molecular weights, where the influence of PPF is di-

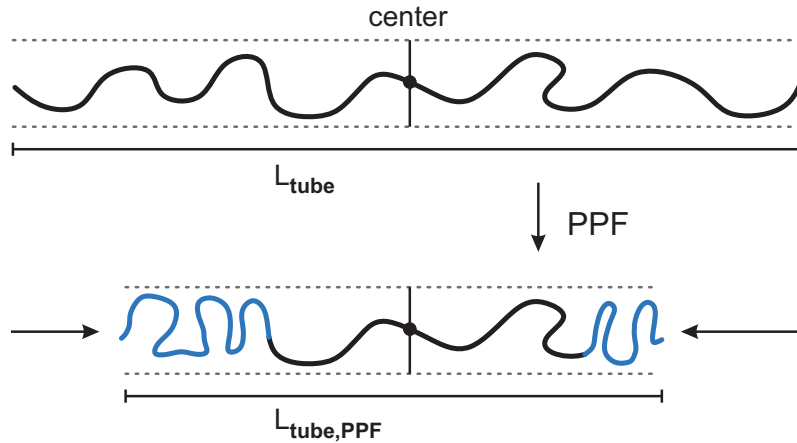


Figure 3.14.: Primitive path fluctuation of a linear chain. The outer ends of the chain (blue) move towards the center. During this process, the terminal ends of the tube get lost and the chain ends relax. When the ends extend again, new random tube regions are formed.

minishing ($M/M_e > 100$, fig. 3.15). Between the critical molecular weight M_c and the reptation molecular weight M_r , $M_c < M_w < M_r$ (see also section 3.2.2), reptation plus PPF can predict the experimentally observed scaling of $\eta_0 \propto M_w^{3.4}$. The inclusion of PPF also broadens the relaxation time spectrum, which leads to a less steep decrease of $G''(\omega)$ in the rubber region, than with reptation alone (fig. 3.13).

3.3.5. Constraint Release

Reptation and primitive path fluctuation regard a test chain in a tube, entangled with a static matrix of surrounding polymer chains. However, each one of the surrounding chains is also moving, and is undergoing reptation and primitive path fluctuation at the same time. When a surrounding chain reptates, it releases constraints on the test chain (fig. 3.16). The test chain can relax more easily as a result. It should be mentioned, that this simple reptation model is not self consistent, as the polymer matrix chains are considered static and reptating at the same time.

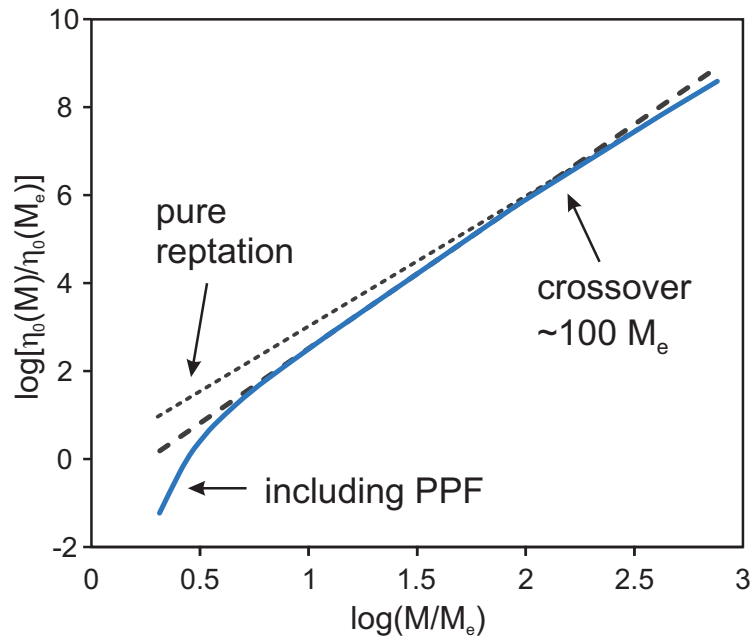


Figure 3.15.: Predictions of the zero-shear viscosity η_0 as function of the number of entanglements M/M_e . The empirical formula $\eta_0 \propto M^{3.4}$ (dashed line) is compared to pure reptation (dotted line) and reptation with primitive path fluctuations (solid thick line). Adapted from Larson [6].

The effect of constraint release (CR) is very complex and most important for polydisperse linear or branched polymers. Dynamics of monodisperse, linear polymers turned out to be only slightly influenced [6]. Simply explained, shorter chains diffuse much faster than long chains can reptate, and release constraints more readily [94].

3.4. FT Rheology in the Nonlinear Mechanical Regime

The application of Fourier Transformation on a time-dependent stress $\sigma(t)$ or normal force signal $N_f(t)$ of an oscillatory shear experiment with the excitation frequency $\omega_1/2\pi$ is called FT rheology. It is important to optimize the recording of the time signal with regard to external disturbance, meaning minimizing signal

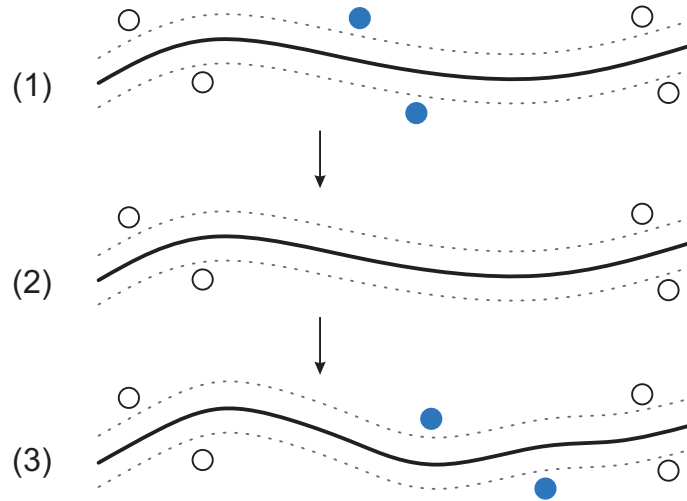


Figure 3.16.: Illustration of constraint release (CR) of a polymer test chain (thick line). Circles represent sidewise constraints via the polymer matrix. Due to relaxation of some polymer chains (full circles), relaxation of the test chain is increased.

contributions that are not coming from the sample response. Only then will it be possible to identify nonlinear material effects, which appear in the spectrum besides the excitation frequency. Techniques to increase the signal to noise ratio (S/N) in FT rheology, and to improve the recording of raw time data and obtain artifact-free spectra are provided elsewhere in detail [5, 15, 82, 91, 125, 127].

3.4.1. Fourier Transformation - Introduction

This section covers the basic fundamentals of Fourier Transformation (FT) that are needed to utilize FT rheology. Detailed description is given in several articles and textbooks [15, 73, 74, 102, 125–127, 129].

With Fourier Transformation it is possible to decompose any continuous, aperiodic function $f(x)$ into its continuous spectrum $F(y)$ with equation (3.40) [74]. It is also possible to recover the original function by a reverse Fourier transform,

3. Rheology

called Fourier synthesis, eq. (3.41).

$$F(y) = \int_{-\infty}^{+\infty} f(x)e^{-iyx} dx \quad (3.40)$$

$$f(x) = \frac{1}{2\pi} \int_{-\infty}^{+\infty} F(y)e^{+iyx} dy \quad (3.41)$$

It is mostly used in signal processing to transform a discrete signal from the time domain into the frequency domain $f(t) \rightarrow F(\omega)$. In this case, instead of a continuous function, a dataset consists of discrete, limited points. The Discrete Fourier Transformation (DFT) simply assumes a periodic continuation of the recorded data.

For experimental FT rheology, a half sided, discrete, complex, magnitude FT is used on the time-dependent stress signal $\sigma(t)$ of an oscillatory shear experiment [15]. It is presumed that the sample composition does not change significantly during the time scale of the deformation period T . This means that $\sigma(t)$ can be projected in a spectrum with respect to the different frequencies $\omega/2\pi$, amplitudes and phases [15]. It is possible because of an important mathematical property of the FT, its linearity.

$$a \cdot f(t) + b \cdot g(t) \longleftrightarrow a \cdot F(\omega) + b \cdot G(\omega) \quad (3.42)$$

This means, that a superposition of different signals in the time domain will result in a superposition in the frequency domain. The FT is inherently complex. As a result, even a real data set $s(t)$ will result a complex spectrum $S(\omega)$ with a real (Re) and imaginary part (Im). A complex spectrum can also be represented by a

3.4. FT Rheology in the Nonlinear Mechanical Regime

magnitude $m(\omega)$ and a phase $\phi(\omega)$ (eqs. 3.43, 3.44 and fig. 3.17).

$$m(\omega) = \sqrt{\text{Re}(F(\omega))^2 + \text{Im}(F(\omega))^2} \quad (3.43)$$

$$\tan(\phi(\omega)) = \frac{\text{Im}(F(\omega))}{\text{Re}(F(\omega))} \quad (3.44)$$

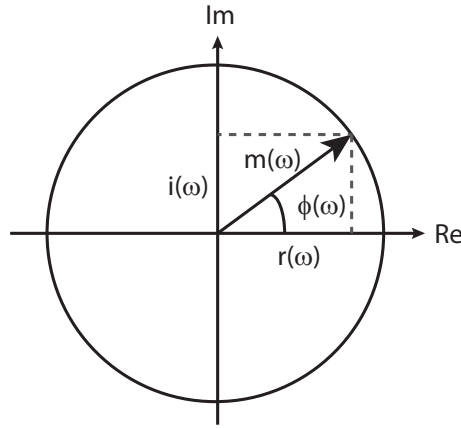


Figure 3.17.: Depiction of a complex number with real (Re) and imaginary part (Im), or magnitude (m) and phase (ϕ) in the complex plane, respectively.

Due to the Euler relation $\exp(i\phi) = \cos(\phi) + i \sin(\phi)$, eq. (3.40) can also be separated into a Fourier cosine and a Fourier sine.

$$F(y) = \int_{-\infty}^{+\infty} f(x) \cos(yx) + f(x)i \sin(yx) dx \quad (3.45)$$

Experimental data is recorded digitally in discrete data points (where N is the number of recorded points) with a fixed increment t_{dw} (dwell time, or inverse sampling rate) for a total time $t_{aq} = t_{dw} \cdot N$ (acquisition time) of the experiment. Therefore, a discrete FT (DFT) is used along half the integral limits $t = 0$ to $t = +\infty$ (half sided FT). The DFT generates N discrete complex points in the frequency spectrum, when N discrete real or complex points in the time domain are transformed. The spectral width, respectively the maximal detectable frequency,

3. Rheology

is called the Nyquist frequency ν_{max} and is given by the sampling rate [15].

$$\nu_{max} = \frac{\omega_{max}}{2\pi} = \frac{1}{2t_{dw}} \quad (3.46)$$

The spectral resolution, meaning the interval between two points in the frequency spectrum, is defined by $\Delta\nu = 1/t_{aq}$.

3.4.2. Fourier Transformation of a Time-Dependent Stress Signal

The most simple one dimensional flow of a viscous fluid under a constant shear rate is described by Newton's law (also see eq. 3.7).

$$\sigma = \eta \cdot \dot{\gamma}. \quad (3.47)$$

For non-Newtonian fluids, the viscosity η is a function of the applied shear rate $\dot{\gamma}$. Due to symmetry, the viscosity η is independent of direction of shear, and therefore: $\eta = \eta(\dot{\gamma}) = \eta(-\dot{\gamma}) = \eta(|\dot{\gamma}|)$. For small shear rates, respectively small strain amplitudes, the viscosity can be expanded via an even Taylor series with respect to shear rate.

$$\eta(\dot{\gamma}) = \eta_0 + c_1 \cdot \dot{\gamma}^2 + c_2 \cdot \dot{\gamma}^4 + \dots . \quad (3.48)$$

In oscillatory shear, η_0, c_1, c_2, \dots might become complex numbers to account for the relative phase shift. The time-dependent strain for oscillatory shear experiments is given in a simplified complex notation:

$$\gamma(t) = \gamma_0 \cdot e^{i\omega_1 t} \quad (3.49)$$

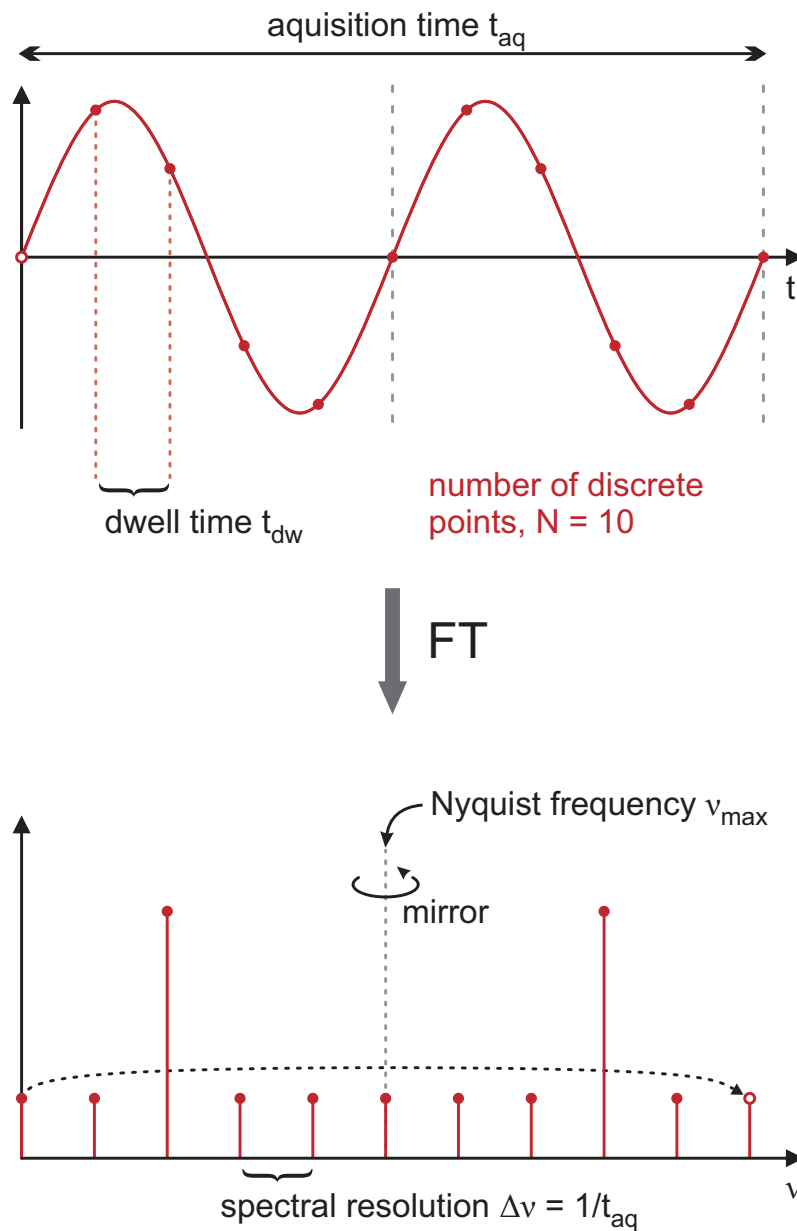


Figure 3.18.: Schematic discrete Fourier Transformation (DFT) of a sinusoidal signal. Exemplary, the recording of 10 data points of two cycles for an acquisition time $t_{aq} = 1$ s leads to 10 points in the frequency spectrum with a spectral resolution of 1 Hz, a Nyquist frequency of 5 Hz and a signal at the excitation frequency $\nu_1 = 2$ Hz.

3. Rheology

The shear rate is given by the time derivative of eq. (3.49):

$$\dot{\gamma}(t) = i\omega_1\gamma_0 \cdot e^{i\omega_1 t}. \quad (3.50)$$

Insertion of eq. (3.48) in eq. (3.47) results in the shear stress σ given as a function of shear rate $\dot{\gamma}$:

$$\sigma(\dot{\gamma}) = (\eta_0 + c_1 \cdot \dot{\gamma}^2 + c_2 \cdot \dot{\gamma}^4 + \dots) \cdot \dot{\gamma}. \quad (3.51)$$

Substitution of the shear rate $\dot{\gamma}$ by eq. (3.50) results in a time-dependent shear stress:

$$\begin{aligned} \sigma(t) &= (\eta_0 + c_1 \cdot i^2 \omega_1^2 \gamma_0^2 \cdot e^{i2\omega_1 t} + c_2 \cdot i^4 \omega_1^4 \gamma_0^4 \cdot e^{i4\omega_1 t} + \dots) \cdot i\omega_1 \gamma_0 e^{i\omega_1 t} \\ &= \underbrace{\eta_0 \cdot i\omega_1 \gamma_0}_{I_1 \propto \omega_1 \gamma_0} e^{i\omega_1 t} + \underbrace{c_1 \cdot i^3 \omega_1^3 \gamma_0^3}_{I_3 \propto \omega_1^3 \gamma_0^3} e^{i3\omega_1 t} + \underbrace{c_2 \cdot i^5 \omega_1^5 \gamma_0^5}_{I_5 \propto \omega_1^5 \gamma_0^5} e^{i5\omega_1 t} + \dots \end{aligned} \quad (3.52)$$

Fourier Transformation of the time dependent stress should consequently consist of peak signals at the odd higher harmonics of the excitation frequency $\omega_1/2\pi$ in the frequency spectrum.

The intensity of the third harmonic I_3 from eq. eqrefeq:shearStress was chosen as a sensitive quantity toward mechanical nonlinearity. To partly compensate experimental variations, I_3 is normalized to the stress response I_1 at the excitation frequency ω_1 , which results in an intensive property $I_{3/1}(\gamma_0, \omega_1) := I_3/I_1$. This enhances reproducibility in a way, that these experimental errors, as for example inhomogeneities of the sample or incorrect loading and trimming, are mainly compensated, since they equally influence the different harmonic intensities. From eq. (3.52) it is expected, that $I_1 \propto \gamma_0^1$ and $I_3 \propto \gamma_0^3$, which concludes in a quadratic scaling law of $I_{3/1} \propto \gamma_0^2$ at low strain amplitudes.

3.4.3. Intrinsic Nonlinearity

The nonlinear parameter ${}^3Q(\omega, \gamma_0)$ and the intrinsic nonlinearity ${}^3Q_0(\omega)$, at low strain amplitudes, were defined by Hyun et al. [23] as follows.

$$\lim_{\gamma_0 \rightarrow 0} {}^3Q(\omega, \gamma_0) \equiv {}^3Q_0(\omega) \quad \text{with} \quad {}^3Q(\omega) \equiv \frac{I_{3/1}}{\gamma_0^2} \quad (3.53)$$

Using the simplified definition of I_1 and I_3 from eq. (3.52), an expression for ${}^3Q_0(\omega)$ is obtained:

$${}^3Q_0(\omega) \propto \frac{c_1}{\eta_0} \omega^2 \quad (3.54)$$

From eq. (3.54), it can be seen, that the intrinsic nonlinearity ${}^3Q_0(\omega)$ is expected to be a function of the zero shear viscosity η_0 , and therefore a function of the molecular weight and the measurement temperature. With the use of the TTS principle (section 3.2.1), intrinsic nonlinear master curves can be generated in analogy to linear master curves, using the same WLF parameters [23, 28]. The TTS principle is expected to be applicable for the intrinsic nonlinearity, since the nonlinear parameter ${}^3Q_0(\omega)$ is a back-extrapolation of ${}^3Q(\omega, \gamma_0)$ to the linear viscoelastic regime at very small amplitudes ($\lim_{\gamma_0 \rightarrow 0}$) [82].

3.4.4. Experimental Aspects of FT Rheology

Experimental measurements of polymer melts show, that I_3 is dominated by a constant noise at low strain amplitudes γ_0 , originating from the rheometer. Consequently at low γ_0 , when $I_1 \propto \gamma_0$ and $I_3 \equiv \text{noise}$, $I_{3/1}(\gamma_0)$ decreases [108] with $I_{3/1} \propto \gamma_0^{-1}$, and reaches a minimum before it increases with the expected scaling of 2, when $I_3 \propto \gamma_0^3$ (fig. 3.19). In this work on polymer melts, this quadratic scaling was observed at medium strain amplitudes (MAOS region), generally

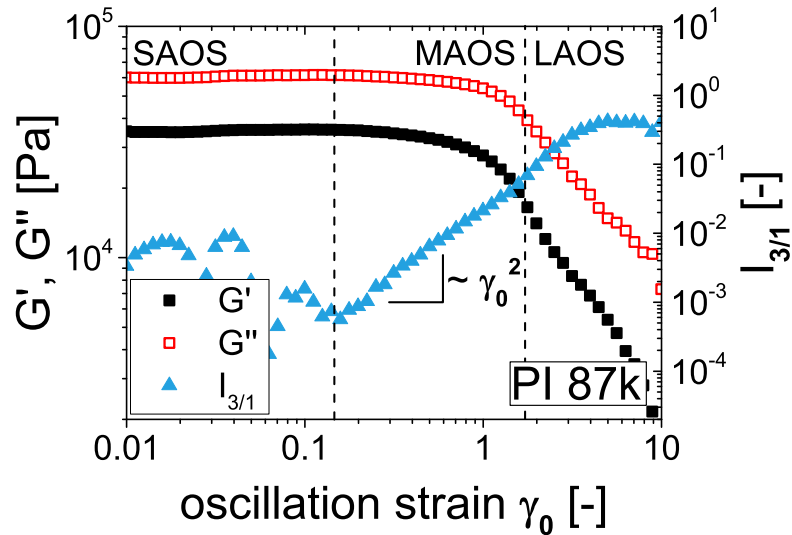


Figure 3.19.: Typical dynamic strain sweep measurement of a linear homopolymer melt (adapted from [76]). At medium strain amplitudes (MAOS) a proportionality of $I_{3/1} \propto \gamma_0^2$ is observed (sample PI 87k, $T = 20^\circ\text{C}$, $\omega_1 = 4 \text{ rad/s}$).

between $0.1 \leq \gamma_0 \leq 1.0$ (see fig. 3.19). However, the exact MAOS region also depended on the polymer, molecular weight, measurement temperature related to T_g , and excitation frequency. Finally, $I_{3/1}$ typically levels off at values around $I_{3/1} \approx 0.1 - 0.2$ at high strain amplitudes (LAOS) [126]. The minimum value that can be reached for $I_{3/1}(\gamma_0)$ highly depends on the signal to noise ratio S/N of the instrument, which limits the application of FT rheology to quantify nonlinearities. For this reason, thorough optimizations have been conducted to maximize S/N up to 10^7 for $I_{3/1}$ of emulsions [127]. Hyun et al. [23] assessed the nonlinear regime for $I_{3/1}(\gamma_0) \geq 5 \cdot 10^{-3}$ in their oscillatory shear tests of polymer melts. With newer instrumentation used in this work, it was possible to reach values for $I_{3/1}(\gamma_0)$ of around one decade lower, with $I_{3/1}(\gamma_0) \geq 5 \cdot 10^{-4}$ (see fig. 3.19). This value is currently a practical limit for the beginning of the medium amplitude oscillatory shear (MAOS) region, followed by the large amplitude oscillatory shear (LAOS) region, where $I_{3/1}(\gamma_0)$ is not proportional to γ_0^2 anymore. The proportionality $I_{3/1}(\gamma_0) \propto \gamma_0^2$ was observed for all linear homopolymer melt samples in this study, regardless of molecular weight, PDI or polymer type.

The general procedure to obtain nonlinear master curves is illustrated schematically in figure 3.20. The raw stress time data of an oscillating shear experiment is

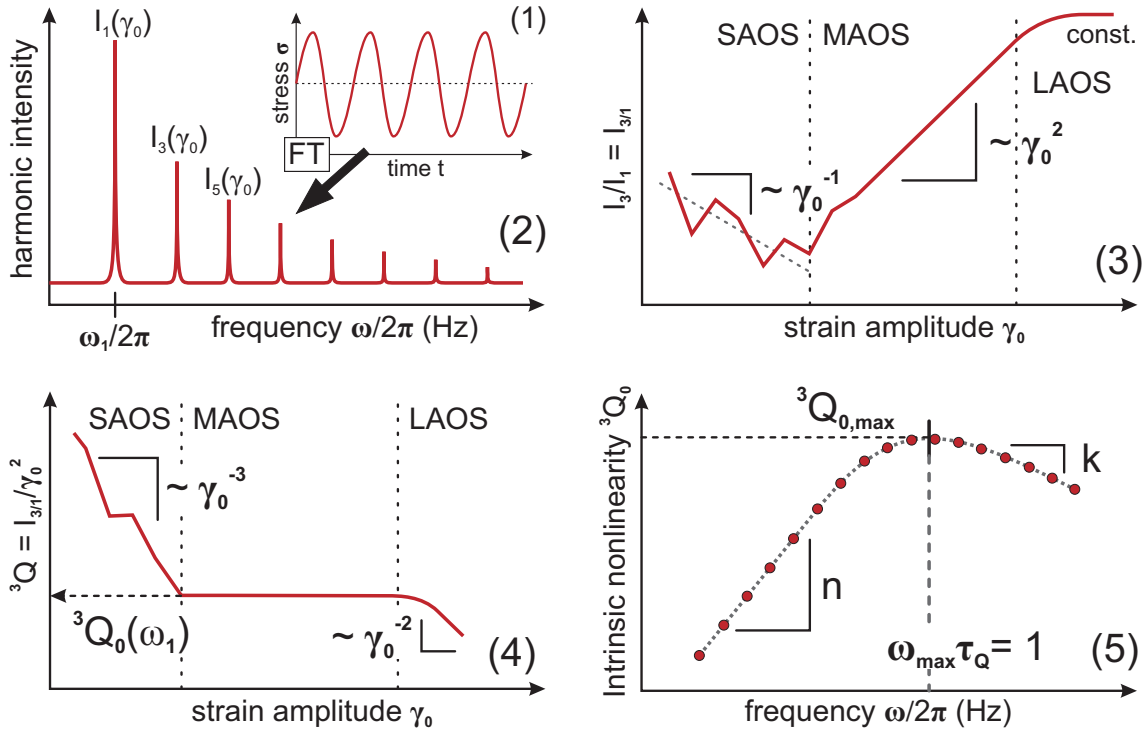


Figure 3.20.: Scheme of a five step procedure from raw data (1) to nonlinear master curve (5). (1) Nonlinear stress time data of an oscillatory shear experiment. (2) After Fourier Transformation of the time data, a magnitude frequency spectrum with odd higher harmonics can be obtained. (3) The ratio $I_{3/1}(\gamma_0, \omega_1)$ of the first and third harmonic is proportional to γ_0^2 in the MAOS region. (4) Extrapolation of ${}^3Q(\gamma_0, \omega_1)$ to small amplitudes gives the intrinsic nonlinearity ${}^3Q_0(\omega_1)$. (5) A nonlinear master curve can be created by plotting several ${}^3Q_0(\omega_1)$ values of different excitation frequencies, that are shifted to a reference temperature, utilizing the TTS principle. Adapted from Cziep et al. [76].

recorded and transformed into a frequency spectrum via Fourier Transformation (fig. 3.20, scheme 1 and 2). From the intensities of the first and third harmonics (I_1 and I_3), $I_{3/1}$ is calculated and plotted against the strain γ_0 (fig. 3.20, scheme 3). This procedure is repeated for different frequencies and/or different temperatures to cover a maximum experimental range in the ${}^3Q_0(\omega)$ frequency space. From each $I_{3/1}(\gamma_0)$ plot, the MAOS region with $I_{3/1} \propto \gamma_0^2$ is identified and the parameter ${}^3Q(\omega, \gamma_0) = I_{3/1}/\gamma_0^2$ is calculated. In a 3Q versus γ_0 plot, a plateau can be identified, whose average value is extrapolated to infinite small strains, $\gamma_0 \rightarrow 0$,

3. Rheology

and eventually yields ${}^3Q_0(\omega)$, see fig. 3.20, scheme 4. Each ${}^3Q_0(\omega)$ value is plotted against the frequency and a nonlinear master curve is obtained via the TTS principle (fig. 3.20, scheme 5).

4. Intrinsic Nonlinearity in Pom-Pom and MSF Constitutive Equations

Modeling and simulation in polymer rheology has proven to be extremely worthwhile over the last decades [31, 32, 93, 100]. Mathematical and numerical models help to understand and reveal underlying physics of rheological behavior, correlated to polymer properties, such as the monomer, molecular weight, dispersity and topology. The development and refinement of these models and simulations certainly require a close collaboration between experimentalists and theorists. An active communication between both sides is therefore the foundation of further progress in polymer science.

In this chapter, two constitutive models are introduced. Predictions of the Pom-Pom model are compared to the molecular stress function (MSF) model, which leads to a more generalized prediction for the intrinsic nonlinear behavior of linear polymer melts. The new generalized expression then can be used to investigate results from nonlinear shear experiments in chapter 5. The predictions in this chapter were performed by Dr. Mahdi Abbasi.

4.1. Pom-Pom Model

4.1.1. Fundamentals

The Pom-Pom model is a molecular based constitution equation model, and was developed by McLeish and Larson [31] to predict rheological behavior of model branched polymers. An idealized branched molecule, called a "pom-pom", consists of a backbone with two branching points at each end, with a number of q dangling arms per side, respectively (fig. 4.1).

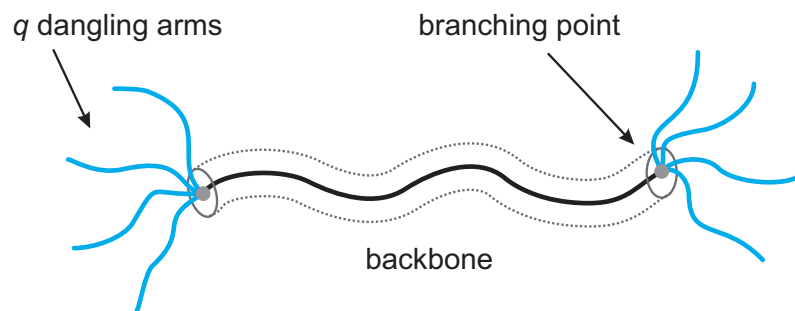


Figure 4.1.: Idealized model Pom-Pom molecule. A number of q dangling arms ("pom-poms") are attached to each end of a linear backbone.

The advantage of the Pom-Pom model is that smaller relaxation times, originating from chain end effects, can be neglected and focus on the slower backbone dynamics is given. The branches are entangled with surrounding molecules, which allows to examine backbone behavior due to orientation and relaxation times in shear and extensional deformation.

The Pom-Pom model features three important relaxation times. The stretch relaxation time of the backbone τ_s and the longest relaxation time (orientation) of the

backbone τ_b , as well as the longest relaxation time of the branches τ_a .

$$\tau_s = Z_b \tau_a(0) q \quad (4.1)$$

$$\tau_b = \frac{4}{\pi^2} Z_b^2 \Phi_b \tau_a(0) q \quad (4.2)$$

$$\tau_a = \tau_0 \exp \left[\frac{15}{4} Z_a \left(\frac{(1-x)^2}{2} - (1-\Phi_b) \frac{(1-x)^3}{3} \right) \right] \quad (4.3)$$

The backbone relaxation τ_b , eq. (4.2), not only depends on the backbone molecular weight Z_b (in terms of number of entanglements) and the volume fraction of the backbone Φ_b , but is also influenced by the number of dangling arms q and the relaxation time τ_a of the fraction x of one arm segments that is drawn into the backbone tube at a given time. It is therefore time-dependent. The arm relaxation time τ_a , eq. (4.3), is also time-dependent and changes with x . The stretch relaxation time τ_s of the backbone, eq. (4.1), has a fixed timescale and depends only on the molecular weight Z_b of the backbone and the longest arm relaxation time $\tau_a(0)$, while not being drawn into the backbone tube.

Using the multi-mode variation of the Pom-Pom model, suggested by Inkson et al. [92], the stress tensor is given by the following equation, where second rank tensors are represented by bold letters.

$$\boldsymbol{\sigma} = 3 \sum_i^N G_i \lambda_i^2(t) \mathbf{S}_i(t) \quad (4.4)$$

Where G_i are the elastic moduli and λ_i are the stretch ratios of the backbone. \mathbf{S} is the orientation tensor, which is given by the unit tensor, and \mathbf{K} is the velocity gradient.

$$\mathbf{S} = \frac{\mathbf{A}}{\text{tr} \mathbf{A}} \quad (4.5)$$

$$\frac{D\mathbf{A}}{Dt} = \mathbf{K} \cdot \mathbf{A} + \mathbf{A} \cdot \mathbf{K}^T - \frac{1}{\tau_b} (\mathbf{A} - \mathbf{I}) \quad (4.6)$$

4. Intrinsic Nonlinearity in Pom-Pom and MSF Constitutive Equations

An evolution of the originally proposed Pom-Pom model was given by Blackwell et al. [72] and McLeish et al. [99], which discusses a branch point displacement. The stretch relaxation time τ_s , and the backbone stretch itself, is reduced by an exponential factor. Consequently, the stretch equation is nonlinear in $\lambda(t)$.

$$\frac{D\lambda(t)}{Dt} = \lambda(t)\mathbf{K} : \mathbf{S} - \frac{1}{\tau_s}(\lambda(t) - 1)e^{\frac{2(\lambda(t)-1)}{q-1}} \quad \text{for } \lambda < q \quad (4.7)$$

A subsequent modification by Lee et al. [96] accounts for the reversing flow of entangled chains.

$$\frac{1}{\tau_b^*} = \frac{1}{\tau_b} + \frac{\dot{\lambda}}{\lambda} - \mathbf{K} : \mathbf{S} \quad \text{for } \lambda < 1 \quad (4.8)$$

This is especially important for the investigation of oscillatory shear, since a reversal of flow is applied repeatedly to the molecules.

4.1.2. Pom-Pom Model Predictions for Nonlinearity in MAOS

Hyun et al.[24] and Hoyle et al.[29] simulated the single mode Pom-Pom constitutive equation in the LAOS/MAOS regime within the framework of FT rheology analysis. In order to focus on molecular weight effects, a single mode Pom-Pom model is used [24]. The slowest mode in the relaxation spectrum $\{G_i, \tau_i\}$ is chosen for this, since it is the most dominant. This is the longest relaxation time τ_0 . The single mode Pom-Pom constitutive equation is given by the following equation, with G_N^0 being the plateau modulus.

$$\sigma = 3G_N^0 \Phi_b^2 \lambda^2(t) \mathbf{S}(t) \quad (4.9)$$

The volume fraction of the backbone Φ_b equals 1 for linear polymers. Simulation of the single mode Pom-Pom model in MAOS showed that the stress response

depends on the ratio of orientation time τ_b (respectively the longest relaxation time τ_0 for linear polymers), and the stretch relaxation time τ_s , of the backbone, which are proportional to the number of effective entanglements Z_b along the backbone.

$$r = \frac{\tau_b}{\tau_s} = \frac{4}{\pi^2} Z_b \quad (4.10)$$

Hoyle et al. [29] concluded that for $q > 1$, the predictions of $I_{3/1}(\gamma_0)$ in MAOS are more sensitive to changes in the ratio of relaxation times, $r = \tau_b/\tau_s$, than to changes in the degree of branching, q .

In this work, the main focus lies on the investigation of nonlinear behavior of linear polymer melts. The backbone orientation time τ_b is correlated to, and termed as the longest relaxation time τ_0 within the framework of linear, monodisperse polymers, to ensure a distinct and consistent nomenclature in the following remarks.

One method to predict the rheology of a linear molecule using the Pom-Pom constitutive model is to set the branching degree $q = 1$, and the stretch relaxation time to zero, $\tau_s = 0$, meaning $r \rightarrow \infty$. Another possible viewpoint is that a linear molecule could also exhibit chain stretch relaxation and therefore $\tau_s > 0$. With respect to the latter assumption $\tau_s > 0$, the ratio of relaxation times r in the limit of a linear polymer could be presented as [24]:

$$r = \frac{\tau_0}{\tau_s} = \frac{4}{\pi^2} \frac{M_w}{M_e} \approx 0.4Z \quad (4.11)$$

Where $Z = M_w/M_e$ is the number of entanglements of the linear molecule, and the volume ratio Φ_b of the backbone from eq. (4.10) approaches 1.

With respect to this criterion, the Pom-Pom model with a single relaxation time is used with Z as the only fitting parameter, to predict the rheological behavior

4. Intrinsic Nonlinearity in Pom-Pom and MSF Constitutive Equations

of linear polymer melts in the MAOS regime. Single mode models result in an approximation for monodisperse polymers. However, even linear monodisperse polymers show a relaxation time spectrum due to different relaxation mechanisms of the polymer chain (see also chapter 3.3). Nevertheless, a single mode version was used to gain an analytical solution for 3Q_0 in the MAOS region with an explicit formula as a function of molecular weight (respectively Z) and the Deborah number $De = \omega\tau_0$.

An asymptotical solution of the Pom-Pom differential equation at low strain amplitudes ($\gamma_0 \leq 1$) results in the intensity of the first and third harmonics of the stress response $\sigma(t)$ with the Deborah number De , and the number of entanglements Z in the following equations (see appendix B and [25] for detailed calculation).

$$\gamma(t) = \gamma_0 \sin(\omega t)$$

$$\sigma(t) = \sum_{n=odd} I'_n \sin(n\omega t) + I''_n \cos(n\omega t) \quad (4.12)$$

$$I'_1 = G_N^0 \left(\frac{De^2}{1 + De^2} \right) \gamma_0 \quad (4.13)$$

$$I''_1 = G_N^0 \left(\frac{De}{1 + De^2} \right) \gamma_0 \quad (4.14)$$

$$I'_3 = G_N^0 \left(\frac{De^4(1 - 2.5Z^{-1})(De^2 + 12.5De^2Z^{-1} - 2 - 2.5Z^{-1})}{\pi(1 + 25De^2Z^{-2})(1 + 4De^2)(1 + De^2)^2} \right) \gamma_0^3 \quad (4.15)$$

$$I''_3 = G_N^0 \left(\frac{De^3(1 - 2.5Z^{-1})(10De^4Z^{-1} - 5De^2 - 20De^2Z^{-1} + 1)}{2\pi(1 + 25De^2Z^{-2})(1 + 4De^2)(1 + De^2)^2} \right) \gamma_0^3 \quad (4.16)$$

Where G_N^0 is the rubber plateau modulus and I'_1 and I''_1 , are proportional to the storage and loss modulus, respectively. I'_3 and I''_3 are the real and imaginary parts of the absolute value of the intensity of third harmonics in the shear stress. With respect to the definition of ${}^3Q_0(\omega)$ (eq. 3.53) and eqs. (4.13) to (4.16), the intrinsic nonlinearity ${}^3Q_0(De)$ is calculated as follows, where $I_1 = \sqrt{I_1'^2 + I_1''^2}$ and $I_3 =$

$$\sqrt{I_3'^2 + I_3''^2}.$$

$${}^3Q_0(De) = \frac{De^2(1 - 2.5Z^{-1})}{2\pi(1 + 25De^2Z^{-2})^{0.5}(1 + 4De^2)^{0.5}(1 + De^2)^{0.5}} \quad \text{for } Z > 2.5 \quad (4.17)$$

Please note, that ${}^3Q_0(\omega)$ cannot be smaller than 0, and equation (4.17) is therefore limited to $Z > 2.5$. Detailed calculations of ${}^3Q_0(De)$ from the single mode Pom-Pom model are given in the appendix.

Figure 4.2 presents the normalized storage and loss modulus, G'/G_N^0 and G''/G_N^0 , calculated from eqs. (4.13) and (4.14), along with 3Q_0 vs De (eq. 4.17) for various number of entanglements ($Z = 5, 10, 40, 630$ and ∞).

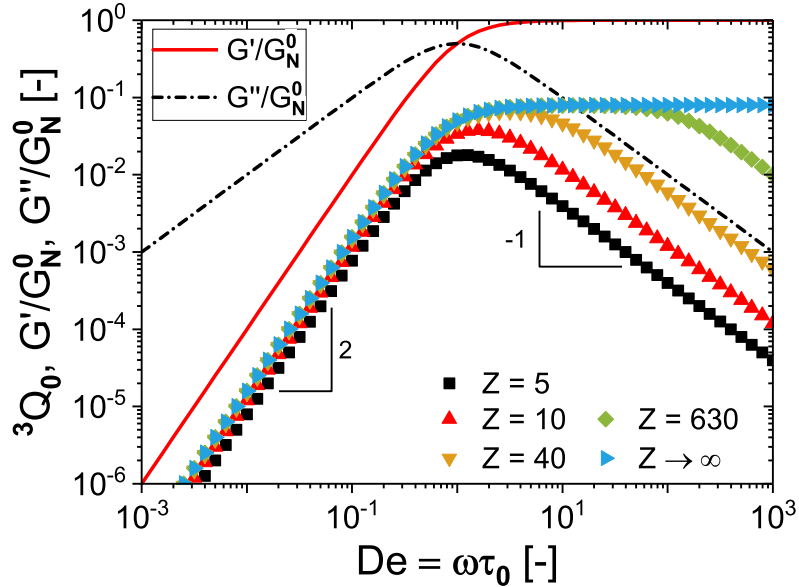


Figure 4.2.: Predictions of the single mode Pom-Pom model for the intrinsic nonlinearity ${}^3Q_0(De)$ along with predictions for normalized loss and storage modulus as a function of different entanglement numbers Z (modified from [76]).

It is shown that for low Deborah numbers, $De < 1$ ($De = 1$ is the crossover of G'/G_N^0 and G''/G_N^0) the intrinsic nonlinearity 3Q_0 scales to De^2 , where it behaves like the storage modulus G' . At high Deborah numbers, $De \gg 1$, 3Q_0 scales with De^{-1} , which is the same scaling as the loss modulus G'' . Figure 4.2 depicts that an increasing molecular weight results in a broader peak for 3Q_0 , utilizing the Pom-

4. Intrinsic Nonlinearity in Pom-Pom and MSF Constitutive Equations

Pom model. For polymers with $Z \leq 2.5$ the simplified Pom-Pom model predicts negative intensities (see eq. 4.17), that are clearly without physical meaning. An asymptotical simplification of eq. (4.17) for low and high Deborah numbers De results in the following equations.

$${}^3Q_0(De) = \frac{1}{2\pi} \frac{(1 - 2.5Z^{-1})De^2}{1} \quad \text{for } De \rightarrow 0 \quad (4.18a)$$

$${}^3Q_0(De) = \frac{1}{2\pi} \frac{(1 - 2.5Z^{-1})De^{-1}}{10Z^{-1}} \quad \text{for } De \rightarrow \infty \quad (4.18b)$$

Combination of eqs. (4.18a) and (4.18b) result in a simplified equation with the correct asymptotic limiting function.

$${}^3Q_0(De) = \frac{1}{2\pi} \frac{(1 - 2.5Z^{-1})De^2}{1 + 10Z^{-1}De^3} \quad \text{for } Z > 2.5 \quad (4.19)$$

This expression can be used as an approximation of ${}^3Q_0(De)$ for low and high Deborah numbers.

The prediction for the maximum value ${}^3Q_{0,max}$ of the intrinsic nonlinearity can be calculated from the derivative of eq. (4.19).

$${}^3Q_{0,max} = \frac{(1 - 2.5Z^{-1})(Z/5)^{2/3}}{6\pi} \quad (4.20)$$

$$\lim_{Z \rightarrow \infty} {}^3Q_{0,max} = \frac{1}{4\pi} \approx 0.08 \quad (4.21)$$

Detailed calculations for ${}^3Q_0(\omega)$ and ${}^3Q_{0,max}$ from the Pom-Pom model are given in the appendix B.

It is worth mentioning, that the simplified eq. (4.19) cannot predict ${}^3Q_{0,max}$ around $De \approx 1$ properly, as this equation is an approximation, optimized for low and high Deborah numbers. Figure 4.3 shows a comparison of ${}^3Q_0(De)$ with $Z = 10$ between the asymptotic equation (4.19) and the exact solution (eq. 4.17) as pre-

dicted from the single mode Pom-Pom model. The maximum deviation, referred to the exact equation, is given at $De = 1$ with almost 77%. For small (< 0.02) and high (> 50) Deborah numbers the deviation diminishes below 0.1% nevertheless.

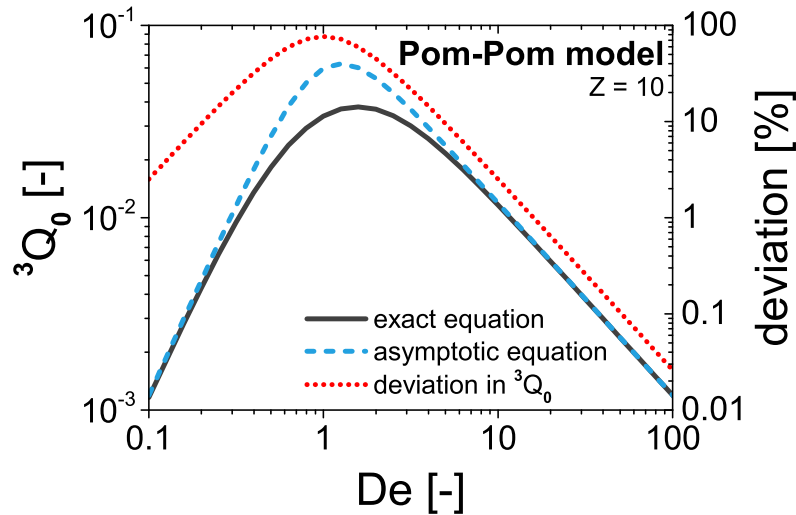


Figure 4.3.: Single mode Pom-Pom model predictions of ${}^3Q_0(De)$ for $Z = 10$ from the exact equation (4.17) and the simplified asymptotic equation (4.19). The maximum deviation between the exact and the simplified solution is given at $De = 1$, with almost 77% (adapted from [76]).

4.2. Molecular Stress Function (MSF) Model

4.2.1. Fundamentals

The molecular stress function (MSF) model is alike the Pom-Pom model (section 4.1) a molecular based constitutive model. It is based on the Doi-Edwards (DE) theory [78] and includes backbone stretching along with the sidechain orientation of comb-like molecules during deformation. It was developed by Wagner et al. [120–123] as a tube segment model, originating from a slip-link model [120]. In contrast to the original tube model of Doi and Edwards, the MSF model respects

4. Intrinsic Nonlinearity in Pom-Pom and MSF Constitutive Equations

a variable tube diameter $a(t)$ during deformation (fig. 4.4). At small deformations the tube diameter is inversely proportional to the average stretch of the tube [120]. The MSF model successfully predicted nonlinear phenomena, e.g. strain hardening in extensional flow and stress overshoot in transient shear flow, for linear [120, 121] and branched [121–123] polymers.

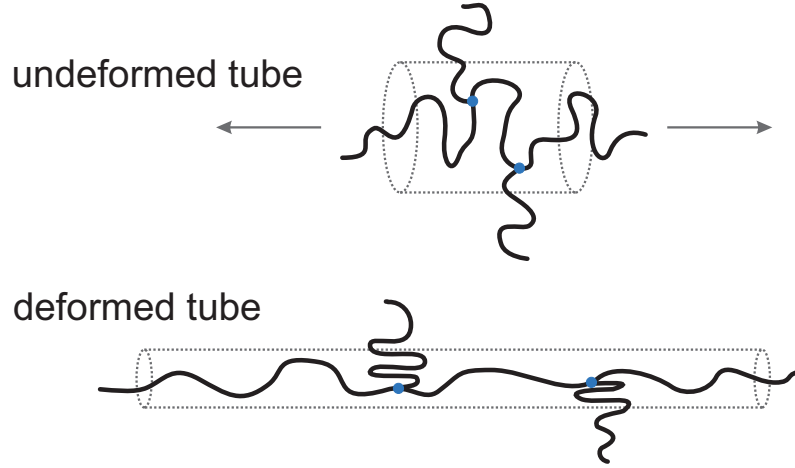


Figure 4.4.: Deformed and undeformed tube in theory of the MSF model. Adapted from Wagner et al. [122].

The extra stress tensor in the MSF model is given by the following equation.

$$\sigma(t) = \int_{-\infty}^t m(t-t') f^2(t, t') \mathbf{S}_{DE}^{IA}(t, t') dt' \quad (4.22)$$

Where $m(t-t')$ is the viscoelastic memory function, which can be obtained from the relaxation spectrum $\{G_i, \tau_i\}$ of linear rheological data.

$$m(t-t') = \frac{\delta G(t-t')}{\delta t'} = \sum_{i=1}^N \frac{G_i}{\tau_i} \exp\left(-\frac{t-t'}{\tau_i}\right) \quad (4.23)$$

The molecular stress function f is the relative tube diameter at equilibrium state (a_0) and after deformation (a).

$$f(t, t') = \frac{a_0}{a(t, t')} \quad (4.24)$$

4.2. Molecular Stress Function (MSF) Model

The time t' indicates the time when the tube segment was created with an equilibrium tube diameter, and t is the present time, when the stress is measured.

In a more recent work, Abbasi et al. [69] proposed an evolution equation for f with respect to long chain branching (LCB).

$$\frac{\delta f^2}{\delta t} = \beta f^2 \left((\mathbf{K} : \mathbf{S}) - \frac{CR}{f^2 - 1} \right) - (\beta - 1) \frac{\delta f_s^2}{\delta t} \quad (4.25a)$$

Where f and f_s represent the backbone and sidechain stretching, respectively. Abbasi et al. [25] concluded in a further work, that for $f_s \ll f$, i.e. short arms, the sidechain stretch equals 1, $f_s = 1$, and therefore eq. (4.25a) can be reduced .

$$\frac{\delta f^2}{\delta t} = \beta f^2 \left((\mathbf{K} : \mathbf{S}) - \frac{CR}{f^2 - 1} \right) \quad (4.25b)$$

This equation respects constraint release (CR) due to motion of the surrounding polymer matrix.

$$CR = \frac{(f^2 - 1)^2}{f_{max}^2 - 1} \sqrt{\mathbf{D}^2 : \mathbf{S}} + a_2 (f^2 - 1)^2 \sqrt{|\mathbf{W}\mathbf{D} : \mathbf{S}|} \quad (4.26)$$

The parameter β is associated with the isotopic stretch of the polymer chains (ratio of number of all entanglements to number of entanglements of the backbone, $\beta = M_w/M_b$), and was shown to be sensitive to the topology of the molecule. It is also connected to the rate of strain hardening in extensional flow. Parameter a_2 is related to the overshoot in transient shear flows, and f_{max} predicts the maximum (steady-state) viscosity. Correlation of molecular structure to the nonlinear parameters f_{max} , β and a_2 is presented in [32].

\mathbf{S}_{DE}^{IA} is the strain measure of the Doi-Edwards (DE) model, using the independent alignment (IA) assumption [124], and was approximated by Curries's formula

[75].

$$\mathbf{S}_{DE}^{IA}(t, t') = 5\mathbf{S} = 5 \left[\left(\frac{1}{J-1} \right) \mathbf{B} - \left(\frac{1}{(J-1)(I_2 + 13/4)^{0.5}} \right) \mathbf{C} \right] \quad (4.27)$$

$$\text{with } J = I_1 + 2\sqrt{I_2 + 13/4} \quad (4.28)$$

\mathbf{C} and \mathbf{B} are the Cauchy and Finger tensors, respectively, I_1 is the trace of \mathbf{B} , and I_2 is the trace of \mathbf{C} . Please note, that in this context, I_1 and I_2 may not be mistaken for the higher harmonic intensities from chapter 3.

4.2.2. MSF Model Predictions for Nonlinearity in MAOS

The MSF model was extended to predict the nonlinear behavior of linear and long chain branched molecules (e.g. strain hardening in extensional flows) in different nonlinear deformations with a maximum of three nonlinear parameters β , f_{max} and a_2 (see eq. 4.25a and 4.26) [32]. Wagner et al. [26] used the MSF model to predict ${}^3Q_0(\omega)$ data of entangled linear and model comb polystyrenes, which before had been experimentally provided by Hyun and Wilhelm [23] in the framework of FT rheology. The strain measure \mathbf{S} for small deformations from eq. (4.27) could be expressed in a general form as a function of a series of odd strain powers.

$$\mathbf{S} = \gamma - (\alpha - \beta)\gamma^3 + O(\gamma^5) \quad (4.29)$$

They concluded that ${}^3Q_0(\omega)$ is proportional to the difference of the orientational effect α and the stretching effect β , whereas f_{max} (maximum tension in a chain segment, governs the steady state extensional viscosity) and a_2 (governs the overshoot in transient shear viscosity) had no distinct effect on ${}^3Q_0(\omega)$. The consideration of the DE model for linear polymers with the independent alignment assumption (DE-IA) resulted in a constant $\alpha = 5/21$. The stretching effect

4.2. Molecular Stress Function (MSF) Model

β was used as a fitting parameter for polymer combs by Wagner et al. [26], whereas $\beta_W = 0.12$ resulted for linear polystyrenes (see below, as notation was later modified by Abbasi et al. [25]).

Abbasi et al. [25] extended this idea and presented an evolution equation to predict the extensional, transient shear and MAOS behavior simultaneously with a single set of nonlinear material parameters. In this evolution equation, the parameter β is changed by its numerical value and represents the ratio of number of entanglements in the whole molecule to the number of entanglements in the backbone, and controls the rate of strain hardening in extensional flow. Based on this definition, β is equal to 1 for a linear polymer and increases monotonically with increasing long chain branching content. In the final evolution equation, $\beta_W = 0.12$ from Wagner et al. [26] was replaced with $\beta_A/10 = 0.1$ by Abbasi et al. [25], to gain a consistency between the predicted β for linear polymer topologies and the fitting of the model on the extensional viscosity, and 3Q_0 in MAOS deformation. Within this thesis, from now on, the definition of Abbasi et al. $\beta = \beta_A$ will be used, where a non-branched polymer has $\beta = 1$ per definition.

An asymptotical solution of the single mode MSF model for linear polymers in MAOS results, in analogy to the single mode Pom-Pom model (eq. 4.12 to 4.16), in the intensity of first and third harmonics as a function of Deborah number, $De = \omega\tau_0$, and of the difference of the orientation and stretch parameters $(\alpha - \beta/10)$.

$$I'_1 = G_N^0 \left(\frac{De^2}{1 + De^2} \right) \gamma_0 \quad (4.30)$$

$$I''_1 = G_N^0 \left(\frac{De}{1 + De^2} \right) \gamma_0 \quad (4.31)$$

$$I'_3 = G_N^0 \frac{3}{4} (\alpha - \beta/10) \left(\frac{De^2}{1 + De^2} - \frac{4De^2}{1 + 4De^2} + \frac{3De^2}{1 + 9De^2} \right) \gamma_0^3 \quad (4.32)$$

$$I''_3 = G_N^0 \frac{3}{4} (\alpha - \beta/10) \left(\frac{De}{1 + De^2} - \frac{2De}{1 + 4De^2} + \frac{De}{1 + 9De^2} \right) \gamma_0^3 \quad (4.33)$$

4. Intrinsic Nonlinearity in Pom-Pom and MSF Constitutive Equations

With respect to the definition of the intrinsic nonlinearity ${}^3Q_0(De)$ (eq. 3.53) and eqs. (4.30) to (4.33), ${}^3Q_0(De)$ is calculated for the single mode MSF model (for detailed calculation see *Appendix*):

$${}^3Q_0(De) = \frac{3}{2}(\alpha - \beta/10) \frac{De^2}{(1 + 9De^2)^{0.5}(1 + 4De^2)^{0.5}} \quad (4.34)$$

An asymptotical simplification of eq. (4.34) for low and high De , in analogy to equations (4.18a) and (4.18b), results in:

$${}^3Q_0(De) = \frac{3}{2}(\alpha - \beta/10) \frac{De^2}{1 + 6De^2} \quad (4.35)$$

Figure 4.5 shows predictions for ${}^3Q_0(\omega)$ for a linear ($\beta = 1$) and a slightly branched polymer ($\beta = 1.75$). The single mode MSF model predicts a scaling of 2 for

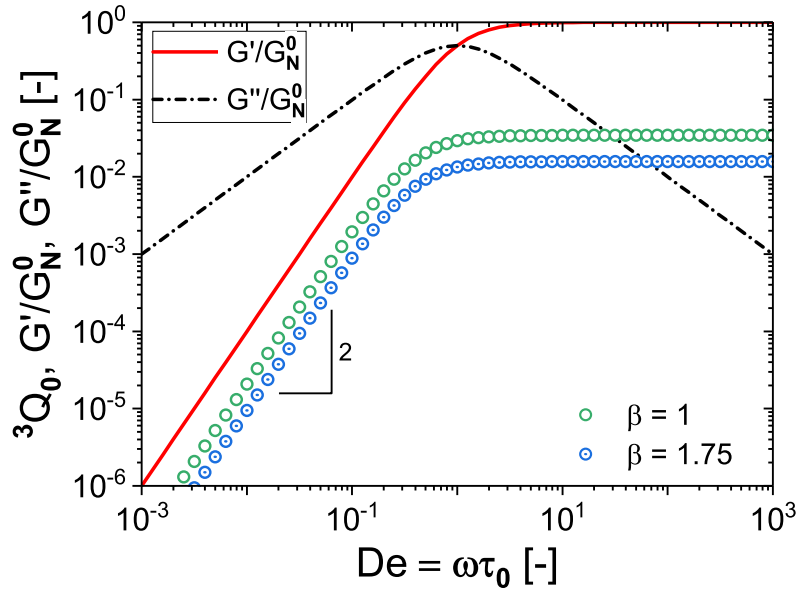


Figure 4.5.: Single mode MSF model predictions of ${}^3Q_0(De)$ for $\beta = 1$ (linear polymer) and $\beta = 1.75$ (slightly branched) from eq. (4.34).

small frequencies, ${}^3Q_0(\omega) \propto De^2$. This agrees with the behavior of the storage modulus G' in the flow regime. Around $De = 1$, a constant value for ${}^3Q_0(\omega)$ is

reached, which is maintained for higher frequencies as well.

$${}^3Q_{0,max} = \lim_{De \rightarrow \infty} {}^3Q_0(\omega) = \frac{1}{4}(\alpha - \beta/10) \quad (4.36)$$

An increasing parameter β for more branched polymers, decreases the maximum plateau value of ${}^3Q_{0,max}$, linearly (fig. 4.5).

Using $\alpha = 5/21$ and $\beta = 1.0$ for a linear polymer topology, eq. (4.35) will be simplified even further (for detailed calculation see appendix B).

$${}^3Q_0(De) = 0.207 \frac{De^2}{1 + 6De^2} \quad (4.37)$$

$${}^3Q_{0,max} = \lim_{De \rightarrow \infty} {}^3Q_0(De) = 0.0345 \quad (4.38)$$

The deviation between eq. (4.37) compared to the exact equation (4.34) is at maximum, at around $De = 0.4$, below 2% (fig. 4.6).

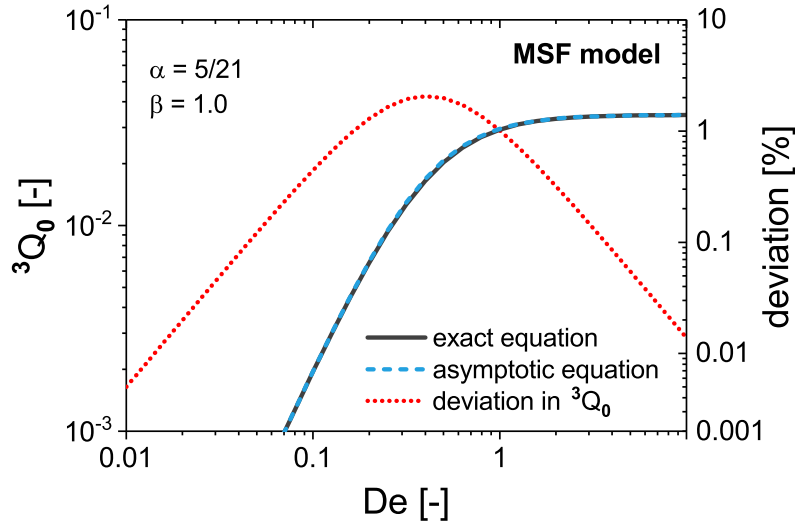


Figure 4.6.: Single mode MSF model predictions for ${}^3Q_0(\omega)$ from the exact eq. (4.34) and the asymptotic simplification eq. (4.35) for linear polymers ($\beta = 1$). The maximum deviation between both solutions is 2% at maximum (normalized to the exact equation).

4.3. General Prediction for Nonlinear Behavior from Constitutive Models

Equations (4.13) and (4.14) in the Pom-Pom model and eqs. (4.30) and (4.31) in the MSF model show, that these models predict similar Maxwell behavior for the loss and storage modulus at low enough strain amplitudes. Figure 4.7 compares eq. (4.34) from the MSF model (with constant parameter $\alpha = 5/21$ and two different $\beta = 1.0$ and 1.75) with Pom-Pom model predictions (eq. 4.17). The MSF model predictions, as well as the Pom-Pom model, scale with De^2 at low frequencies. After the crossover point of the normalized loss and storage modulus, the MSF predictions level off at a plateau value of ${}^3Q_{0,max} = 0.25(\alpha - \beta/10)$, where for a linear polymer ${}^3Q_{0,max} \approx 0.03$, for $\alpha = 5/21$ and $\beta = 1$. This leveling off at high frequencies is similar to the predictions of the Pom-Pom model (${}^3Q_{0,max} = 1/4\pi \approx 0.08$) with infinitive number of entanglements ($Z \rightarrow \infty$, see eq. 4.21). However, the MSF model predicts the same value ${}^3Q_{0,max}$ for all linear polymers, and has no parameter to adapt for varying molecular weights.

A comparison between equations (4.19) and (4.37), as well as in view of figure 4.7, it can be assumed that a general equation could predict the intrinsic nonlinearity ${}^3Q_0(De)$ at low and high De as with three fitting parameters.

$${}^3Q_0(De) = a \frac{De^2}{1 + b \cdot De^{2+k}} \quad (4.39)$$

Here a , b and k are the material characteristics, that might depend on the monomer type, molecular weight, and/or polydispersity.

For the Pom-Pom model, a and b show a dependence on the entanglement number Z , $a = 1/(2\pi)(1 - 2.5Z^{-1})$ and $b = 10Z^{-1}$. In the MSF model, a and b are

4.3. General Prediction for Nonlinear Behavior from Constitutive Models

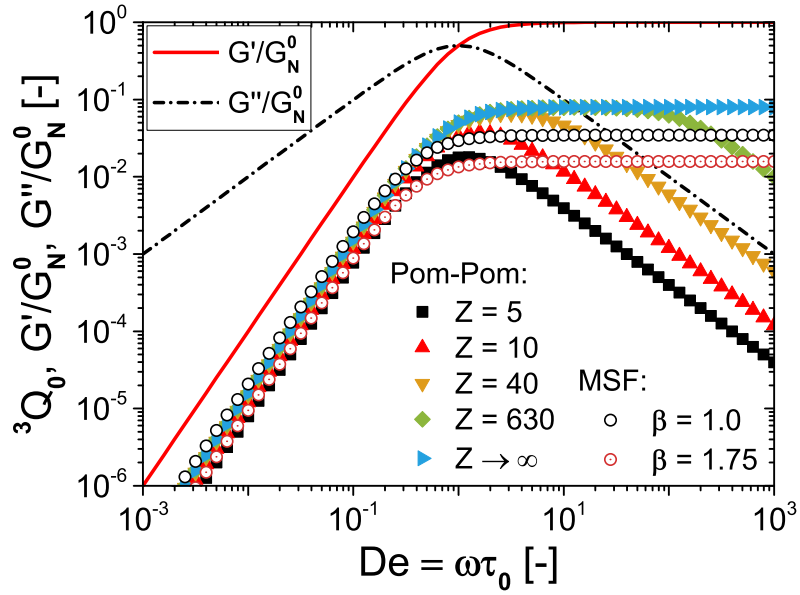


Figure 4.7.: Predictions of the Pom-Pom and MSF model for ${}^3Q_0(\omega)$ in comparison (adapted from [76]). For small frequencies, both models predict similar nonlinear behavior for monodisperse polymers (${}^3Q_0(\omega) \propto De^2$).

constants instead, $a = 1.5(\alpha - \beta/10)$ and $b = 6$, with $\alpha = 5/21$ and $\beta = 1$. In other words, for a linear polymer, the MSF model predicts ${}^3Q_0(De)$ as a function only of the longest relaxation time τ_0 . This longest relaxation time τ_0 can be predicted by polymer reptation theories ($\tau_0 \propto M^{3.4}$) or by direct measurements of loss and storage modulus data [6].

$$\lim_{\omega \rightarrow 0} \left(\frac{G''}{\omega} \right) = \sum_i G_i \tau_i \quad (4.40)$$

$$\lim_{\omega \rightarrow 0} \left(\frac{G'}{G''^2} \right) = \sum_i \frac{G_i \tau_i^2}{(G_i \tau_i)^2} \quad (4.41)$$

$$\lim_{\omega \rightarrow 0} \left(\frac{G''}{\omega} \cdot \frac{G'}{G''^2} \right) = \lim_{\omega \rightarrow 0} \left(\frac{G'}{\omega G''} \right) = \tau_0 \quad (4.42)$$

In contrast to the MSF model, ${}^3Q_0(De)$ depends not only on the longest relaxation time τ_0 in the Pom-Pom model, but also on the molecular weight M_w .

5. Rheological Experiments

5.1. Methodology

All rheological characterizations were conducted with an ARES G2 strain controlled rotational rheometer from TA instruments. Parallel plate geometries (13 mm and 25 mm diameter) were used to measure the linear behavior. Nonlinear oscillatory shear (MAOS) tests were partly conducted with cone-plate geometries (13 mm and 25 mm diameter, both with 0.1 rad cone angle) to maintain a homogeneous shear field, partly with a self-made 10 mm partitioned plate geometry in combination with a 13 mm, 0.1 rad cone geometry. The partitioned plate setup was chosen to obtain high shear rates without edge fracture affecting the measurement [113]. However, the partitioned plate-cone (ppc) setup was not optimal for all samples and measurement temperatures, since percolation of the sample into the split between geometry and surrounding plate occurred. The small diameter of 10 mm, and a resulting low torque also lead to sensitivity issues, especially for low entangled polymers. Therefore, if not stated otherwise, the here presented results were measured with a simple plate-plate (SOAS) or cone-plate (MAOS) geometry.

The ARES G2 rheometer, used in this work, is provided with the TA Instruments TRIOS software, which is capable of directly calculating $I_{3/1}$ from raw stress time

5. Rheological Experiments

data (correlation mode). The nonlinear master curves were then created from 3Q_0 values with the TTS principle, utilizing WLF parameters from corresponding linear master curves. Reinheimer et al. [127] rated the reliability of the TRIOS software correlation mode, compared to raw time data measurements, as most accurate for nonlinear experiments. Nevertheless, raw stress time data was recorded additionally in the transient mode and Fourier transformed with a home-written MATLAB routine, to gain access to the frequency spectra of stress and normal force.

Most of the presented results of linear homopolymer melts in this chapter were published in Cziep et al. [76].

5.2. Linear homopolymer Melts

All polymer samples have been specifically synthesized with anionic polymerization (see chapter 2), free radical polymerization or emulsion polymerization, with the exception of high density polyethylene (HDPE), which was donated and characterized (M_w , M_n , PDI) by LyondellBasell, and poly(ethylene oxide) (PEO), which was kindly donated and characterized by Polymer Standards Service GmbH (PSS). Table 5.1 lists the investigated samples.

5.2.1. Small Amplitude Oscillatory Shear (SAOS) Experiments

Oscillatory shear experiments were conducted in the linear regime for all polymer melts in this work. The linear viscoelastic region of each sample was determined with strain sweep experiments under oscillatory shear. Linear master curves of $G'(\omega)$ and $G''(\omega)$ have been acquired via the TTS principle [27] (see also

sample*	M_w [g/mol]	M_n [g/mol]	PDI	Z (M_w/M_e)**	Polymerization method
PS 25k	24 600	23 700	1.03	1.5	anionic
PS 43k	43 000	41 800	1.03	2.6	anionic
PS 83k	83 400	81 100	1.03	5.0	anionic
PS 154k	154 300	146 100	1.06	9.2	anionic
PS 340k	340 100	294 500	1.15	20.2	anionic
PS 107k	106 700	53 600	2.00	6.4	free radical
PS 112k	112 200	67 500	1.66	6.7	free radical
PS 186k	186 400	79 900	2.33	11.0	emulsion
PS 602k	602 000	127 400	4.70	35.5	emulsion
PI 22k	22 300	21 600	1.04	4.5	anionic
PI 42k	42 500	41 100	1.03	8.6	anionic
PI 87k	86 800	84 300	1.03	17.6	anionic
PpMS 32k	31 900	30 500	1.04	1.4	anionic
PpMS 210k	210 100	199 700	1.05	9.3	anionic
P2VP 83k	82 900	71 500	1.16	3.4	anionic
PMMA 89k	89 400	85 400	1.05	16.7	anionic
PEO 220k	220 000	197 000	1.11	110	anionic***
PEO 1020k	1 020 000	884 000	1.15	510	anionic***
HDPE 155k	155 000	10 300	15.0	187	***
HDPE 338k	338 400	12 500	27.2	409	***

* sample nomenclature comprises polymer abbreviation (e.g. PS for polystyrene) and rounded weight average molecular weight M_w (e.g. 25k \equiv 24 900 g/mol)

** entanglement molecular weights of referred polymers in kg/mol: (PS) 16.8, (PI) 4.6, (PpMS) 22.5, (P2VP) 24.3, (PMMA) 5.4, (PEO) 2.0, (HDPE) 0.8

*** PEO provided by PSS; HDPE provided by LyondellBasell

Table 5.1.: Linear homopolymer melt samples, used in this thesis. The table lists molecular weights and PDIs as obtained by SEC.

5. Rheological Experiments

tab. 5.1 and section 3.2.1). The purpose of SAOS measurements was to attain information about material specific dynamics in the linear regime, such as the discrete relaxation spectrum $\{G_i, \tau_i\}$, including the longest relaxation time τ_0 , the modulus crossover frequency where, $\omega_1 \tau_{co} = 1$, and the plateau modulus G_N^0 as another important property. The obtained WLF parameters C_1 and C_2 (tab. 5.2) were used in the creation of nonlinear master curves of the intrinsic nonlinearity ${}^3Q_0(\omega)$ for each respective sample (see following section 5.3). Features from linear viscoelastic data were also compared directly to nonlinear measurements, to help determine correlations between nonlinear mechanical behavior and molecular properties.

The longest relaxation time τ_0 can be predicted by polymer reptation theories ($\tau_0 \propto M^{3.4}$) or by direct measurements of loss and storage modulus data, respectively the zero-shear viscosity η_0 and steady-state compliance J_0^e [6].

$$\eta_0 = \lim_{\omega \rightarrow 0} \left(\frac{G''}{\omega} \right) = \sum_i G_i \tau_i \quad (5.1)$$

$$J_0^e = \lim_{\omega \rightarrow 0} \left(\frac{G'}{G''^2} \right) = \sum_i \frac{G_i \tau_i^2}{(G_i \tau_i)^2} \quad (5.2)$$

$$\tau_0 = \eta_0 J_0^e = \lim_{\omega \rightarrow 0} \left(\frac{G''}{\omega} \cdot \frac{G'}{G''^2} \right) = \lim_{\omega \rightarrow 0} \left(\frac{G'}{\omega G''} \right) \quad (5.3)$$

Discrete relaxation spectra $\{G_i, \tau_i\}$ from the same linear oscillatory shear data were used for predictions from the Pom-Pom and MSF constitutive models (see section 4). It was possible to calculate the entanglement molecular weight M_e from the plateau value G_N^0 of the storage modulus $G'(\omega)$ for most of the here presented polymers, using the definition of equation (3.29) from Graessley and Fetters [85, 88].

The storage modulus $G'(\omega)$ of monodisperse samples showed a plateau modulus G_N^0 in the rubber plateau region, while for samples with a PDI ≥ 1.2 only a

shoulder could be examined (see fig. 3.9 in section 3.2.3). For all monodisperse polymers, the expected proportionality of $G' \propto \omega^2$ and $G'' \propto \omega^1$ were reached at low frequencies. The plateau value G_N^0 was determined by the minimum of $\tan \delta = G''/G'$ in the rubber plateau region [130]. From this plateau value G_N^0 , the entanglement molecular weight M_e was calculated with equation (3.29). For samples synthesized from the same monomer, M_e was taken from the sample with the highest molecular weight and a $PDI \leq 1.2$. Where possible, self measured values for M_e were used in this work to calculate the average number of entanglements $Z = M_w/M_e$. The exact values for M_e may therefore differ slightly from literature values. However, values from literature [85] were used for HDPE and PEO, that did not allow to determine M_e with the mentioned method.

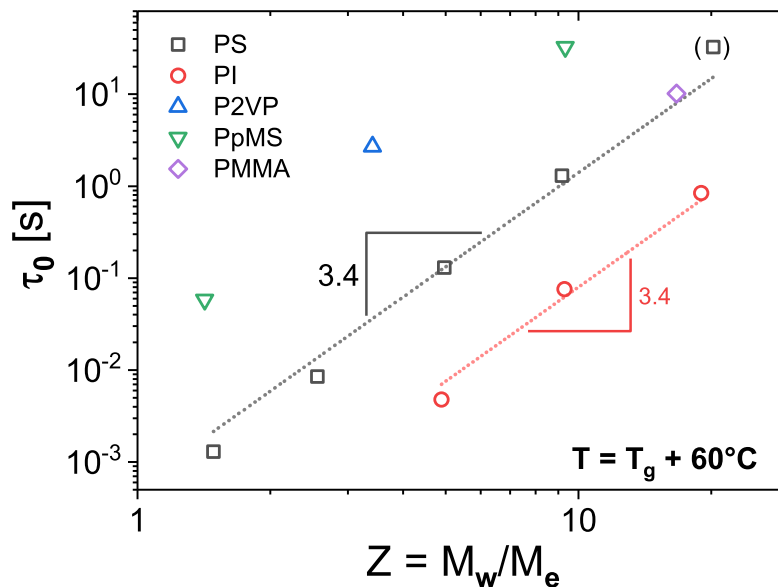


Figure 5.1.: Longest relaxation time $\tau_0(Z)$ for linear monodisperse homopolymers. Dotted lines show the expected scaling with molecular weight with $\tau_0 \propto M_w^{3.4}$ for polystyrene (PS) and polyisoprene (PI).

The longest relaxation times τ_0 , calculated with eq. (5.3) for monodisperse samples are presented in figure 5.1. The expected scaling of $\tau_0 \propto M_w^{3.4}$ was achieved, which approves the obtained data for further investigation in the nonlinear regime.

5. Rheological Experiments

sample	T_{ref} [°C]	C_1	C_2 [K]	G_N^0 [kPa]	T_g [°C]	τ_0^a [s]
PS 25k	160	7.455	131.4	287.7	103.6	0.0013
PS 43k	160	5.396	98.8	217.1	105.4	0.0085
PS 83k	160	6.087	104.6	178.8	105.5	0.13
PS 154k	160	6.153	104.7	153.0	107.8	1.3
PS 340k	160	6.199	104.8	169.2	106.7	33
PS 112k	160	6.149	105.5	166.0	105.7	na
PS 107k	160	6.044	104.4	140.0	106.0	na
PS 186k	160	6.146	103.6	135.2	106.3	na
PS 602k	160	5.853	103.6	167.6	106.7	na
PI 22k	-10	6.245	104.3	339.1	-65.0	0.0048
PI 42k	-10	6.651	106.6	335.6	-61.5	0.066
PI 87k	-10	6.370	104.7	357.7	-58.2	0.84
PpMS 31k	160	5.374	84.2	156.6	90.6	0.058
PpMS 210k	160	6.770	96.8	129.9	113.5	33
P2VP 83k	160	6.828	121.4	135.0	86.5	2.7
PMMA 89k	160	10.782	140.4	605.0	125.6	10
PEO 220k	80	2.469	203.2	na	na	0.25
PEO 1020k	80	1.206	91.5	na	na	na
HDPE 155k	140	2.246	212.4	na	133.9 ^b	na
HDPE 338k	140	2.835	270.9	na	130.3 ^b	na

^a relaxation times are listed for $T_g + 60^\circ\text{C}$ with exception of PEO 220k, which is given for $T = 80^\circ\text{C}$

^b no T_g was measured for HDPE, instead the melt temperature T_m is listed

Table 5.2.: Obtained material and rheometry properties from linear viscoelastic shear experiments of linear homopolymers, presented in this work. The list is completed by the glass transition temperature T_g for each sample, obtained by DSC. Except for the PEO and HDPE samples, all polymers were synthesized within this thesis. For further material characterization, see table 5.1.

5.3. Medium Amplitude Oscillatory Shear (MAOS) Experiments

Nonlinear mechanical data was obtained for all samples by Fourier Transformation of measured stress time data in medium amplitude oscillatory shear (MAOS). The used step by step method to obtain nonlinear master curves of ${}^3Q_0(\omega)$ is described in section 3.4.4.

The obtained ${}^3Q_0(\omega)$ values yielded nonlinear master curves for each polymer sample, when the WLF parameter from corresponding linear master curves were used (for more parameters see Tab. 5.2). The linear and nonlinear master curve of polystyrene sample PS83k, with $M_w = 83$ kg/mol, a PDI of 1.03 and $Z = 5$ is shown as an example in figure 5.2. The nonlinear mastercurve of ${}^3Q_0(\omega)$ was measured at three different measurement temperatures and and constructed, using the TTS principle with WLF parameters that were obtained from the respective linear master curve of the storage and loss modulus, $G'(\omega)$ and $G''(\omega)$. This example also contains two different data processing routines for ${}^3Q_0(\omega)$, the correlation and transient mode of the used TA ARES-G2 rheometer software (see section 5.1). Especially for lower frequencies below the modulus crossover frequency, and around the crossover, reproducibility of ${}^3Q_0(\omega)$ from both methods was achieved with an average deviation of less than 10 %.

Experience showed that measurement frequencies between $\omega_1 = 1$ rad/s and 10 rad/s constituted the "best" data in a reasonable time. The meaning of this assessment is discussed in the following description of a typical measurement routine for nonlinear mastercurves ${}^3Q_0(\omega)$.

A typical measuring routine for nonlinear mastercurves started at a certain temperature with a fresh sample and a first strain sweep test at a low frequency (usu-

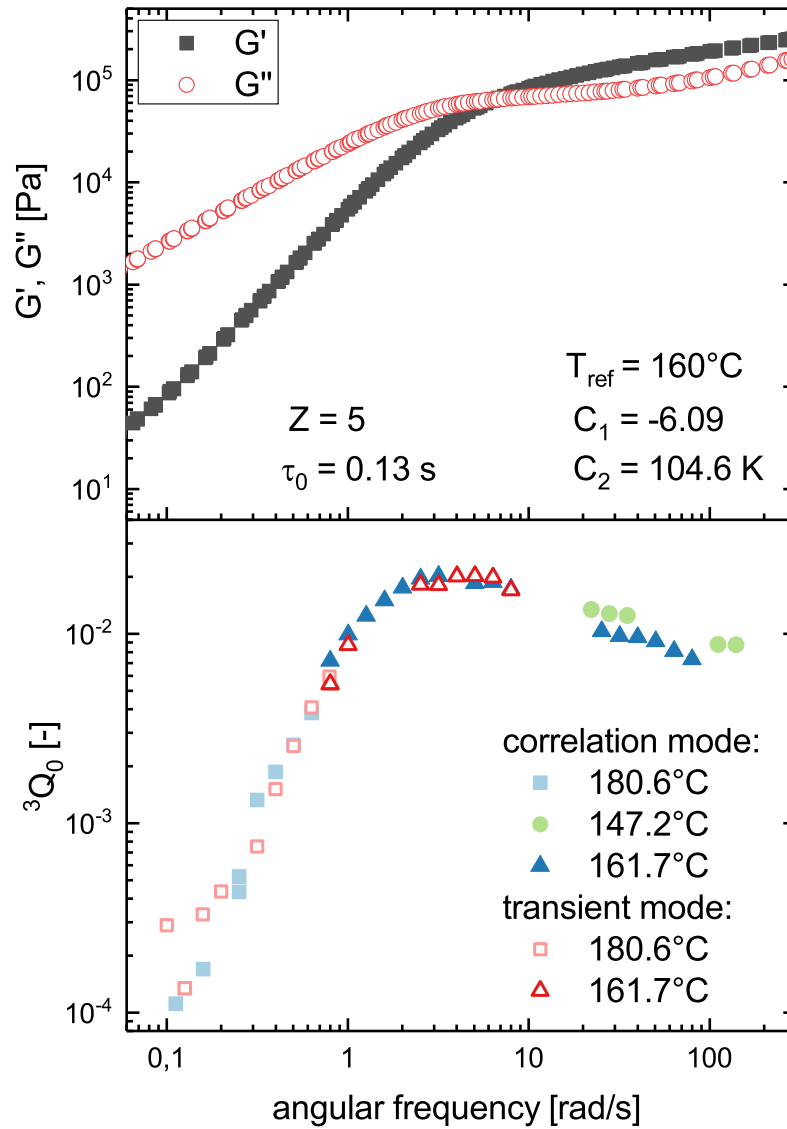


Figure 5.2.: Linear (top) and nonlinear (bottom) mastercurve of monodisperse polystyrene (PS83k). The nonlinear mastercurve was constructed by applying the given WLF shift parameter to the measured ${}^3Q_0(\omega)$ values from different measurement temperatures. Results for ${}^3Q_0(\omega)$ from correlation and transient mode of the rheometer software are shown (also see fig. 3.20).

5.3. Medium Amplitude Oscillatory Shear (MAOS) Experiments

ally 1 rad/s). The test ended with a high frequency at the same temperature and with the same sample, at which a scaling of 2 ($I_{3/1} \propto \gamma_0^2$) was no longer observed. Reasons for the non-quadratic scaling could be sample failure, for example due to edge fracture. The experiment could also not be continued, when the torque was too high for the instrument. Longer waiting times (up to 20 min) between two measurements, improved our data with regard to the observation of the expected scaling of $I_{3/1} \propto \gamma_0^2$. Samples had to be fully relaxed before the next measurement, else a scaling exponent smaller than 2 was found (typically $I_{3/1} \propto \gamma_0^{1.4-1.7}$). Reproducibility of the nonlinear master curves was given in our experiments, with a typical standard deviation for ${}^3Q_0(\omega)$ values of estimated 4% for low frequencies, and up to 15% for higher frequencies. Appearing scattering of ${}^3Q_0(\omega)$ values at higher frequencies after the observed local maximum, ${}^3Q_{0,max}$, occurred because of experimental difficulties. These intricacies originated from low measurement temperatures close to the glass transition temperature T_g of the polymer melts, or high measurement frequencies, which led to possible wall slip and other sample failures, torque overload or low S/N of the higher harmonics, i.e. I_3 .

Nonlinear Master Curves of Chemically Different, Linear Monodisperse Polymers

Nonlinear master curves of linear homopolymers with a low PDI ≤ 1.08 were examined with respect to molecular weight and monomer. Investigated linear, monodisperse homopolymers in this study were polystyrene (PS), poly(methyl methacrylate) (PMMA), *cis*-1,4-polyisoprene (PI), poly-*p*-methylstyrene (PpMS), poly(2-vinylpyridine) (P2VP), poly(ethylene oxide) (PEO), and polydisperse high-density polyethylene (HDPE). For detailed sample properties see Tab. 5.1. In the measured frequency range, the nonlinear master curves of samples with a low PDI showed a scaling at $\lim_{\omega \rightarrow 0} {}^3Q_0(\omega) \propto \omega^n$ with typically $n = 2 \pm 0.4$ ($n = 2$

5. Rheological Experiments

expected from Eq. 4.39) and scaling exponents k between 0.06 and 0.49 for higher frequencies, $\lim_{\omega \rightarrow \infty} {}^3Q_0(\omega) \propto \omega^{-k}$, after reaching the maximum ${}^3Q_{0,max}$ (Fig. 5.3; see also Eq. 4.39). The large variety of different scaling exponents for ${}^3Q_0(\omega)$ at

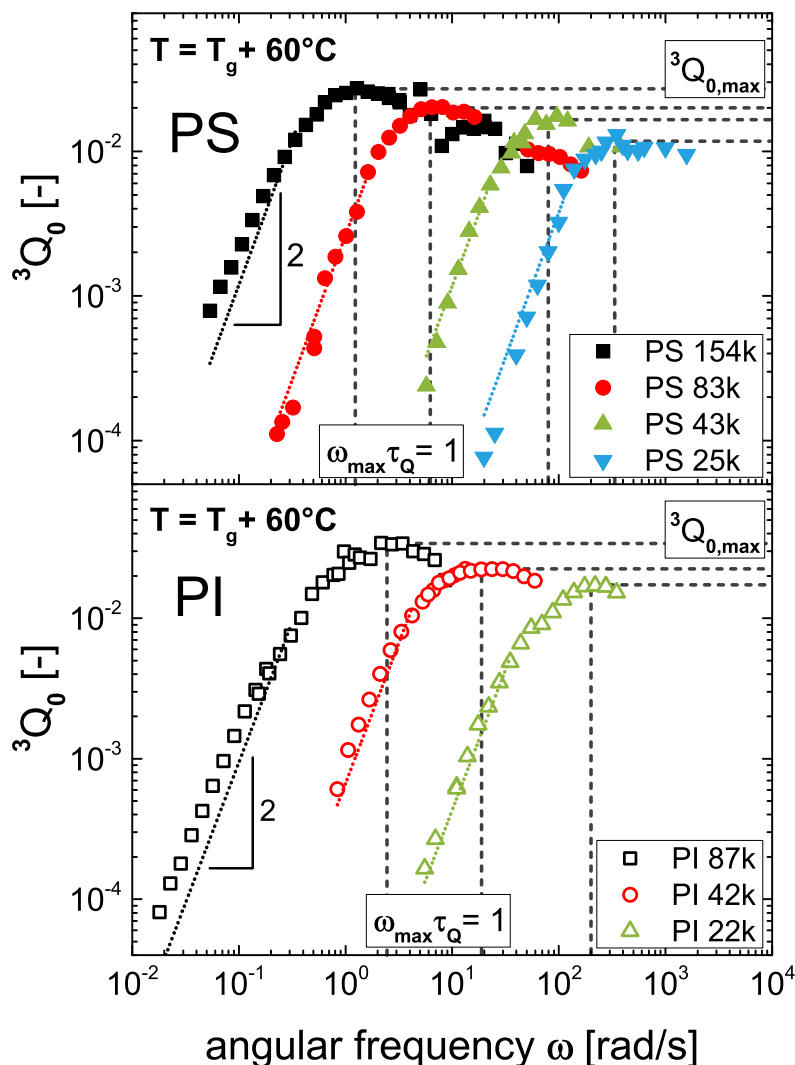


Figure 5.3.: Nonlinear master curves of low PDI polystyrene (PS) and *cis*-1,4-polyisoprene (PI) samples. For low frequencies approximately ${}^3Q_0(\omega) \propto \omega^2$ was found for all monodisperse polymer melts (dotted lines). Adapted from Cziep et al. [76].

higher frequencies is based on the experimental problems described in section 3.4.4 (e.g. edge fracture), so that only few measurement points could be acquired in this region. However, high frequency ${}^3Q_0(\omega)$ data could be obtained for a couple of polymer melt samples (PS 154k, PS 83k and PpMS 210k). These measu-

periments resulted a scaling exponent k between 0.30 and 0.37.

A characteristic feature in the experimental data of all nonlinear master curves of monodisperse, linear homopolymer melts is the maximum ${}^3Q_{0,max}$. Set expectations from constitutive modeling are either a dependence on the entanglement number Z (Pom-Pom), or a constant value (MSF). The experiment reveals a correlation to Z , however neither of the constitutive models presented in chapter 4 (Pom-Pom and MSF model) could predict the found scaling of approximately ${}^3Q_{0,max} \propto Z^{0.35}$ (fig. 5.4.

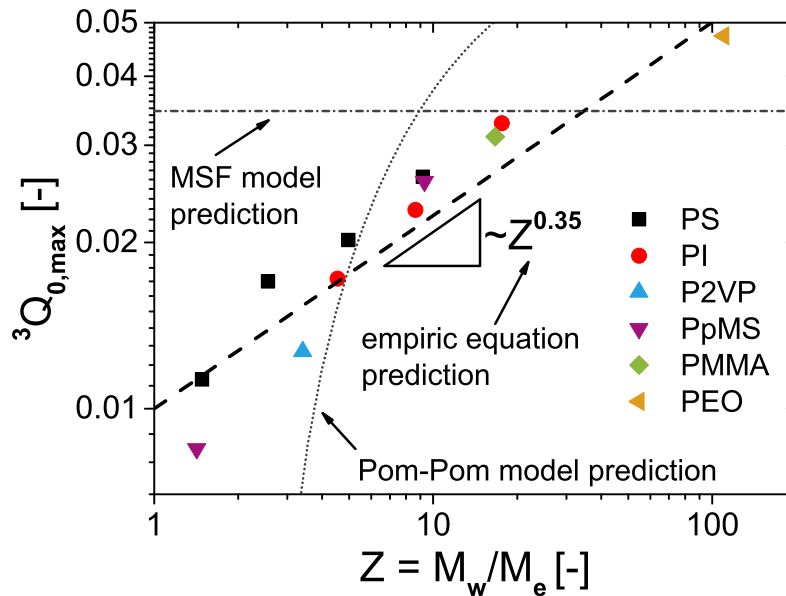


Figure 5.4.: Experimentally determined nonlinear master curve maxima ${}^3Q_{0,max}$ of monodisperse, linear homopolymer melts presented in this thesis (also see fig. 5.6). ${}^3Q_{0,max}$ scales with the entanglement number ($\propto Z^{0.35}$). Predictions from the simplified Pom-Pom (eq. 4.19) and MSF models (eq. 4.35), as well as expectations from the anticipated empiric equation (eq. 5.5) are shown.

The nonlinear relaxation time τ_Q is calculated via $\tau_Q \omega_{max} = 1$ at the maximum ${}^3Q_{0,max}$ and is, within experimental limits, similar to the longest linear relaxation time τ_0 (fig. 5.5), which is obtained from respective linear master curves (eq. 5.3). The found correlation of $\tau_Q = \tau_0^{0.9}$ was confirmed by Song et al. [114]. This

5. Rheological Experiments

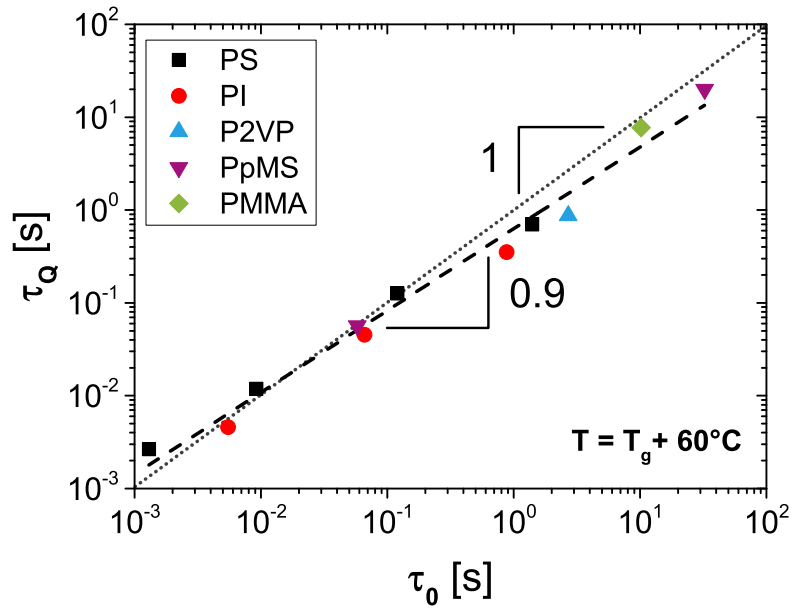


Figure 5.5.: Comparison of the longest relaxation time τ_0 with the relaxation time $\tau_Q = 1/\omega_{max}$ (see fig. 5.3). The experimentally determined scaling of 0.9 and the the expected scaling of 1 ($\tau_Q = \tau_0$) are displayed. Entanglement range from $Z = 1.4$ to 17.6 (also see Tab. 5.1).

similarity, between nonlinear and linear relaxation times, shows that they can be associated with similar molecular dynamics and processes.

For further analysis with respect to the Pom-Pom and MSF constitutive models, as well as the proposed general equation (4.39) derived from these models, all nonlinear master curves are plotted against the Deborah number, $De = \omega\tau_0$. This results in a shift on top of each other of those ${}^3Q_0(De, Z)$ master curves, where the low frequency slopes, with a scaling of 2, coincide (fig. 5.6).

The obtained picture can be compared with the predicted general equation (4.39) from the Pom-Pom and MSF constitutive model. Figure 5.6 shows the fit of eq. (4.39) to all nonlinear master curves of low PDI polymers, with $k = 0.35$ as mean value for the decreasing slope after ${}^3Q_{0,max}$. This yielded the parameters a and b , which were plotted against the number of entanglements Z (fig. 5.7). A weak scaling law, related to the entanglement number Z for a and b , was found

5.3. Medium Amplitude Oscillatory Shear (MAOS) Experiments

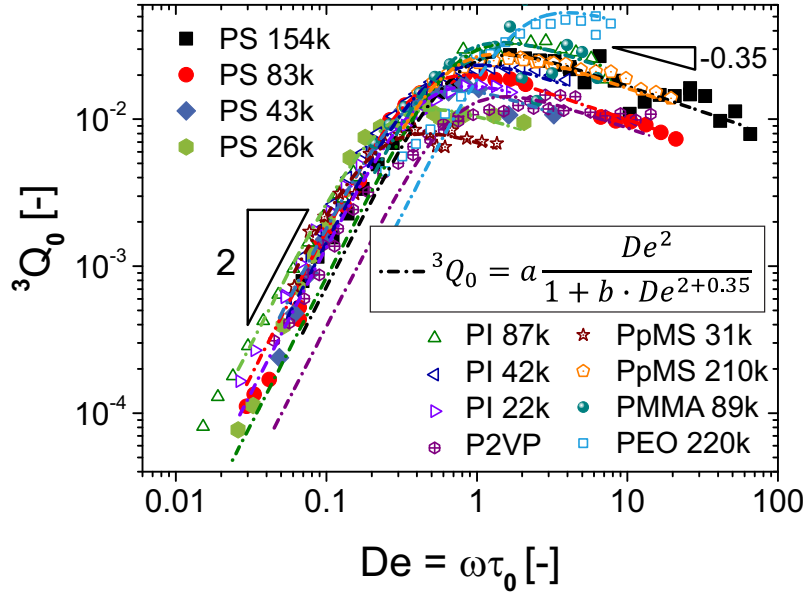


Figure 5.6.: Nonlinear master curves of monodisperse ($PDI \leq 1.07$) linear melts and related fits via eq. (4.39). Adapted from Cziep et al. [76].

for all investigated polymers, $a = A \cdot Z^{-0.5}$ and $b = B \cdot Z^{-1}$.

In a next step, an iteration (eq. 5.4) of equation (4.39), with the new scaling laws for a and b , was fitted on the experimental data with respective entanglement numbers for Z , and resulted average values for A and B .

$${}^3Q_0(De, Z) = A \cdot Z^{-0.5} \frac{De^2}{1 + B \cdot Z^{-1} De^{2+0.35}} \quad (5.4)$$

The values of A and B can be used in a final, empiric equation for ${}^3Q_0(De, Z)$, where the molecular weight, i.e. the entanglement number Z is a fitting parameter, and the Deborah number De , specifically the angular frequency ω , is used as variable for a unifying equation (eq. 5.5).

$${}^3Q_0(De, Z) = 0.32 \cdot Z^{-0.5} \frac{De^2}{1 + 33.8 \cdot Z^{-1} De^{2+0.35}} \quad (5.5)$$

$${}^3Q_{0,max}(Z) \approx 0.01Z^{0.35} \quad (5.6)$$

This equation approximately describes all monodisperse, linear homopolymer

5. Rheological Experiments

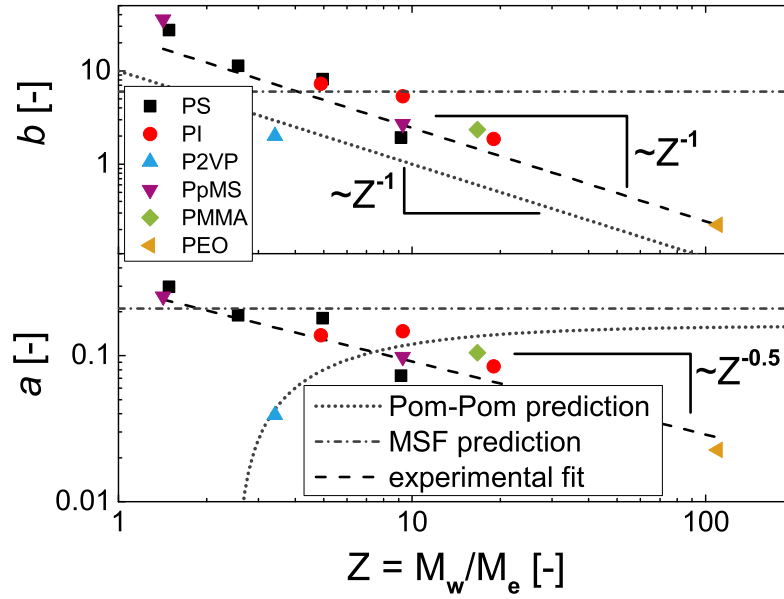


Figure 5.7.: Parameters a and b from eq. (4.39) for polymer samples with $\text{PDI} \leq 1.16$, along with predictions from the Pom-Pom constitutive model (pointed line) and MSF model (point-dash lines) as a function of Z . For exact parameter expressions see also tab. 5.3. Dashed lines indicate the power law behavior of each parameter from the experiment as $a \propto Z^{-0.5}$ and $b \propto Z^{-1}$ (adapted from [76]).

melts, independent of chemical composition within the investigated samples, and might be of high importance especially for molecular dynamic simulations.

The different parameters a , b and k from eq. (4.39) are presented in table 5.3 for the Pom-Pom and MSF model, and are compared to the semi-empiric equation (5.5).

Figure 5.8 shows the predictions from the Pom-Pom and MSF model with expe-

Model	a	b	k	${}^3Q_{0,max}$
Pom-Pom	$1/(2\pi)(1 - 2.5Z^{-1})$	$10Z^{-1}$	1	$1/(4\pi)^*$
MSF	$1.5(\alpha - \beta/10)$	6	0	$0.25(\alpha - \beta/10)$
Experiment	$0.32Z^{-0.5}$	$33.8Z^{-1}$	0.35	$\propto Z^{0.35}$

* for $Z \rightarrow \infty$; see also fig. 5.4

Table 5.3.: Parameters for eq. (4.39), as predicted by the Pom-Pom and MSF constitutive model, as well as results from fits on experimental data as presented in eq. (5.5).

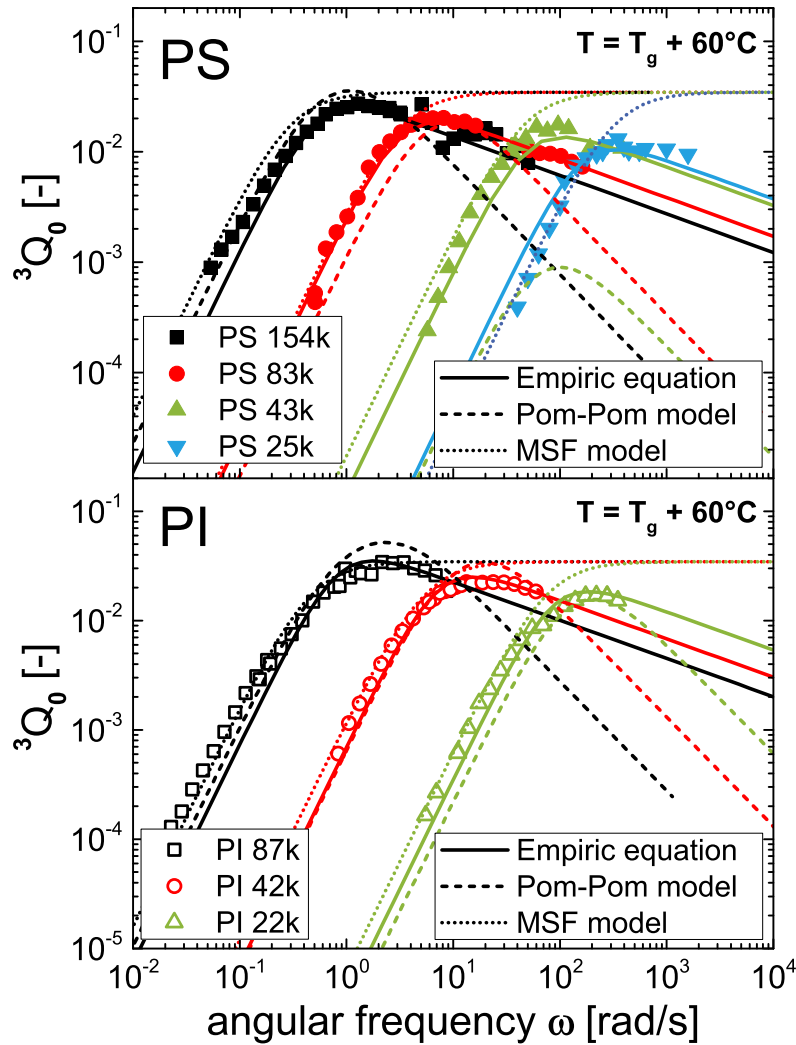


Figure 5.8.: Predictions of the simplified single mode Pom-Pom (dashed lines, eq. 4.19) and simplified single mode MSF (dotted lines, eq. 4.37) model, measured data (symbols) and predictions from the here presented semi-empiric equation (full lines, eq. 5.5). Adapted from Cziep et al. [76].

rimental data, and the here presented semi-empiric equation (5.5) in comparison. For low frequencies, all three methods are able to depict the expected scaling of 2, but for high frequencies, only the semi-empiric expression is able to describe the full behavior of the experimental data. It should be mentioned, that the Pom-Pom model cannot predict ${}^3Q_0(De)$ for samples below a certain threshold of $M_w \leq 2.5Z$ (for example PS25k), since the entanglement number is too low or nonexistent (see also section 4.1.2).

5. Rheological Experiments

It was experimentally shown, that $A = 0.32$ and $B = 33.8$ from eq. (5.4) do not depend on the monomer for monodisperse, linear homopolymers, but rather only on the entanglement number Z . Therefore, eq. (5.5) seems to be a unifying quantification of nonlinear shear under MAOS conditions for these kind of polymer melts. The introduced simplified, single mode constitutive models are able to approximately predict these parameters (chapter 4). Nevertheless, for small polymers below a molecular weight with $Z \leq 3$, which is close to the critical molecular weight M_c (section 3.2.2), major discrepancies occur, especially for the Pom-Pom model (fig. 5.7). It was also shown that k is experimentally around 0.35 for monodisperse samples, where its predicted value is either $k = 0$ (MSF model), or $k = 1$ (Pom-Pom model).

Please note, that the sample PEO 1020k (see tab. 5.1), which has an extremely high number of entanglements with $Z = 510$, was excluded from the here presented iterative step-by-step evaluation. The reason is, that the measured ${}^3Q_0(\omega)$ master curve of this sample, could not be predicted by the found semi-empiric equation (5.5), using the parameter values of $A = 0.32$ and $B = 33.8$ (fig. 5.9).

Fetters and coworkers [70, 118] stated, that the transition from a dominating Rouse behavior and contour length fluctuation (CLF) to pure reptation of a polymer chain takes place at a reptation molecular weight M_r (see also section 3.2.2), which is a function of the polymer specific packing length p . From all investigated polymer samples in this work, only the sample PEO 1020k exceeds the threshold of M_r . Therefore, a change in molecular dynamics is assumed due to the extremely high molecular weight [119] ($M_w = 1020 \text{ kg/mol} \gg M_r(\text{PEO}) \approx 680 \text{ kg/mol}$). The influence of chain end dynamics to the overall molecular relaxation spectrum diminishes for ultra-high molecular weight polymers, which could be of interest for further investigation of nonlinear mechanical behavior.

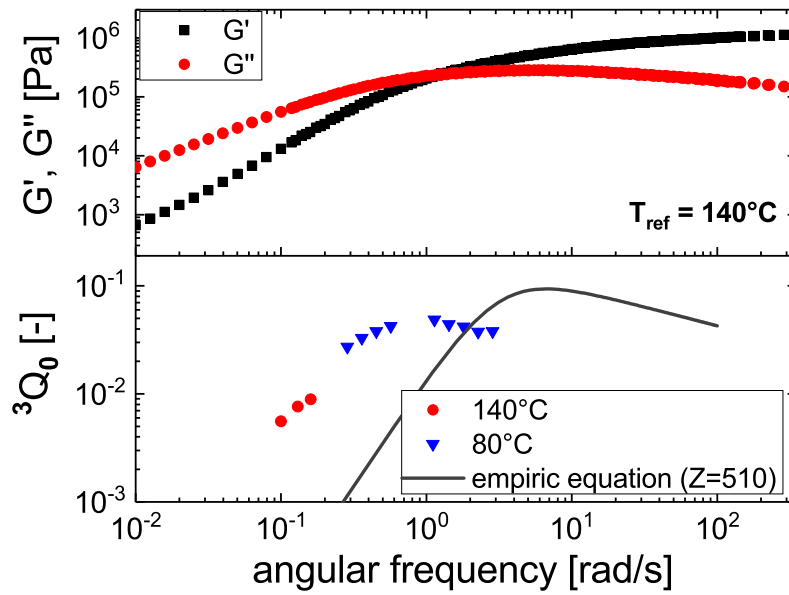


Figure 5.9.: Linear and nonlinear master curve of PEO1020k. The prediction from eq. (5.5) (full line) does not conform the measured ${}^3Q_0(\omega)$ master curve (symbols). Instead ${}^3Q_{0,max}$ has a lower value and appears at a lower frequency than expected.

Effect of Polydispersity

Polydisperse, linear homopolymer melts were investigated with the MSF constitutive model. Fix values were chosen for the nonlinear parameters, $\alpha = 5/21$ and $\beta = 1.0$. The summation of a relaxation spectrum from each investigated sample was used to calculate the real and imaginary parts of the higher harmonic intensities I_1 and I_3 , i.e. I'_1, I'_3, I''_1 and I''_3 , for every sample individually. Each spectrum was calculated, using relaxation spectra of G_i and $De_i = \omega\tau_i$, instead of G_N^0 and $De = \omega\tau_0$ in eqs. (4.30) to (4.33). The relaxation spectra (G_i and τ_i , see Tab. 5.4) were experimentally obtained from the storage and loss moduli of respective linear master curves. Finally, a linear summation of the obtained spectra were used to calculate the 3Q_0 parameter. Figure 5.10 depicts the simulation along with experimental ${}^3Q_0(\omega)$ data. A wavy form is obtained for the simulation of ${}^3Q_0(\omega)$ instead of a smooth curve, due to the limited and fixed number of relaxation times, which were used (see tab. 5.4). Direct comparison shows the accordance

5. Rheological Experiments

PS 340k (1.15)		PS 186k (2.33)		PS 602k (4.70)			
$G_i[Pa]$	$\tau_i [s]$	$G_i[Pa]$	$\tau_i [s]$	$G_i[Pa]$	$\tau_i [s]$		
1.89E+7	6.65E-6	8.87E+6	1.11E-5	1.13E+7	9.45E-6		
5.85E+5	2.11E-4	5.09E+5	2.26E-4	3.81E+5	3.94E-4		
1.69E+5	1.94E-3	1.53E+5	2.13E-3	9.90E+4	4.31E-3		
5.59E+4	1.75E-2	6.57E+4	2.00E-2	3.77E+4	5.28E-2		
4.08E+4	1.46E-1	4.97E+4	1.68E-1	3.39E+4	5.22E-1		
4.50E+4	9.46E-1	3.67E+4	1.23E+0	3.83E+4	4.26E+0		
4.90E+4	5.43E+0	2.47E+4	8.40E+0	4.39E+4	3.47E+1		
4.83E+4	3.06E+1	1.75E+4	6.02E+1	3.42E+4	3.02E+2		
1.04E+4	1.05E+2	7.87E+3	4.47E+2	1.35E+4	2.22E+3		
		1.27E+3	3.24E+3	3.12E+3	1.56E+4		
PS 112k (1.66)		PS 107k (2.00)		HDPE 155k (15.0)		HDPE 338k (27.2)	
$G_i[Pa]$	$\tau_i [s]$	$G_i[Pa]$	$\tau_i [s]$	$G_i[Pa]$	$\tau_i [s]$	$G_i[Pa]$	$\tau_i [s]$
1.34E+7	8.08E-6	1.21E+7	8.53E-6	2.34E+6	4.27E-3	2.39E+5	1.26E-2
5.13E+5	2.57E-4	4.73E+5	2.88E-4	5.35E+5	3.87E-2	9.43E+4	1.10E-1
1.68E+5	2.58E-3	1.53E+5	3.05E-3	1.76E+5	2.81E-1	4.42E+4	1.01E+0
9.08E+4	2.27E-2	7.95E+4	2.69E-2	3.39E+4	2.54E+0	1.30E+4	1.19E+1
5.48E+4	1.52E-1	3.97E+4	1.81E-1				
1.89E+4	8.44E-1	1.09E+4	1.03E+0				
2.08E+3	4.46E+0	9.93E+2	5.57E+0				

Table 5.4.: Relaxation spectra of polydisperse samples at $T(\text{PS}) = 160^\circ\text{C}$ and $T(\text{HDPE}) = 140^\circ\text{C}$. The data was obtained from respective linear master curves of $G'(\omega)$ and $G''(\omega)$. The polydispersity index is given in brackets.

of the multi mode MSF model prediction with the experimental data within our experimental window. However, as mentioned before, the MSF constitutive model cannot predict the decrease of nonlinear master curves, with ${}^3Q_0(\omega) \propto \omega^{-0.35}$, for high frequencies after the maximum ${}^3Q_{0,max}$, even for monodisperse samples. For smaller frequencies (${}^3Q_0(\omega)$ with $\omega < \omega_{max}$) the MSF prediction shows the expected scaling exponent of 2, ${}^3Q_0(\omega) \propto \omega^2$. For increasing ω , a decreasing slope in ${}^3Q_0(\omega)$ is observed until ${}^3Q_0(\omega) = \text{const.}$ at ${}^3Q_{0,max}$ and for $\omega > \omega_{max}$. The MSF constitutive model therefore predicts the same scaling behavior for all linear polymer melts, independent of dispersity. The experimental window however is typically limited to $10^{-3} \leq De \leq 10^3$, and the low frequency ranges, that are needed to obtain the expected scaling of 2 (see also fig. 5.11), could not be

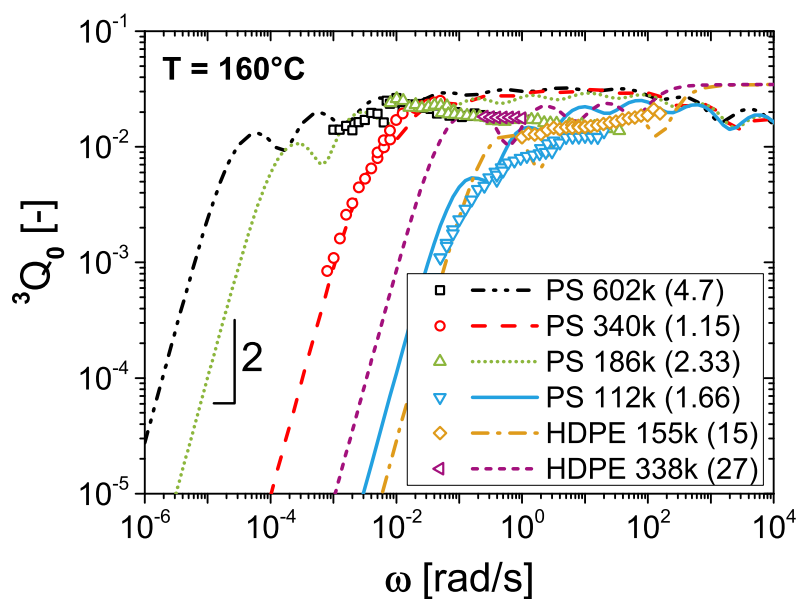


Figure 5.10.: Experimental ${}^3Q_0(\omega)$ data of polydisperse linear polymer melts along with respective Molecular Stress Function (MSF) model predictions (PDI given in brackets). The low frequency region, where ${}^3Q_0(\omega) \propto \omega^2$, is hardly accessible for some polymer measurements because of instrumental and experimental limitations. This is especially valid for high polydispersities and high molecular weights. Figure adapted from [76].

approached with our instrumental setup. Within the experimental window, the prediction overlaps approximately with our experimental data.

In figure 5.11 several ${}^3Q_0(De)$ master curves for polymer samples with different polydispersities are presented. In this figure, the relaxation time τ_{co} , from the crossover of G' and G'' , was used to calculate De . The high polydispersity shifts the linear terminal regime to very low frequencies, where very high measurement temperatures are needed. Therefore it was not possible to obtain reliable data for the longest relaxation time τ_0 via the zero shear viscosity η_0 with eq. (5.3) for all samples, and τ_{co} was used instead.

A scaling of approximately ${}^3Q_0(De) \propto De^2$ for low frequencies, before the maximum ${}^3Q_{0,max}$, was observed for all linear monodisperse polymers in this work (see fig. 5.3 or fig. 5.6). With increasing PDI, the slope of ${}^3Q_0(De)$ for low frequen-

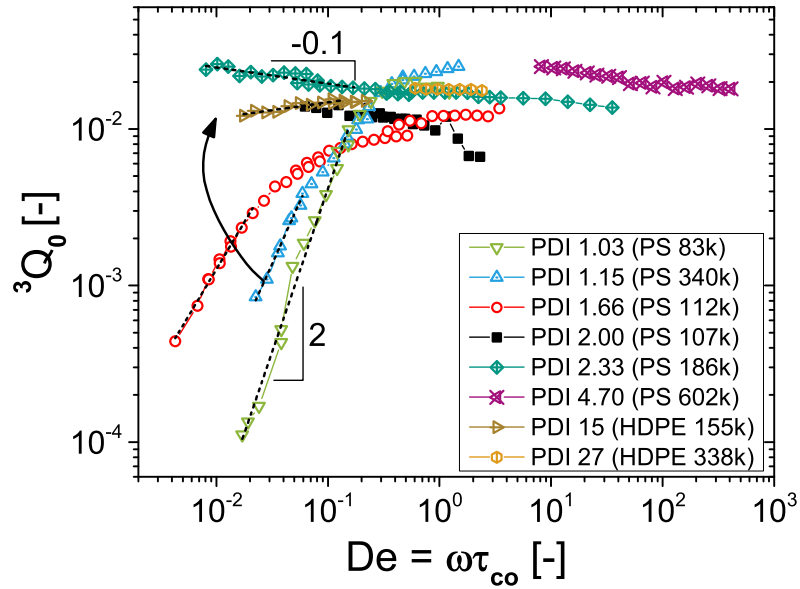


Figure 5.11.: Nonlinear master curves of linear polymer melts with different polydispersities. With increasing PDI, the slope at low frequencies decreases from 2 for monodisperse polymers, to -0.1 for the shown polymer sample with the highest PDI of 27 (adapted from [76]).

cies decreases, until it levels off at a constant value, which equals ${}^3Q_{0,max}$, within the measured frequency range and accessible intensity range of $I_{3/1}(\gamma_0)$ for samples with a $PDI \geq 2$. The experiments show a dependence of the low frequency scaling ${}^3Q_0(De) \propto De^n$ on the PDI. The following empiric equation (5.7) can describe this observation with a minimum set of parameters at $De = 0.02$, where the scaling of $n = 2$ for monodisperse samples ($PDI = 1$) is still given (fig. 5.12).

$$n = \frac{2}{PDI^{2.2}} \quad \text{for } De = 0.02 \quad (5.7)$$

It is shown by the MSF model for polydisperse polymer melts (fig. 5.10), that the proportionality ${}^3Q_0(De) \propto De^2$ for extremely low frequencies is expected. However, to be able to detect this behavior in a very polydisperse sample, a sensitive measurement at a high temperature above the T_g in combination with a high activation energy and a low thermal degradation is desirable. This low frequency, needed to detect the expected quadratic scaling, might not always be accessible

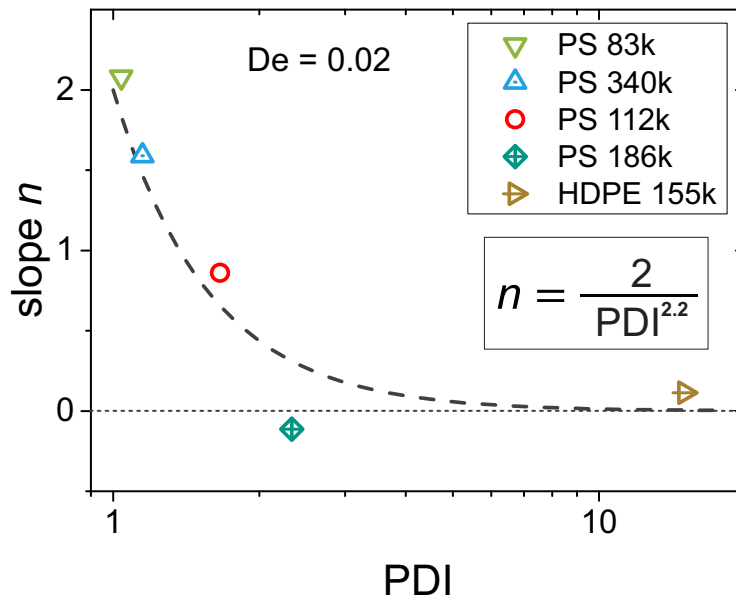


Figure 5.12.: Scaling exponents n from ${}^3Q_0(\omega) \propto \omega^n$ for $De = 0.02$ as a function of PDI (see related Fig. 5.11, adapted from [76]).

experimentally.

5.4. Rheological Characterization of Polymer Combs

5.4.1. Linear Mechanical Behavior (SAOS)

Components of a polymer comb behave rheologically different than their linear counterparts. Chain ends can move freely, while the covalent bonds reduce the degree of freedom in the inner molecule segments. The relaxation of the backbone is dominated by reptation (see section 3.3), but it is impeded by the traction of the sidearms [95, 105]. The linear master curve of the storage and loss modulus of a polyisoprene (PI) comb with $M_w = 340$ kg/mol and PDI = 1.06 is shown in figure 5.13 (for synthesis see section 2.4). Compared to its precursors (backbone $M_w = 142$ kg/mol, sidearms $M_w = 34$ kg/mol) the comb shows a hierarchical relaxation

5. Rheological Experiments

process. At higher frequencies the dynamics of the sidearms are observed. After full relaxation of the branches, the backbone reptation mechanism occurs at lower frequencies. The sidearms are partly folded up at these frequencies (primitive path fluctuations), which leads to a dynamic dilution effect for the backbone. As a result, the plateau modulus G_N^0 of the backbone is decreased proportionally to its volume fraction Φ_b , compared to a linear chain of same molecular weight [6, 124].

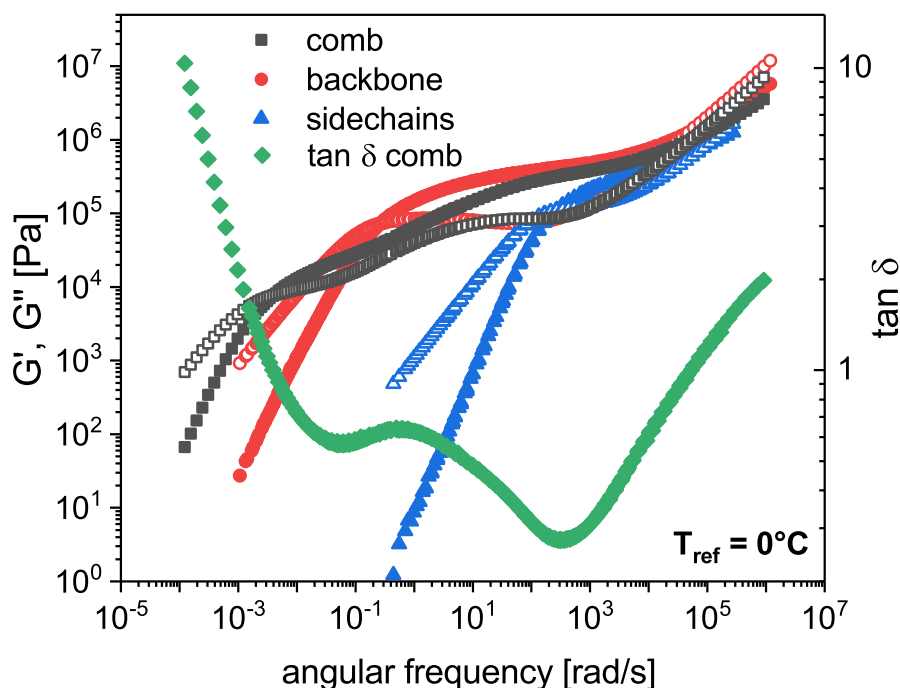


Figure 5.13.: Linear master curve of a PI comb with $M_w = 340$ kg/mol (squares). Master curves of the linear backbone (circles, $M_w = 142$ kg/mol) and isolated linear sidechains (triangles, $M_w = 34$ kg/mol) are also shown, to visualize the different linear mechanical behavior of the final comb and its educts.

Figure 5.14 shows the van Gurp-Palmen plot of the PI comb (340 kg/mol, 5.8 average number of sidearms with 34 kg/mol, PDI = 1.06) from fig. 5.13. The reduced van Gurp-Palmen plot can be used to compare different molecular topologies, for example polymer comb molecules with different number of sidearms and varying molecular weight [90, 116, 117]. Normalization of the complex modulus $|G^*|$ to the plateau modulus G_N^0 makes it invariant to temperature and time,

and therefore differences of these parameters between experiments are tolerated [112].

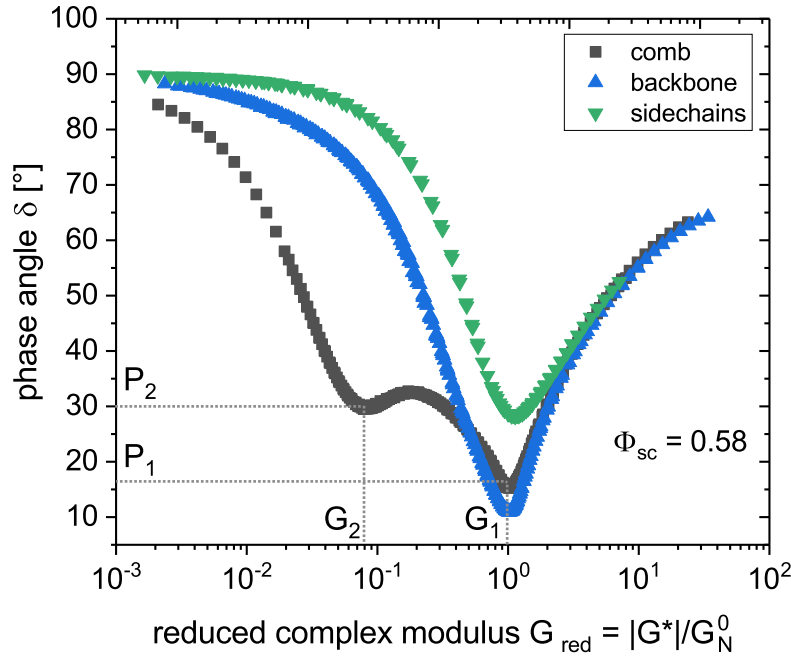


Figure 5.14.: Reduced van Gorp-Palmen plot of a PI comb with $M_w = 340$ kg/mol, a linear PI with same molecular weight as the comb backbone, $M_w = 142$ kg/mol, and a linear PI with similar molecular weight to the comb sidechains, $M_w = 33$ kg/mol. Characteristic points for the comb are sidechain relaxations (G_1 , P_1) and backbone relaxation (G_2 , P_2).

Kempf et al. [28] and Abbasi et al. [67] used the van Gorp-Palmen plot, or reduced van Gorp-Palmen plot respectively, to investigate a wide spectrum of model combs with varying branching content. Kempf et al. correlated a characteristic value G_2 of the reduced complex modulus $G_{red} = |G^*|/G_N^0$ (fig. 5.14) with the volume fraction Φ_{sc} of the branches. They proposed a linear relationship between G_2 and Φ_{sc} , which depends on the entanglement (i.e. slightly or well-entangled) of the sidearms and a dynamic dilution effect [28]. An increasing volume fraction Φ_{sc} of the sidearms leads to a stronger dynamic dilution, as the number of entanglements also increases.

Conclusion

The here described rheological results on a well characterized polyisoprene comb, that were conducted in the linear mechanical regime, indicate that the investigation of branched structures is still germinal. Especially the influence of the monomer is not yet full understood. A well established synthesis route for model comb polymers, chemically different to the well investigated polystyrene structures, will prove to be valuable in further investigations on the dynamics of branched polymers.

5.4.2. Nonlinear Mechanical Behavior (MAOS)

The mechanical nonlinear behavior of well-defined branched model polymers was first executed by Hyun et al. [23] and Kempf et al. [28]. Their measurements of ${}^3Q_0(\omega)$ showed two maximum values, which they related to relaxations of the backbone and the sidechains. However, a quantitative description of the intrinsic nonlinearity ${}^3Q_0(\omega)$ could not be achieved in their early publications.

The newly found semi-empirical equation (5.5) from this thesis, showed good accordance to experimental data of monodisperse, linear homopolymer melts (see fig. 5.8). It is therefore possible, to perform predictions of nonlinear master curves with ${}^3Q_0(\omega)$ for various polymer melts with varying molecular weights, even though a sample is not available for rheological measurements. However, the general framework of monodispersity and linear topology needs to be adhered to. Equation (5.5) was then used to predict the intrinsic nonlinearity ${}^3Q_0(\omega)$ of linear polymers with the same molecular weight, or number of entanglements Z , as the backbone and sidechains of a polymer model comb from Hyun et al. [23] and

5.4. Rheological Characterization of Polymer Combs

Kempf et al. [28] (see fig. 5.15), as well as a PI comb, synthesized in this work (see section 2.4, and fig. 5.16).

The two investigated combs from Hyun and Kempf have a PS backbone with $M_w = 275$ kg/mol ($Z = 16.4$) and 29 PS sidearms with $M_w = 47$ kg/mol ($Z = 2.8$, PS 275k-29-47k), and a PpMS backbone of $M_w = 197$ kg/mol ($Z = 8.1$) with 14 PpMS sidearms of $M_w = 42$ kg/mol ($Z = 1.7$, PpMS 197k-14-42k). Figure 5.15 shows the experimental data from Hyun and Kempf [23, 28]. The dashed lines are predictions from the semi-empiric equation (5.5) for referring linear polymers of the backbones and sidearms. The Deborah number, needed for eq. (5.5), of each linear backbone and linear sidearm was calculated with $De = \omega\tau_0$, using the relation of $\tau_Q = \tau_0^{0.9}$ (see fig. 5.5), where τ_Q was determined from the two maxima (one maximum for the backbone, one for the sidearms) of the measured nonlinear master curves of the comb (symbols in fig. 5.15). It is apparent, that the predictions for the backbone imply 5 to 6 times higher values than the experimental data shows. The sidechain predictions however are very similar to the experiment. A very simplified conception is to describe a well-defined polymer comb as a bidisperse melt, in which some molecules are chemically connected. The sum function (5.8) of the semi-empirical equation (5.5) could therefore be the simplest possible approach, to describe the intrinsic nonlinearity of a comb, following the multi-mode MSF model concept for polydisperse melts (see fig. 5.10 in section 5.3).

$${}^3Q_0(\omega) = \Phi_b {}^3Q_{0,b}(\omega) + \Phi_{sc} {}^3Q_{0,sc}(\omega) \quad (5.8)$$

Using the volume fraction Φ_b of the backbone as a multiplying factor, equation (5.8) results a prediction of ${}^3Q_0(\omega)$ similar to the obtained experimental data (full lines in fig. 5.15). The maximum of ${}^3Q_0(\omega)$ for the backbone and the sidechains only deviate slightly from the measurement and the overall curve is in good accordance to the experiment.

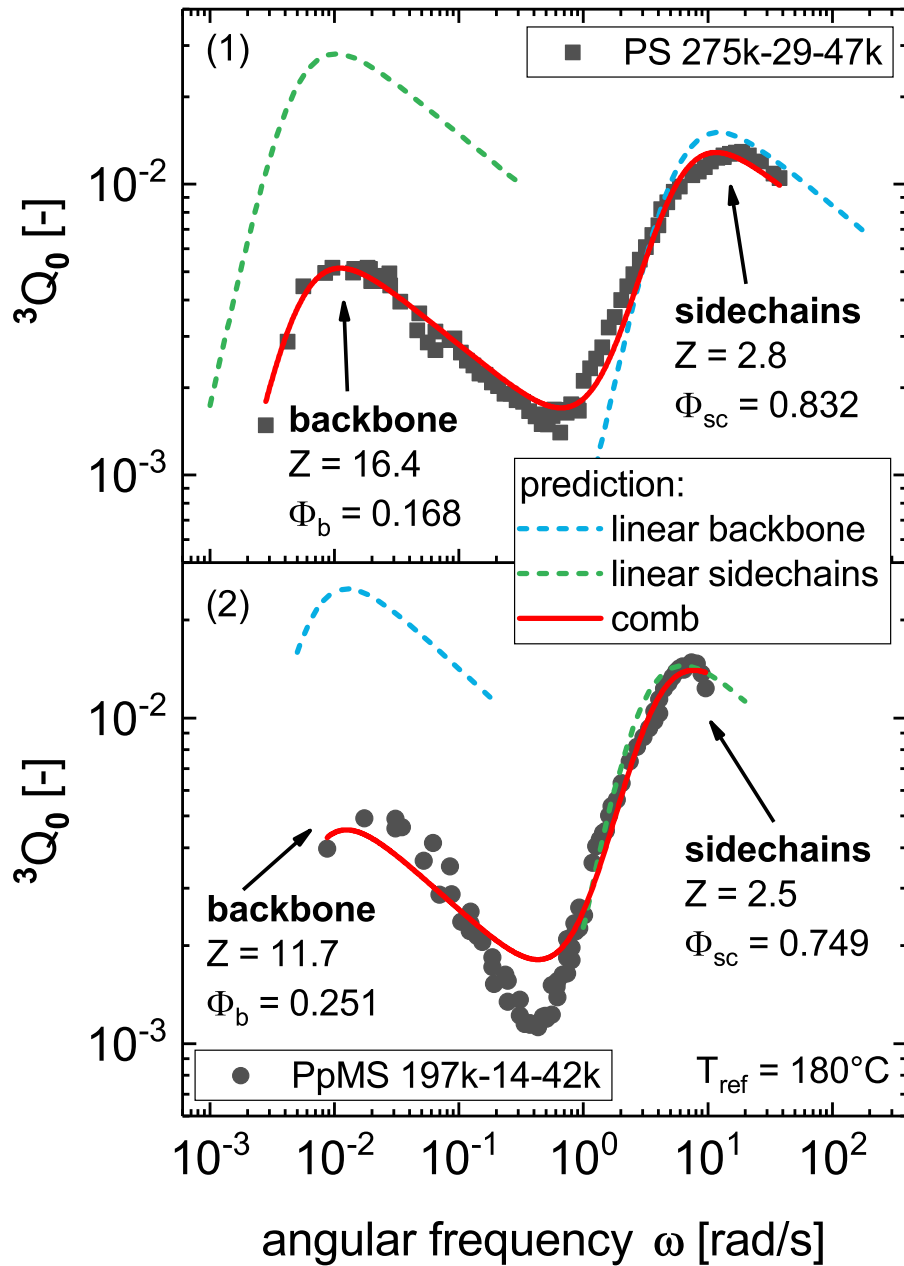


Figure 5.15.: Nonlinear master curves of a PS (1) and PpMS (2) model comb (data from Hyun and Kempf et al. [23, 28]). A sum function (eq. 5.8), which includes the volume fraction Φ_b of the backbone, was used to predict the nonlinear behavior for the combs (line), in contrast to predictions for respective linear homopolymers (eq. 5.5, dashed lines).

5.4. Rheological Characterization of Polymer Combs

The synthesized PI comb in this thesis (backbone $M_w = 142$ kg/mol, sidechain $M_w = 34$ kg/mol, number of sidechains 5-6, see fig. 2.18) allowed to directly measure the longest relaxation time τ_0 of the not connected, linear backbone and sidechains independently (section 5.4.1), as opposed to the combs of Hyun and Kempf, from which the linear data was not accessible. The relaxation time τ_0 was then used in the prediction of the intrinsic nonlinearity ${}^3Q_0(\omega)$ with equations (5.5) and (5.8). This allows to investigate and correlate the influence of the attached sidechains onto the linear backbone in more detail. The linear and nonlinear master curve of the PI comb are shown in figure 5.16. Predictions from the semi-empirical equation (5.5) for the linear backbone and the sidechains, and from the sum function (5.8) for the comb, are compared to the experimental results of the linear and nonlinear master curves.

The predicted maximum values of ${}^3Q_0(\omega)$ for the backbone and the sidechains are similar to the measured data. However, the frequency of the predicted maxima is around two decades too high and, for the backbone, is located near the crossover frequency of the related linear master curve ($\omega_{co} = 3 \cdot 10^{-3}$ rad/s). The implied ${}^3Q_0(\omega)$ maximum, related to the sidechains, is also close to the indicated longest relaxation of the sidechains, which can be identified by a local maximum of the $\tan \delta$ around $\omega = 1$ rad/s in figure 5.16. This behavior was also observed for linear homopolymer melts, where the maximum ${}^3Q_{0,max}$ always resides near the frequency of the longest relaxation time, as shown by $\tau_Q = \tau_0^{0.9}$ (also see fig. 5.5 and 5.2). A correlation between the molecular dynamics in the linear and nonlinear regime via the longest relaxation time τ_0 can therefore be estimated.

These first results show, that the intrinsic nonlinearity ${}^3Q_0(\omega)$ could be a summation of the nonlinear behavior of involved molecules via the volume fraction. It is assumed that the attached sidechains reduce the backbone mobility, hence the shift of the backbone maximum to lower frequencies. At the same time, the

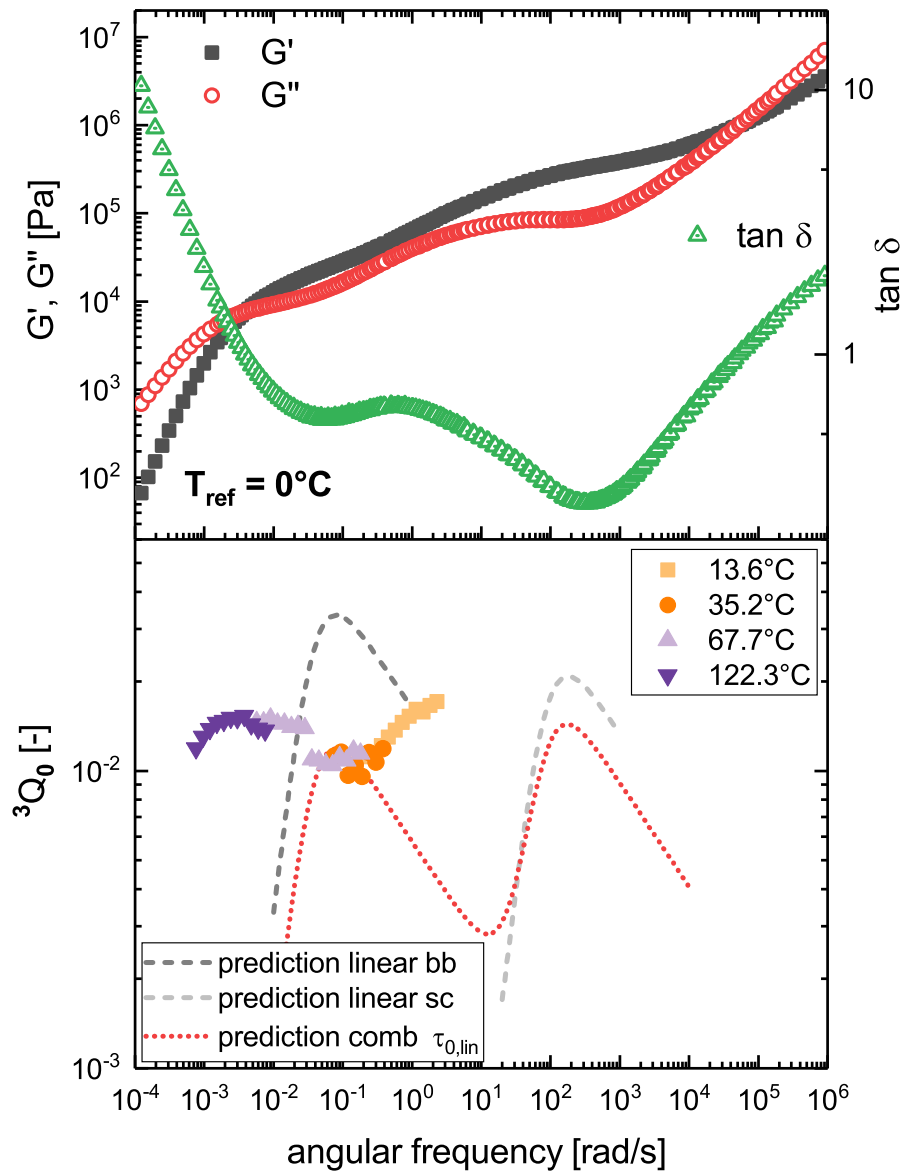


Figure 5.16.: Linear and nonlinear master curves of a PI comb (340 kg/mol, backbone 142 kg/mol, sidechains 34 kg/mol). The predicted intrinsic nonlinearity ${}^3Q_0(\omega)$ from eq. (5.5) (dashed lines) for a linear backbone (bb) and linear sidechains (sc), and the prediction from eq. (5.8) (dotted line) for a respective comb is compared to experimental data (symbols).

sidechain relaxations are also reduced by the backbone, since their ${}^3Q_0(\omega)$ maximum is also shifted to lower frequencies than expected from equations (5.5) and (5.8).

5.5. Conclusion

The here presented results of linear ($G'(\omega)$, $G''(\omega)$) and nonlinear (${}^3Q_0(\omega)$) master curves investigated the molecular dynamics of linear homopolymer melts with varying molecular weight, molecular weight distribution and polymer. A successful quantification of the intrinsic nonlinearity ${}^3Q_0(\omega)$ was achieved via a semi-empirical approach, with the help of constitutive models (Pom-Pom and MSF). The obtained description (eq. 5.5) is independent of the polymer, and only contains the number of entanglements Z , and the Deborah number De . These results were then applied to predict the nonlinear mechanical behavior of model combs (eq. 5.8). Within this attempt, it was revealed, that the quantification of the intrinsic nonlinearity ${}^3Q_0(\omega)$ for branched polymers and clarification of underlying physics has still to be researched.

6. Conclusion and Outlook

Summary

The mechanical nonlinear behavior of homogeneous molten polymers is of high interest for the processing industry. Correlations between molecular microstructure, such as the molecular weight, molecular weight distribution, monomer chemistry and topology, and the rheological behavior in the nonlinear regime are still not fully understood. The goal of this thesis was to contribute to this field of research by investigating the intrinsic nonlinearity ${}^3Q_0(\omega)$ of defined polymer melts. A series of well-characterized linear homopolymers was synthesized by anionic polymerization (table 7.1). It was taken care, that a broad variety of chemically different polymers was chosen. Polystyrene (PS), poly-*p*-methylstyrene (PpMS) and *cis*-1,4-polyisoprene (PI) are unpolar, yet they exhibit very different chain mobilities and glass transition temperatures T_g (table 5.1). Poly(methyl methacrylate) (PMMA) and poly-2-vinylpyridine (P2VP) introduce heteroatoms in the substituents, whereas poly(ethylene oxide) (PEO) does this within the chain backbone. PEO and high density polyethylene (HDPE), even though not polymerized within this thesis, were included and investigated because of their commercial importance. The total molecular weight of the samples was varied from nonentangled ($M_w < 3M_e$), to well-entangled ($M_w > 3M_e$), and even an outlook to ultra-high molecular weight ($M_w > 200M_e$) was given (section 5.4). The influence

6. Conclusion and Outlook

of polydispersity (PDI) was also investigated (section 5.3). Anionic polymerization results polymers with a PDI nearly 1. Utilizing other polymerization techniques (free radical and emulsion polymerization) polymer melts with molecular weight distributions up to 4.7 were realized, and HDPE samples with a PDI up to 27 were investigated for their nonlinear behavior. All synthesized polymers were fully characterized via gel permeation chromatography (GPC) to determine the molecular weight and polydispersity. Additionally, the microstructure ratio between 1,4 and 3,4 isomers of PI was identified with $^1\text{H-NMR}$. The glass transition temperatures T_g were obtained with differential scanning calorimetry (DSC). Rheological experiments were conducted on all linear homopolymer melts (chapter 5). First, small amplitude oscillatory shear (SAOS) frequency sweeps resulted linear master curves from $G'(\omega)$ and $G''(\omega)$ by exploiting the time-temperature superposition principle (TTS). From these linear master curves material properties were extracted, such as the Williams-Landel-Ferry (WLF) parameter, the plateau modulus G_N^0 , the entanglement molecular weight M_e , and the longest relaxation time τ_0 (section 5.1). Second, medium amplitude oscillatory shear (MAOS) strain sweeps were conducted on all polymer samples (section 5.2). Fourier Transformation of the time-dependent stress signal $\sigma(t)$ into the frequency spectrum revealed higher harmonic intensities of the excitation frequency $\omega_1/2\pi$. These higher harmonics started to rise out of the noise level with increasing shear rates. Especially the normalized third higher harmonic intensity $I_{3/1}(\gamma_0)$ was found to be sensitive to mechanical nonlinearity. Therefore, $I_{3/1}(\gamma_0)$ was used to calculate the nonlinear parameter $Q(\gamma_0) = I_{3/1}/\gamma_0^2$. Finally, the intrinsic nonlinearity ${}^3Q_0(\omega)$ was obtained as a frequency-dependent zero-shear nonlinearity, $\lim_{\gamma_0 \rightarrow 0} Q(\gamma_0) = {}^3Q_0(\omega)$. Using WLF parameter from respective linear master curves, allowed to create nonlinear master curves of ${}^3Q_0(\omega)$ (figure 5.7). It was observed, that all monodisperse ($PDI < 1.1$) homopolymer melts shared the same characteristic curve shape of ${}^3Q_0(\omega)$. A scaling of 2 (${}^3Q_0(\omega) \propto \omega^2$) was found for low frequencies, transitioning

into a maximum ${}^3Q_{0,max}$. At higher frequencies, after ${}^3Q_{0,max}$, values decreased with a negative scaling of -0.35 (${}^3Q_0(\omega) \propto \omega^{-0.35}$). In order to quantify the obtained nonlinear master curves, predictions from the Pom-Pom and molecular stress function (MSF) constitutive models were consulted (see chapter 4). The predictions match the scaling at low frequencies, though differ at high frequencies from the experimental findings (figure 5.9). The Pom-Pom model forecasts a scaling of -1, whereas the MSF model results a constant plateau at the value of ${}^3Q_{0,max}$.

A general, combined and simplified equation (eq. 5.4) from the Pom-Pom and MSF model was able to describe the nonlinear master curves of linear homopolymer melts with low PDI, independent of the investigated monomer, by fitting this equation to the experimental data. The proposed semi-empirical equation (eq. 5.5) includes two molecular weight dependent parameters $a = 0.32Z^{-0.5}$ and $b = 33.75Z^{-1}$, and a quadratic scaling of ${}^3Q_0(\omega)$ for frequencies below the maximum ${}^3Q_{0,max}$, and a scaling of $k = 0.35$ for the decreasing slope after the maximum for low PDI polymer melts.

Polymer melts with a PDI higher than 1.1 experimentally revealed a scaling exponent ${}^3Q_0 \propto De^n$ at low frequencies, that could be experimentally described by $n = 2/PDI^{2.2}$ for the measured frequency ranges of the nonlinear master curves (figure 5.12). Model prediction from the MSF constitutive model for high PDI polymers show, that at very low frequencies, the scaling of ${}^3Q_0 \propto \omega^2$ should be seen again (figure 5.10). This prediction however, is not accessible experimentally due to the potentially very high measurements temperatures, and the broad relaxation time distributions respectively, that are needed for such an experiment in addition to an instrument sensitivity that is currently not available.

In addition to the research on the nonlinearity of linear homopolymer melts, first steps towards a rheological investigation of topological more complicated poly-

6. Conclusion and Outlook

mers by the synthesis of PI combs was done (chapter 6). For isolated investigation of backbone and sidearm relaxation, a cooperation project was started to combine knowledge from low field double quantum NMR experiments and rheology. The synthesis of branched PI was achieved by oxidizing the inner double bonds of a linear monodisperse PI and introducing an epoxi functional group (section 2.4). This epoxi ring served as electrophile for living PI anions, which lead to the grafting of PI sidechains onto the functionalized PI backbone. The molecular weight of the newly formed comb and average number of sidearms was determined by SEC-MALLS (figure 2.17). Low field NMR investigation of separated molecule segments calls for partly deuterated PI combs. Therefore, first attempts to synthesize fully deuterated isoprene-d8 as a monomer were conducted (section 2.5). The precursor molecule could be prepared starting from water and carbide. ^1H -NMR revealed successful preparation (figure 2.20), however separation from the solvent via distillation kept challenging and could not be achieved within this thesis. The linear rheological investigation of the synthesized, protonated, PI comb showed typical branched polymer behavior by separation of backbone and sidearm relaxation (figure 6.1). The relaxation time of the backbone was also reduced due to hierarchical relaxation processes.

Perspective

The nonlinear mechanical behavior of viscoelastic polymer melts and solutions is a field of commercial interest and ongoing research. Within this work it was possible to describe mechanical nonlinear behavior with a semi-empirical equation, which includes only the number of entanglements Z and the Deborah number De . For the first time it was possible to quantify the intrinsic nonlinearity $^3Q_0(\omega)$ for linear homopolymer melts, independent of the chemical composition

of the polymer. It can therefore be assumed, that a universal physics is underlying all nonlinear motion effects for these class of polymers and topologies. The influence of various relaxation effects, such as reptation and contour path fluctuations were firstly observed in nonlinear master curves of polydisperse samples and an ultra-high molecular weight polymer. With these results and further developments in instrumentation and access to more powerful computation, the possibility for better knowledge about the macroscopic and microscopic level of polymeric materials is opened. Using the fundamental synthesis methods from this thesis, successful preparation of fully deuterated isoprene-d8 was achieved in the meanwhile, and first partly deuterated PI combs are in preparation, also utilizing the epoxidation route. These new polymeric materials offer the possibility to additionally investigate molecular relaxation modes of branched polymers with low field quantum NMR. Combining rheology and NMR promises to result deeper insight into molecular motion on different time scales. The results from this work are especially interesting for polymer processing at high shear rates. From an academical viewpoint, the presented experimental basic research can validate and expand existing theories about correlations between rheological behavior and molecular structure. The detailed investigation and quantification of the intrinsic nonlinearity ${}^3Q_0(\omega)$ on viscoelastic materials of various structures can lead to new developments in constitutive modeling and computer simulations, especially molecular dynamic simulations of polymer melts.

Appendix

A. Materials and Synthesis

A.1. Monomer and Solvent Purification

Styrene (Acros, 99%), *p-methylstyrene* (Acros, 98%), *methyl methacrylate* (Acros, 99%) and *2-vinylpyridine* (Aldrich, 97%) were first degassed by three freezing-evacuation-thawing cycles, then stirred over calcium hydride (CaH_2 ; Acros, 93%) over night. Afterwards, it was distilled at reduced pressure and stirred over di-*n*-butylmagnesium (Aldrich, 1 M in heptane) for 20 minutes. It was then distilled at reduced pressure into precalibrated ampoules and stored under argon at $-20\text{ }^\circ\text{C}$ until needed.

Isoprene (Acros, 98% stabilized) was stirred over *n*-butyllithium (*n*-BuLi; Aldrich, 2.5 M in hexanes) for no longer than 20 minutes in an ice bath. Then it was distilled at room temperature, first into a liquid nitrogen cooled flask at reduced pressure, then into precalibrated ampoules and stored under argon at $-18\text{ }^\circ\text{C}$ until needed.

Tetrahydrofuran (THF; Carl Roth, 99.5%) was first distilled from CaH_2 and then from sodium/benzophenone (Acros, 99%). It was stored over sodium benzophenone on the vacuum line prior to use.

Toluene (Carl Roth, 99.5%) was distilled from CaH_2 and stored over sodium benzophenone in a flask on the vacuum line.

A.2. Synthesis of Linear Homopolymers

A.2.1. Monodisperse Polymers by Anionic Polymerization

A high-vacuum technique ($\leq 10^{-3}$ mbar) was used to synthesize linear polystyrene (PS), polyisoprene (PI), poly(methyl methacrylate) (PMMA), poly(*p*-methylstyrene) (PpMS), and poly(2-vinylpyridine) (P2VP) samples with PDI < 1.2. The monomer ampoules were directly installed on the vacuum line with ground glass joints. After removal of the argon used for storage, the monomer was carefully freeze-dried with liquid nitrogen. Then, toluene was distilled over the vacuum line and freeze-dried into the ampoule. Once the compounds melted completely, they were thoroughly mixed and *s*-butyllithium (*s*-BuLi; Acros, 1.3 M in cyclohexane/hexane) was added as initiator with a syringe in an argon counterstream at room temperature. A deep orange (polystyrene) or a slightly yellow (polyisoprene) color indicated presence of the living anions of the polymers. After stirring with a magnetic stirrer at room temperature for several minutes (10 min for PS and PpMS, 30 min for PMMA and 60 min for PI), the reaction was terminated with degassed methanol (Carl Roth, 99%), at which any color disappeared immediately. The polymers were then precipitated in methanol (PMMA in water), redissolved in THF, and precipitated again in methanol.

For the synthesis of P2VP an initiator solution of *s*-BuLi in toluene was prepared with an excess of 10 mol% 1,1-diphenylethylene (DPE; Acros, 98%), which resulted in a deep red liquid. Pyridine (Carl Roth, $\geq 99.5\%$, p.a.) and THF (10:1 pyridine/THF) were distilled into a baked out and argon flushed reactor, where the 2-vinylpyridine ampoule and also the initiator ampoule were connected with ground glass joints. The reactor was cooled with an ice bath, and under stirring, first the initiator solution was dropped in thoroughly, then the 2-vinylpyridine monomer was added fast. A red color indicated the living polymer. After stirring

for 24 hours at room temperature, the reaction was stopped by adding degassed methanol until all color was vanished. P2VP was precipitated in petroleum ether (Acros, boiling range 40 °C to 60 °C).

The final products were filtered and dried under reduced pressure at 70 °C, and PMMA at 150 °C respectively, for at least three days to remove residual amounts of solvents. Polyisoprene samples were further stabilized with 0.5 wt% BHT (2,6-di-*tert*-butyl-4-methylphenol; Acros, 99%).

A.2.2. Polydisperse Polymers by Free Radical and Emulsion Polymerization

Polystyrene samples with a polydispersity higher than 1.2 were synthesized with free radical polymerization or with emulsion polymerization. For free radical polymerization Azobis(isobutyronitrile) (AIBN; Aldrich, 98%) was used as initiator. Styrene was given into a small flask and after adding the initiator, the mixture was stirred under argon at 60 °C for 24 hours. The reaction was continued for another two days at room temperature, with stirring as long as possible, before THF was used to dissolve the product. The polymer was precipitated in fresh methanol and dried under reduced pressure at 70 °C.

For emulsion polymerization, distilled water, a 10 wt% aqueous solution of sodium dodecylsulfate (Aldrich, 99%) as emulsifier, and styrene were given into a flask with a sealed precision glass (KPG) stirrer. After stirring for 30 minutes under argon, the emulsion was heated to 80 °C and the reaction was started by adding solid potassium peroxydisulfate ($K_2S_2O_8$; Aldrich, 99%) as initiator. Heating and stirring was continued for 6 hours. The reaction was stopped by adding a 4% aqueous solution of 1,4-dihydroxybenzene (hydroquinone; Acros, 99,5%)

A. Materials and Synthesis

and cooling with an ice bath to room temperature. To remove the emulsifier, concentrated hydrochloric acid (Acros, 37% in water) was added. The sediment was then washed with distilled water until it was neutral ($6 \leq \text{pH} \leq 7$) and washed with methanol until styrene smell could no longer be observed.

A.3. Molecular Characterization

The number and weight average molecular weight (M_n and M_w) and polydispersity index ($PDI = M_w/M_n$) of the samples were determined with size exclusion chromatography (SEC). The SEC system consisted of an Agilent 1100 pump, an Agilent 1200 differential refractive index (DRI) and UV detector with two PSS SDV Lux 8 mm \times 300 mm columns (10^3 Å and 10^5 Å pore size). The SEC analysis was done in THF at 25 °C with a flow rate of 1 ml min⁻¹.

¹H-NMR spectroscopy was performed in deuterated chloroform (CDCl₃) at 25 °C with a Bruker Avance III Microbay 400 MHz spectrometer and 512 scans. The amount of *cis/trans*-1,4 and 3,4 microstructure in the polyisoprene samples was determined by the peak intensity ratio of the =CH- signal from the 1,4 microstructure (one proton) between 4.9 ppm to 5.2 ppm, and the =CH₂ signal from the 3,4 microstructure (two protons) between 4.6 ppm to 4.8 ppm (see fig. 2.14) [107]. The epoxidation ratio for functionalized polyisoprenes was calculated from the integral of the single proton signal at 2.7 ppm, which was compared to the above mentioned 1,4- and 3,4 microstructure signal integrals (see fig. 2.16).

Differential scanning calorimetry (DSC), using a DSC30 from Mettler Toledo, with a heat rate of 10 °C/min over two separated heat runs was used to obtain glass transition temperatures T_g of each samples.

B. Model Calculations

This section includes step-by-step calculations of the simplified Pom-Pom and Molecular Stress Function (MSF) constitutive models for the intrinsic nonlinearity ${}^3Q_0(De)$ (see chapter 4).

B.1. Calculation of the Intrinsic Nonlinearity

B.1.1. Pom-Pom Model

The definition of the intrinsic nonlinearity ${}^3Q_0(De)$, and the real and imaginary parts of the higher harmonic intensities I_1 and I_3 in the Pom-Pom model are given in the following.

$${}^3Q_0(De) = \lim_{\gamma_0 \rightarrow 0} \frac{I_3}{I_1 \gamma_0^2} \quad (\text{B.1})$$

$$I_1' = G_N^0 \left(\frac{De^2}{1 + De^2} \right) \gamma_0 \quad (\text{B.2})$$

$$I_1'' = G_N^0 \left(\frac{De}{1 + De^2} \right) \gamma_0 \quad (\text{B.3})$$

$$I_3' = G_N^0 \left(\frac{De^4 C_1 C_3'}{\pi C_2 (1 + De^2)^2} \right) \gamma_0^3 \quad (\text{B.4})$$

$$I_3'' = G_N^0 \left(\frac{De^3 C_1 C_3''}{2\pi C_2 (1 + De^2)^2} \right) \gamma_0^3 \quad (\text{B.5})$$

B. Model Calculations

with

$$C_1 = 1 - 2.5Z^{-1} \quad (\text{B.6})$$

$$C_2 = (1 + 25De^2Z^{-2})(1 + 4De^2) \quad (\text{B.7})$$

$$C'_3 = De^2 + 12.5De^2Z^{-1} - 2 - 2.5Z^{-1} \quad (\text{B.8})$$

$$C''_3 = 10De^4Z^{-1} - 5De^2 - 20De^2Z^{-1} + 1 \quad (\text{B.9})$$

The higher harmonic intensity I_1 can then be calculated.

$$I_1 = \sqrt{I_1'^2 + I_1''^2} \geq 0 \quad (\text{B.10})$$

$$I_1 = \sqrt{\left(G_N^0 \left(\frac{De^2}{1 + De^2}\right) \gamma_0\right)^2 + \left(G_N^0 \left(\frac{De}{1 + De^2}\right) \gamma_0\right)^2} \quad (\text{B.11})$$

$$I_1 = \sqrt{G_N^0{}^2 \gamma_0^2 \left(\frac{De^4}{(1 + De^2)^2} + \frac{De^2}{(1 + De^2)^2}\right)} \quad (\text{B.12})$$

$$I_1 = \frac{G_N^0 \gamma_0 De}{1 + De^2} \sqrt{De^2 + 1} \quad (\text{B.13})$$

$$I_1 = \frac{G_N^0 \gamma_0 De}{(1 + De^2)^{0.5}} \quad (\text{B.14})$$

The same calculation steps can be done to obtain the higher harmonic intensity

I_3 .

$$I_3 = \sqrt{I_3'^2 + I_3''^2} \geq 0 \quad (\text{B.15})$$

$$I_3 = \sqrt{\left(G_N^0 \left(\frac{De^4 C_1 C'_3}{\pi C_2 (1 + De^2)^2}\right) \gamma_0^3\right)^2 + \left(G_N^0 \left(\frac{De^3 C_1 C''_3}{2\pi C_2 (1 + De^2)^2}\right) \gamma_0^3\right)^2} \quad (\text{B.16})$$

$$I_3 = \sqrt{\frac{G_N^0{}^2 \gamma_0^6 De^6 C_1^2}{4\pi^2 C_2^2 (1 + De^2)^4} (4De^2 C_3'^2 + C_3''^2)} \quad (\text{B.17})$$

$$I_3 = \frac{G_N^0 \gamma_0^3 De^3 C_1}{2\pi C_2 (1 + De^2)^2} \sqrt{4De^2 C_3'^2 + C_3''^2} \quad \text{for } Z > 2.5 \quad (\text{B.18})$$

Insertion of I_1 (eq. B.14) and I_3 (eq. B.18) into eq. (B.1) results ${}^3Q_0(De)$ for the single mode Pom-Pom constitutive model.

$${}^3Q_0(De) = \lim_{\gamma_0 \rightarrow 0} \frac{\frac{G_N^0 \gamma_0^3 De^3 C_1}{2\pi C_2 (1+De^2)^2} \sqrt{4De^2 C_3'^2 + C_3''^2}}{\frac{G_N^0 \gamma_0 De}{(1+De^2)^{0.5}} \gamma_0^2} \quad (\text{B.19})$$

$${}^3Q_0(De) = \frac{De^2 C_1 (1+De^2)^{0.5}}{2\pi C_2 (1+De^2)^2} \sqrt{4De^2 C_3'^2 + C_3''^2} \quad (\text{B.20})$$

$$\begin{aligned} {}^3Q_0(De) &= \frac{De^2 (1 - 2.5Z^{-1})}{2\pi (1 + 25De^2 Z^{-2})(1 + 4De^2)(1 + De^2)^{1.5}} \\ &\cdot \sqrt{4De^2 (De^2 + 12.5De^2 Z^{-1} - 2 - 2.5Z^{-1})^2} \\ &\quad + (10De^4 Z^{-1} - 5De^2 - 20De^2 Z^{-1} + 1)^2} \end{aligned} \quad (\text{B.21})$$

$$\begin{aligned} {}^3Q_0(De) &= \frac{De^2 (1 - 2.5Z^{-1})}{2\pi (1 + 25De^2 Z^{-2})(1 + 4De^2)(1 + De^2)^{1.5}} \\ &\cdot \sqrt{(1 + 25De^2 Z^{-2})(1 + 4De^2)(1 + De^2)^2} \end{aligned} \quad (\text{B.22})$$

$${}^3Q_0(De) = \frac{De^2 (1 - 2.5Z^{-1})}{2\pi (1 + 25De^2 Z^{-2})^{0.5} (1 + 4De^2)^{0.5} (1 + De^2)^{0.5}} \quad \text{for } Z > 2.5 \quad (\text{B.23})$$

B.1.2. MSF Model

The definition of the intrinsic nonlinearity ${}^3Q_0(De)$ and the higher harmonic intensity I_1 are the same as in the Pom-Pom model (see eq. B.1 and eq. B.14). A different definition is used for the real and imaginary part of I_3 , with the orientational effect α and the stretching parameter β .

$$I_3' = \frac{3}{4}(\alpha - \beta/10)G_N^0 \left(\frac{De^2}{1+De^2} - \frac{4De^2}{1+4De^2} + \frac{3De^2}{1+9De^2} \right) \gamma_0^3 \quad (\text{B.24})$$

$$I_3'' = \frac{3}{4}(\alpha - \beta/10)G_N^0 \left(\frac{De}{1+De^2} - \frac{2De^2}{1+4De^2} + \frac{De}{1+9De^2} \right) \gamma_0^3 \quad (\text{B.25})$$

B. Model Calculations

Calculation of I_3 is then done via insertion of I'_3 and I''_3 into the definition of I_3 .

$$I_3 = \sqrt{I_3'^2 + I_3''^2} \quad (\text{B.26})$$

$$I_3 = \sqrt{\left(\frac{3}{4} \left(\alpha - \frac{\beta}{10}\right) G_N^0 \left(\frac{De^2}{1+De^2} - \frac{4De^2}{1+4De^2} + \frac{3De^2}{1+9De^2}\right) \gamma_0^3\right)^2 + \left(\frac{3}{4} \left(\alpha - \frac{\beta}{10}\right) G_N^0 \left(\frac{De}{1+De^2} - \frac{2De^2}{1+4De^2} + \frac{De}{1+9De^2}\right) \gamma_0^3\right)^2} \quad (\text{B.27})$$

$$I_3 = \frac{3}{4} \left(\alpha - \frac{\beta}{10}\right) G_N^0 \gamma_0^3 \sqrt{\left(\frac{De^2}{1+De^2} - \frac{4De^2}{1+4De^2} + \frac{3De^2}{1+9De^2}\right)^2 + \left(\frac{De}{1+De^2} - \frac{2De^2}{1+4De^2} + \frac{De}{1+9De^2}\right)^2} \quad (\text{B.28})$$

The intrinsic nonlinearity ${}^3Q_0(De)$ for the simplified single mode MSF model can then be calculated with eq. (B.14) and eq. (B.28).

$${}^3Q_0(De) = \lim_{\gamma_0 \rightarrow 0} \frac{\frac{3}{4} \left(\alpha - \frac{\beta}{10}\right) G_N^0 \gamma_0^3}{\frac{G_N^0 \gamma_0 De}{(1+De^2)^{0.5}} \gamma_0^2} \sqrt{\left(\frac{De^2}{1+De^2} - \frac{4De^2}{1+4De^2} + \frac{3De^2}{1+9De^2}\right)^2 + \left(\frac{De}{1+De^2} - \frac{2De^2}{1+4De^2} + \frac{De}{1+9De^2}\right)^2} \quad (\text{B.29})$$

$${}^3Q_0(De) = \frac{3}{4} \left(\alpha - \frac{\beta}{10}\right) \frac{1}{De} \sqrt{(1+De^2) \left(\frac{De^2}{1+De^2} - \frac{4De^2}{1+4De^2} + \frac{3De^2}{1+9De^2}\right)^2 + (1+De^2) \left(\frac{De}{1+De^2} - \frac{2De^2}{1+4De^2} + \frac{De}{1+9De^2}\right)^2} \quad (\text{B.30})$$

$${}^3Q_0(De) = \frac{3}{4} \left(\alpha - \frac{\beta}{10}\right) \frac{De^2 \sqrt{36De^6 + 49De^4 + 14De^2 + 1}}{(1+9De^2)(1+4De^2)(1+De^2)^{0.5}} \quad (\text{B.31})$$

$${}^3Q_0(De) = \frac{3}{4} \left(\alpha - \frac{\beta}{10}\right) \frac{De^2 \sqrt{(1+9De^2)(1+4De^2)(1+De^2)}}{(1+9De^2)(1+4De^2)(1+De^2)^{0.5}} \quad (\text{B.32})$$

$${}^3Q_0(De) = \frac{3}{4} \left(\alpha - \frac{\beta}{10}\right) \frac{De^2}{(1+9De^2)^{0.5}(1+4De^2)^{0.5}} \quad (\text{B.33})$$

B.2. Calculation of the Maximum ${}^3Q_{0,\max}$

B.2.1. General Equation

The maximum ${}^3Q_{0,\max}$ is calculated by the derivative of the intrinsic nonlinearity ${}^3Q_0(De)$ (eq. 4.39).

$${}^3Q_0(De) = a \frac{De^2}{1 + bDe^{2+k}} \quad (\text{B.34})$$

$$\frac{\partial({}^3Q_0)}{\partial De} = \frac{2aDe}{1 + bDe^{2+k}} - \frac{aDe^2 bDe^{1+k}(2+k)}{(1 + bDe^{2+k})^2} = \frac{aDe(2 - bkDe^{2+k})}{(1 + bDe^{2+k})^2} \quad (\text{B.35})$$

The maximum can be found by setting eq. (B.35) equal to zero.

$$0 = \frac{aDe(2 - bkDe^{2+k})}{(1 + bDe^{2+k})^2} \quad (\text{B.36})$$

$$0 = 2 - bkDe^{2+k} \quad (\text{B.37})$$

$$De_{\max} = \sqrt[2+k]{\frac{2}{bk}} \quad (\text{B.38})$$

Insertion of eq. (B.38) into the general equation (4.39), with $a = 0.32Z^{-0.5}$, $b = 33.8Z^{-1}$ and $k = 0.35$ (see section 5.3), results ${}^3Q_{0,\max}$ only in dependence of the number of entanglements Z .

$${}^3Q_{0,\max} = a \frac{De_{\max}^2}{1 + bDe_{\max}^{2+k}} \quad (\text{B.39})$$

$${}^3Q_{0,\max} = 0.32Z^{-0.5} \frac{\left(\frac{2}{33.8Z^{-1}0.35}\right)^{2/2.35}}{1 + 33.8Z^{-1} \left(\left(\frac{2}{33.8Z^{-1}0.35}\right)^{1/2.35}\right)^{2.35}} \quad (\text{B.40})$$

$${}^3Q_{0,\max} = 0.32Z^{-0.5} \frac{\left(\frac{2Z}{33.8 \cdot 0.35}\right)^{2/2.35}}{1 + \frac{2}{0.35}} \quad (\text{B.41})$$

$${}^3Q_{0,\max} \approx 0.01Z^{-0.5} Z^{2/2.35} \approx 0.01Z^{0.35} \quad (\text{B.42})$$

B.2.2. Pom-Pom Model

The derivative of the simplified single mode Pom-Pom equation (4.19) is calculated analogous to eq. (B.42).

$${}^3Q_0(De) = \frac{1}{2\pi} \frac{(1 - 2.5Z^{-1})De^2}{1 + 10Z^{-1}De^3} \quad \text{for } Z > 2.5 \quad (\text{B.43})$$

where

$$a = \frac{1}{2\pi}(1 - 2.5Z^{-1}) \quad (\text{B.44})$$

$$b = 10Z^{-1} \quad (\text{B.45})$$

and therefore

$$De_{max} = \sqrt[2+k]{\frac{2}{bk}} = \sqrt[3]{\frac{2Z}{10}} = \sqrt[3]{\frac{Z}{5}} \quad (\text{B.46})$$

Insertion of eq. (B.46) in eq. (B.43) results ${}^3Q_{0,max}$ in dependence of the number of entanglements Z .

$${}^3Q_{0,max} = a \frac{De_{max}^2}{1 + bDe_{max}^{2+k}} \quad (\text{B.47})$$

$${}^3Q_{0,max} = \frac{(1 - 2.5Z^{-1})(Z/5)^{2/3}}{6\pi} \quad (\text{B.48})$$

$$\lim_{Z \rightarrow \infty} {}^3Q_{0,max} = \frac{1}{4\pi} \quad (\text{B.49})$$

B.2.3. MSF Model

As seen from plots of the simplified single mode MSF model equation (4.35) (also see fig. 4.5 in section 4.2.2), the maximum ${}^3Q_{0,max}$ can be calculated from the limi-

ting value at very high Deborah numbers.

$${}^3Q_{0,max} = \lim_{De \rightarrow \infty} \frac{3}{2} \left(\alpha - \frac{\beta}{10} \right) \frac{De^2}{1 + 6De^2} \quad (\text{B.50})$$

$${}^3Q_{0,max} = \frac{1}{4} \left(\alpha - \frac{\beta}{10} \right) \quad (\text{B.51})$$

Bibliography

- (1) Geyer, R.; Jambeck, J. R.; Law, K. L. *Science advances* **2017**, *3*.
- (2) Plastics Europe Plastics - the Facts 2017., 2017.
- (3) Domininghaus, H.; Elsner, P., *Kunststoffe*, *8.*; Springer: Heidelberg, 2012.
- (4) Kaiser, W., *Kunststoffchemie für Ingenieure*; Hanser: München, 2006.
- (5) Hyun, K.; Wilhelm, M.; Klein, C. O.; Cho, K. S.; Nam, J. G.; Ahn, K. H.; Lee, S. J.; Ewoldt, R. H.; McKinley, G. H. *Progress in Polymer Science* **2011**, *36*, 1697–1753.
- (6) Dealy, J. M.; Larson, R. G., *Structure and Rheology of Molten Polymers: From Structure to Flow Behavior and Back Again*; Hanser Publishers and Hanser Gardner Publications: Munich and Cincinnati, 2006.
- (7) Hyun, K.; Kim, S. H.; Ahn, K. H.; Lee, S. J. *Journal of Non-Newtonian Fluid Mechanics* **2002**, *107*, 51–65.
- (8) Clegg, D. W.; Collyer, A. A., *Rheological Measurement*, 2nd ed; Chapman & Hall: London and New York, 1998.
- (9) Cho, K. S.; Hyun, K.; Ahn, K. H.; Lee, S. J. *Journal of Rheology* **2005**, *49*, 747.
- (10) Ewoldt, R. H.; Hosoi, A. E.; McKinley, G. H. *Journal of Rheology* **2008**, *52*, 1427.

Bibliography

- (11) Ewoldt, R. H.; Winter, P.; Maxey, J.; McKinley, G. H. *Rheologica Acta* **2010**, *49*, 191–212.
- (12) Pipkin, A. C., *Lectures On Viscoelasticity Theory*, 2nd ed; Applied mathematical sciences, Vol. 7; Springer-Verlag: New York, 1986.
- (13) Rogers, S. A.; Erwin, B. M.; Vlassopoulos, D.; Cloitre, M. *Journal of Rheology* **2011**, *55*, 435.
- (14) Rogers, S. A.; Lettinga, M. P. *Journal of Rheology* **2012**, *56*, 1.
- (15) Wilhelm, M. *Macromolecular Materials and Engineering* **2002**, *287*, 83–105.
- (16) Brader, J. M.; Siebenbürger, M.; Ballauff, M.; Reinheimer, K.; Wilhelm, M.; Frey, S. J.; Weysser, F.; Fuchs, M. *Physical Review E* **2010**, *82*.
- (17) Cho, K. S.; Song, K.-W.; Chang, G.-S. *Journal of Rheology* **2010**, *54*, 27.
- (18) Fleury, G.; Schlatter, G.; Muller, R. *Rheologica Acta* **2004**, *44*, 174–187.
- (19) Vittorias, I.; Lilge, D.; Baroso, V.; Wilhelm, M. *Rheologica Acta* **2011**, *50*, 691–700.
- (20) Neidhöfer, T.; Sioula, S.; Hadjichristidis, N.; Wilhelm, M. *Macromolecular Rapid Communications* **2004**, *25*, 1921–1926.
- (21) Schlatter, G.; Fleury, G.; Muller, R. *Macromolecules* **2005**, *38*, 6492–6503.
- (22) Vittorias, I.; Parkinson, M.; Klimke, K.; Debbaut, B.; Wilhelm, M. *Rheologica Acta* **2006**, *46*, 321–340.
- (23) Hyun, K.; Wilhelm, M. *Macromolecules* **2009**, *42*, 411–422.
- (24) Hyun, K.; Kim, W.; Park, S. J.; Wilhelm, M. *Journal of Rheology* **2013**, *57*, 1–25.
- (25) Abbasi, M.; Golshan Ebrahimi, N.; Wilhelm, M. *Journal of Rheology* **2013**, *57*, 1693.

- (26) Wagner, M. H.; Rolón-Garrido, V. H.; Hyun, K.; Wilhelm, M. *Journal of Rheology* **2011**, *55*, 495.
- (27) Ferry, J. D., *Viscoelastic Properties of Polymers*, 3d ed; Wiley: New York, 1980.
- (28) Kempf, M.; Ahirwal, D.; Cziep, M.; Wilhelm, M. *Macromolecules* **2013**, *46*, 4978–4994.
- (29) Hoyle, D. M.; Auhl, D.; Harlen, O. G.; Barroso, V. C.; Wilhelm, M.; McLeish, T. C. B. *Journal of Rheology* **2014**, *58*, 969–997.
- (30) Bishko, G.; McLeish, T.; Harlen, O.; Larson, R. *Physical Review Letters* **1997**, *79*, 2352–2355.
- (31) McLeish, T. C. B.; Larson, R. G. *Journal of Rheology* **1998**, *42*, 81–110.
- (32) Rolón-Garrido, V. H. *Rheologica Acta* **2014**, *53*, 663–700.
- (33) Szwarc, M.; Levy, M.; Milkovich, R. *Journal of the American Chemical Society* **1956**, *78*, 2656–2657.
- (34) Szwarc, M., *Carbanions, Living Polymers, and Electron Transfer Processes*; Interscience Publishers: New York, 1968.
- (35) Lechner, M. D.; Gehrke, K.; Nordmeier, E.; Heenan, R. K., *Makromolekulare Chemie: ein Lehrbuch für Chemiker, Physiker, Materialwissenschaftler und Verfahrenstechniker*, 4., überarb. und erw. Aufl.; Birkhäuser: Basel, 2010.
- (36) Hadjichristidis, N.; Hirao, A., *Anionic Polymerization: Principles, Practice, Strength, Consequences and Applications*; Springer Japan: Tokyo, 2015.
- (37) Gnanou, Y.; Fontanille, M., *Organic and Physical Chemistry of Polymers*; Wiley: Hoboken, NJ, 2008.
- (38) Hsieh, H. L.; Quirk, R. P., *Anionic Polymerization: Principles and Practical Applications*; *Plastics engineering*, Vol. 34; Dekker: New York, 1996.
- (39) Mark, J. E., *Physical Properties of Polymer Handbook*, 2nd ed; Springer: New York, 2006.

Bibliography

- (40) Odian, G., *Principles of Polymerization*, 4. ed.; Wiley-Interscience: Hoboken, NJ, 2004.
- (41) Gebert, W.; Hinz, J.; Sinn, H. *Makromolekulare Chemie* **1971**, *144*, 97–115.
- (42) Worsfold, D. J.; Bywater, S. *Macromolecules* **1978**, *11*, 582–586.
- (43) Szwarc, M.; van Beylen, M., *Ionic Polymerization and Living Polymers*; Springer Netherlands: Dordrecht, 1993.
- (44) Worsfold, D. J.; Bywater, S. *Macromolecules* **1972**, *5*, 393–397.
- (45) Hadjichristidis, N.; Pitsikalis, M.; Iatrou, H. In *Block Copolymers I*, Abetz, V., Ed.; *Advances in Polymer Science*, Vol. 189; Springer-Verlag: Berlin, 2005, pp 1–124.
- (46) Hong, K.; Uhrig, D.; Mays, J. W. *Current Opinion in Solid State and Materials Science* **1999**, *4*, 531–538.
- (47) Fujimoto, T.; Zhang, H. M.; Kazama, T.; Isono, Y.; Hasegawa, H.; Hashimoto, T. *Polymer* **1992**, *33*, 2208–2213.
- (48) Uhrig, D.; Mays, J. W. *Polymer Chemistry* **2011**, *2*, 69–76.
- (49) Inoki, M.; Akutsu, F.; Yamaguchi, H.; Naruchi, K.; Miura, M. *Macromolecular Chemistry and Physics* **1994**, *195*, 2799–2804.
- (50) Jannasch, P.; Wesslén, B. *Journal of Polymer Science, Part A: Polymer Chemistry* **1995**, *33*, 1465–1474.
- (51) Falk, J. C.; Schlott, R. J. *Journal of Macromolecular Science, Part A: Chemistry* **1973**, *7*, 1663–1668.
- (52) Hadjichristidis, N.; Roovers, J. *Journal of Polymer Science, Polymer Physics Edition* **1978**, *16*, 851–858.
- (53) Altares, T.; Wyman, D. P.; Allen, V. R.; Meyersen, K. *Journal of Polymer Science, Part A: General Papers* **1965**, *3*, 4131–4151.

- (54) Itsuno, S.; Uchikoshi, K.; Ito, K. *Journal of the American Chemical Society* **1990**, *112*, 8187–8188.
- (55) Pepper, K. W.; Paisley, H. M.; Young, M. A. *Journal of the Chemical Society* **1953**, 4097.
- (56) Cameron, G. G.; Qureshi, M. Y. *Macromolecular Rapid Communications* **1981**, *2*, 287–291.
- (57) Iraqi, A.; Seth, S.; Vincent, C. A.; Cole-Hamilton, D. J.; Watkinson, M. D.; Graham, I. M.; Jeffrey, D. *Journal of Materials Chemistry* **1992**, *2*, 1057.
- (58) Guo, X.; Farwaha, R.; Rempel, G. L. *Macromolecules* **1990**, *23*, 5047–5054.
- (59) Hempenius, M. A.; Michelberger, W.; Möller, M. *Macromolecules* **1997**, *30*, 5602–5605.
- (60) Yuan, Z.; Gauthier, M. *Macromolecules* **2005**, *38*, 4124–4132.
- (61) Kempf, M.; Barroso, V. C.; Wilhelm, M. *Macromolecular Rapid Communications* **2010**, *31*, 2140–2145.
- (62) Hadjichristidis, N. et al. *Macromolecules* **2000**, *33*, 2424–2436.
- (63) Clayden, J.; Greeves, N.; Warren, S.; Wothers, P., *Organic Chemistry*, Reprinted, with corrections; Oxford University Press: New York, 2007.
- (64) Gelling, I. R. *Rubber Chemistry and Technology* **1985**, *58*, 86–96.
- (65) Gnecco, S.; Pooley, A.; Krause, M. *Polymer Bulletin* **1996**, *37*, 609–615.
- (66) Tutorskii, I. A.; Khodzhayeva, I. D.; Dogadkin, B. A. *Macromolecular Compounds, Series A. Journal of the Theoretical and Experimental Chemistry and Physics of Macromolecular Compounds* **1974**, *16*, 157–168.
- (67) Abbasi, M.; Faust, L.; Riazi, K.; Wilhelm, M. *Macromolecules* **2017**, *50*, 5964–5977.

Bibliography

- (68) Krebs, F. C.; Jørgensen, M.; Lebech, B.; Almdal, K.; Pedersen, W. B. *Polymer Bulletin* **2000**, *43*, 485–490.
- (69) Abbasi, M.; Ebrahimi, N. G.; Nadali, M.; Esfahani, M. K. *Rheologica Acta* **2012**, *51*, 163–177.
- (70) Abdel-Goad, M.; Pyckhout-Hintzen, W.; Kahle, S.; Allgaier, J.; Richter, D.; Fetters, L. J. *Macromolecules* **2004**, *37*, 8135–8144.
- (71) *Block Copolymers I*; Abetz, V., Ed.; Advances in Polymer Science; Springer-Verlag: Berlin/Heidelberg, 2005.
- (72) Blackwell, R. J.; McLeish, T. C. B.; Harlen, O. G. *Journal of Rheology* **2000**, *44*, 121–136.
- (73) Bracewell, R. N., *The Fourier Transform and Its Applications*, 3rd ed.; McGraw-Hill: Boston, 2000.
- (74) Butz, T., *Fouriertransformation für Fußgänger*, 7., aktualisierte Auflage; SpringerLink : Bücher; Vieweg+Teubner Verlag: Wiesbaden, 2012.
- (75) Currie, P. K. *Journal of Non-Newtonian Fluid Mechanics* **1982**, *11*, 53–68.
- (76) Cziep, M. A.; Abbasi, M.; Heck, M.; Arens, L.; Wilhelm, M. *Macromolecules* **2016**, *49*, 3566–3579.
- (77) Doi, M. *Journal of Polymer Science, Polymer Physics Edition* **1983**, *21*, 667–684.
- (78) Doi, M.; Edwards, S. F. *Journal of the Chemical Society, Faraday Transactions 2: Molecular and Chemical Physics* **1978**, *74*, 1789–1801.
- (79) Doi, M.; Edwards, S. F. *Journal of the Chemical Society, Faraday Transactions 2: Molecular and Chemical Physics* **1978**, *74*, 1802–1817.
- (80) Doi, M.; Edwards, S. F. *Journal of the Chemical Society, Faraday Transactions 2: Molecular and Chemical Physics* **1978**, *74*, 1818–1832.
- (81) Doi, M.; Edwards, S. F. *Journal of the Chemical Society, Faraday Transactions 2: Molecular and Chemical Physics* **1979**, *75*, 38–54.

- (82) Van Dusschoten, D.; Wilhelm, M. *Rheologica Acta* **2001**, *40*, 395–399.
- (83) Ederle, Y.; Isel, F.; Grutke, S.; Lutz, P. J. *Macromolecular Symposia* **1998**, *132*, 197–206.
- (84) Edwards, S. F. *Proceedings of the Physical Society* **1967**, *92*, 9–16.
- (85) Fetters, L. J.; Lohse, D. J.; Richter, D.; Witten, T. A.; Zirkel, A. *Macromolecules* **1994**, *27*, 4639–4647.
- (86) De Gennes, P. G. *The Journal of Chemical Physics* **1971**, *55*, 572–579.
- (87) Goodwin, J. W.; Hughes, R. W., *Rheology for Chemists: An Introduction*, 2. ed.; Royal Society of Chemistry: Cambridge, 2008.
- (88) Graessley, W. W. *Journal of Polymer Science, Polymer Physics Edition* **1980**, *18*, 27–34.
- (89) Graessley, W. W. In *Synthesis and Degradation*, Neuse, E. W., Ed.; Advances in Polymer Science, Vol. 47; Springer London and Central Book Services New Zealand: Guildford and Mitcham, VIC, Australia, 1982, pp 67–117.
- (90) vanGurp, M.; Palmen, J., *Time-Temperature Superposition for Polymeric Blends*; XIIth International Congress on Rheology, Proceedings, 1996.
- (91) Hilliou, L.; van Dusschoten, D.; Wilhelm, M.; Burhin, H.; Rodger, E. R. *Rubber Chemistry and Technology* **2004**, *77*, 192–200.
- (92) Inkson, N. J.; McLeish, T. C. B.; Harlen, O. G.; Groves, D. J. *Journal of Rheology* **1999**, *43*, 873–896.
- (93) Larson, R. G.; Khan, S. A.; Raju, V. R. *Journal of Rheology* **1988**, *32*, 145–161.
- (94) Larson, R. G., *The Structure and Rheology of Complex Fluids*; Topics in chemical engineering; Oxford University Press: New York, 1999.
- (95) Larson, R. G. *Macromolecules* **2001**, *34*, 4556–4571.

Bibliography

- (96) Lee, K.; Mackley, M. R.; McLeish, T. C. B.; Nicholson, T. M.; Harlen, O. G. *Journal of Rheology* **2001**, *45*, 1261–1277.
- (97) Macosko, C. W., *Rheology: Principles, Measurements, and Applications*; Advances in Interfacial Engineering Series; Wiley-VCH: New York, 1994.
- (98) Malkin, A. J.; Isayev, A. I., *Rheology: Concepts, Methods, & Applications*; Chem-Tec: Toronto, 2006.
- (99) McLeish, T. C. B. *Advances in Physics* **2002**, *51*, 1379–1527.
- (100) Mead, D. W.; Larson, R. G.; Doi, M. *Macromolecules* **1998**, *31*, 7895–7914.
- (101) Mezger, T., *The Rheology Handbook: For Users of Rotational and Oscillatory Rheometers*, 3rd., rev. ed.; European Coatings Tech Files; Vincentz Network: Hannover, 2013.
- (102) Neubauer, A., *DFT - Diskrete Fourier-Transformation: Elementare Einführung*; SpringerLink : Bücher; Vieweg+Teubner Verlag: Wiesbaden, 2012.
- (103) *Synthesis and Degradation*; Neuse, E. W., Ed.; Advances in Polymer Science; Springer London and Central Book Services New Zealand: Guildford and Mitcham, VIC, Australia, 1982.
- (104) Pantazis, D.; Chalari, I.; Hadjichristidis, N. *Macromolecules* **2003**, *36*, 3783–3785.
- (105) Park, S. J.; Larson, R. G. *Macromolecules* **2004**, *37*, 597–604.
- (106) Pearson, D. S. *Rubber Chemistry and Technology* **1987**, *60*, 439–496.
- (107) Pham, Q. T., *Proton and carbon NMR spectra of polymers*, 5th ed.; Wiley: Chichester, West Sussex, England and New York, 2003.
- (108) Reinheimer, K.; Grosso, M.; Hetzel, F.; Kübel, J.; Wilhelm, M. *Journal of Colloid and Interface Science* **2012**, *380*, 201–212.
- (109) Rouse, P. E. *The Journal of Chemical Physics* **1953**, *21*, 1272–1280.

- (110) Rubinstein, M.; Colby, R. H., *Polymer Physics*, 1st ed.; Oxford University Press: Oxford, 2016.
- (111) Schulze, U.; Fonagy, T.; Komber, H.; Pompe, G.; Pionteck, J.; Ivan, B. *Macromolecules* **2003**, *36*, 4719–4726.
- (112) Schulze, D.; Roths, T.; Friedrich, C. *Rheologica Acta* **2005**, *44*, 485–494.
- (113) Schweizer, T. *Journal of Rheology* **2003**, *47*, 1071–1085.
- (114) Song, H. Y.; Park, S. J.; Hyun, K. *Macromolecules* **2017**, *50*, 6238–6254.
- (115) Strobl, G. R., *The Physics of Polymers: Concepts for Understanding their Structures and Behavior*, Third revised and expanded edition; Springer: Berlin, Heidelberg, and New York, op. 2007.
- (116) Trinkle, S.; Friedrich, C. *Rheologica Acta* **2001**, *40*, 322–328.
- (117) Trinkle, S.; Walter, P.; Friedrich, C. *Rheologica Acta* **2002**, *41*, 103–113.
- (118) Unidad, H. J.; Goad, M. A.; Bras, A. R.; Zamponi, M.; Faust, R.; Allgaier, J.; Pyckhout-Hintzen, W.; Wischniewski, A.; Richter, D.; Fetters, L. J. *Macromolecules* **2015**, *48*, 6638–6645.
- (119) Vega, J. F.; Rastogi, S.; Peters, G. W. M.; Meijer, H. E. H. *Journal of Rheology* **2004**, *48*, 663.
- (120) Wagner, M. H.; Schaeffer, J. *Journal of Rheology* **1992**, *36*, 1–26.
- (121) Wagner, M. H.; Rubio, P.; Bastian, H. *Journal of Rheology* **2001**, *45*, 1387–1412.
- (122) Wagner, M. H.; Yamaguchi, M.; Takahashi, M. *Journal of Rheology* **2003**, *47*, 779–793.
- (123) Wagner, M. H.; Hepperle, J.; Münstedt, H. *Journal of Rheology* **2004**, *48*, 489–503.
- (124) Watanabe, H. *Progress in Polymer Science* **1999**, *24*, 1253–1403.

Bibliography

- (125) Wilhelm, M.; Maring, D.; Spiess, H. W. *Rheologica Acta* **1998**, *37*, 399–405.
- (126) Wilhelm, M.; Reinheimer, P.; Ortseifer, M. *Rheologica Acta* **1999**, *38*, 349–356.
- (127) Wilhelm, M.; Reinheimer, K.; Kübel, J. *Zeitschrift für Physikalische Chemie* **2012**, *226*, 547–567.
- (128) Williams, M. L.; Landel, R. F.; Ferry, J. D. *Journal of the American Chemical Society* **1955**, *77*, 3701–3707.
- (129) Wong, M. W., *Discrete Fourier Analysis; Pseudo-Differential Operators, Theory and Applications*, Vol. 5; Springer Basel AG: Basel, 2011.
- (130) Wu, S. *Journal of Polymer Science, Part B: Polymer Physics* **1987**, *25*, 557–566.